Cell Biomechanics of the Central Nervous System

by

Kristin Briana Bernick

B.S., Biomedical Engineering,
University of California, Davis (2006)

Submitted to the Department of Biological Engineering in partial fulfillment of the requirements for the degree of

Doctor of Philosophy in Biological Engineering

at the

MASSACHUSETTS INSTITUTE OF TECHNOLOGY

June 2011

Author.....
Department of Biological Engineering
May 20, 2011

Certified by.....
Simona Socrate, Ph.D.
Principal Research Scientist, Harvard-MIT Division of Health Sciences and Technology
and Institute for Soldier Nanotechnologies
Thesis Supervisor

Certified by.....
Roger Kamm, Ph.D.
Singapore Research Professor of Mechanical and Biological Engineering
Thesis Supervisor

Accepted by.....
K. Dane Wittrup, Ph.D.
Professor of Chemical and Biological Engineering
Chairman, Course 20 Graduate Program Committee

Thesis Committee

Simona Socrate, Ph.D.
Thesis Co-advisor
Principal Research Scientist, Harvard-MIT Division of Health Sciences and Technology and Institute for Soldier Nanotechnologies
Massachusetts Institute of Technology

Roger Kamm, Ph.D.
Thesis Co-advisor
Professor of Biological and Mechanical Engineering
Massachusetts Institute of Technology

Ed Boyden, Ph.D.
Professor of Biological Engineering and Media Arts and Sciences
Massachusetts Institute of Technology

Cell Biomechanics of the Central Nervous System

by

Kristin Briana Bernick

Submitted to the Department of Biological Engineering on May 20, 2011 in Partial Fulfillment of the Requirements for the Degree of Doctor of Philosophy in Biological Engineering

ABSTRACT

Traumatic brain injury (TBI) is a significant cause of death and morbidity in both the civilian and military populations. The major causes of TBI, such as motor vehicle accidents, falls, sports concussions, and ballistic and explosive blast threats for military personnel, are well established and extensively characterized; however, there remains much to be learned about the specific mechanisms of damage leading to brain injury, especially at the cellular level. In order to understand how cells of the central nervous system (CNS) respond to mechanical insults and stimuli, a combined modeling/experimental approach was adopted. A computational framework was developed to accurately model how cells deform under various macroscopically imposed loading conditions. In addition, *in vitro* (cell culture) models were established to investigate damage responses to biologically relevant mechanical insults. In order to develop computational models of cell response to mechanical loading, it is essential to have accurate material properties for all cells of interest. In this work, the mechanical responses of neurons and astrocytes were quantified using atomic force microscopy (AFM) at three different loading rates and under relaxation to enable characterization of both the elastic and viscous components of the cell response. AFM data were used to calibrate an eight-parameter rheological model implemented in the framework of a commercial finite element package (Abaqus). Model parameters fit to the measured responses of neurons and astrocytes provide a quantitative measure of homogenized nonlinear viscoelastic properties for each cell type. In order to ensure that the measured responses could be considered representative of cell populations in their physiological environment, cells were also grown and tested on substrates of various stiffness, with the softest substrate mimicking the stiffness of brain tissue. Results of this study showed both the morphology and measured force response of astrocytes to be significantly affected by the stiffness of their substrate, with cells becoming increasingly rounded on soft substrates. Results of simulations suggested that changes in cell morphology were able to account for the observed changes in AFM force response, without significant changes to the cell material properties. In contrast, no significant changes in cell morphology were observed for neurons. These results highlight the importance of growing cells in a biologically relevant environment when studying mechanically mediated responses, such as TBI. To address this requirement, we developed two model systems with CNS cells grown in soft, 3D gels to investigate damage arising from dynamic compressive loading and from a shock pressure wave. These damage protocols, coupled with the single cell computational models, provide a new tool set for characterizing damage mechanisms in CNS cells and for studying TBI in highly controllable *in vitro* conditions.

Thesis Supervisors:
Simona Socrate, Ph.D.
Title: Principal Research Scientist, Harvard-MIT Division of Health Sciences and Technology and Institute for Soldier Nanotechnologies

Roger Kamm, Ph.D.
Title: Singapore Research Professor of Mechanical and Biological Engineering

Acknowledgements

This thesis would not have been possible without the support of many people. First, I would like to thank Prof. Subra Suresh, Dr. Simona Socrate, and Prof. Roger Kamm for each providing guidance and advising throughout my graduate program. Prof. Subra Suresh served as my advisor for the first 4 years of my graduate studies, and during that time, he guided my development as a scientist by serving as an excellent role model with high scientific standards, professionalism, and a dedication to scientific research. Dr. Simona Socrate has been an excellent advisor, sharing her passion for research and continually inspiring me with new ideas and collaborations. Prof. Roger Kamm has served as both my committee chair, and more recently, as a co-advisor, providing insightful discussions and support throughout my time at MIT. In addition, I am grateful to Prof. Ed Boyden for serving on my thesis committee and providing key insight and discussions, especially in his area of expertise of neuroscience. I am grateful to have had formative interactions with each of these researchers throughout my Ph.D.

I would like to thank Prof. Alan Grodzinsky for discussions and encouragement throughout my Ph.D, and for making my time spent in Tech Square enjoyable. In addition, he provided excellent mentoring when I served as his teaching assistant in his graduate course on Molecular, Cellular, and Tissue Biomechanics.

In addition, I had help from fellow students and collaborators throughout my time at MIT. I extend immense thanks to Thibault Prévost for his significant contributions to this thesis especially in the areas of model development, AFM program coding, and set-up and design of the damage devices. I would like to thank Cathal Kearney for helping significantly with the blast system set-up and device calibration and Prof. Myron Spector for allowing me to use the Dolorclast shockwave device. I am also grateful for the help of the laboratory of Professor

Sebastian Seung, especially Heather Sullivan and Jeannine Foley, who provided me with all of the cortical tissue samples necessary for the work of this thesis. In addition, I would like to thank the laboratory of Dr. Michael Whalen at Massachusetts General Hospital, especially Dr. Jianhua Qiu, for helping to characterize our damage devices and for useful discussions on cell signaling and biochemistry.

I also had the opportunity to meet many wonderful people while at MIT who provided both insightful discussions and made my 5 years here fun and memorable. My class, BE 2006, helped me get through my first year here successfully and resulted in lifelong friendships. The members of the Suresh lab and other students in Technology Square made my time spent in lab enjoyable.

I also acknowledge the support of my funding sources, the National Science Foundation Graduation Research Fellowship and the National Institutes of Health Molecular, Cell, and Tissue Biomechanics Training Grant.

The help and support I had to successfully complete this thesis, did not just come from my time spent at MIT. I had many wonderful science teachers and professors who inspired me to pursue this path and showed me how rewarding and interesting a career in the sciences could be. I am especially grateful to Prof. Yin Yeh for letting me work in his lab as an undergraduate at the University of California, Davis and for giving me a positive first experience with academic research. His mentoring and encouragement was a key factor in my decision to attend MIT.

I was also lucky enough to meet my boyfriend, Bryan, during my time at MIT. He was always supportive after a long day in the lab and put up with the ups and downs that come along with graduate school. I am extremely grateful to have him in my life and value the encouragement and support he gives to all aspects of my life.

Most importantly, I extend tremendous gratitude to my family for continuous support over the years. My parents, Debbie and Dave, and my sister, Kim, have supported me in everything that I have done and always stood behind me 100%, encouraging me to pursue my dreams. Knowing that they believed in me helped me through even the toughest situations. I could not have made it this far without their love and support.

Contents

1 Introduction **25**

2 Background **29**

2.1 Traumatic Brain Injury 29

2.2 Biomechanics of Single Neurons and Glia 38

2.3 Existing Cellular Level Models of Traumatic Brain Injury 44

3 Methods for Determining Cell Material Properties **49**

3.1 Overview 49

3.2 Atomic Force Microscopy Experiments 50

3.2.1 Cell Culture 50

3.2.2 Measurements of Neuron Somata on Glass 52

3.2.3 Measurements of Neuron Processes on Glass 56

3.2.4 Measurements of Astrocytes on Glass 57

3.2.5 Measurements of Neurons and Astrocytes on Gels 60

3.3 Finite Element Simulations 62

4 Characterization of Neuron and Astrocyte Response on Glass **69**

4.1 Introduction 69

4.2 Neuron Results 70

4.2.1 Response of the Neuron Soma 70

4.2.2 Response of the Neuron Processes 75

4.3 Astrocyte Results 78

4.4 Discussion 81

4.4 Summary 84

5 Effect of Substrate Stiffness on Neuron and Astrocyte Response **85**

5.1 Introduction 85

5.2 Results 86

5.3 Discussion 102

5.4 Summary 106

6 Design of Damage Devices **107**

6.1 Introduction 107

6.2 3D Cell Cultures 108

6.3 Shockwave device 111

6.4 Compression Device 124

6.5 Summary 128

7 Conclusions and Thesis Contributions **131**

List of Figures

2-1: Characteristic blast wave pressure profile and resulting changes in atmospheric pressure. Before the explosion (1) atmospheric pressure is normal. After the explosion and upon passage of the shockwave (2), the blast wind flows away from the explosion. When a drop in atmospheric pressure occurs below normal, the direction of the blast wind reverses (3). Reproduced with permission from Taber *et al* [1] 30

2-2: Schematic of the primary, secondary, and tertiary blast mechanisms and the characteristic brain injuries. Reprinted with permission from Macmillan Publishers Ltd: Journal of Cerebral Blood Flow and Metabolism, copyright 2010 [2] 31

2-3: Official Department of Defense numbers for different severities of Traumatic Brain Injury (from http://www.dvbic.org/TBI-Numbers.aspx) 33

2-4: Schematic depicting some of the key pathways associated with secondary damage after TBI, involving neurons (blue), astrocytes (orange), and microglia (green). Reproduced with permission from Park et al. [3] © Canadian Medical Association. Copied under license

from the Canadian Medical Association and Access Copyright. Further reproduction prohibited..... 35

3-1: Results of immunocytochemistry to verify cell types. Cells grown in serum containing media were found to be primarily astrocytes (A) and those grown in serum free media primarily neurons (B). Scale Bars 20 μm..... 51

3-2: (A) SEM image of tipless cantilever with attached 45 μm polystyrene sphere (dimensions in μm). (B) Bright field image of AFM tip with bead adjacent to neuron to be indented; 20 μm scale bar. (C) Schematic of AFM experimental setup – Polystyrene bead compressing the cell body of a neuron plated on glass. (D) AFM testing procedure: sample approach, pre-load (black solid), sequences of load-unload segments at 10 μm/s (red dot), 1 μm/s (blue solid), 0.1 μm/s (green dash-dot), followed by stress–relaxation (black dash). 54

3-3: Cell height determination procedure: cell (black solid) and glass substrate (red, blue, green dash) indentation curves were used to retrieve relative piezo positions associated with contact events between cell/glass and cantilever, thereby providing an estimate for the cell height..... 55

3-4: Representative neuron and AFM cantilever with pyramidal tip adjacent to process to be indented. Processes were indented close to the neuron soma..... 57

3-5: Confocal images of astrocytes cultured for 1 day after passage (A) and 3 days (B), highlighting the choice to test cells after 1 day when cells remain isolated and measurements on single cells are possible; nucleus (Hoechst, blue) and cytoplasm (Calcein-AM, green); scale bars 20 μm..... 58

3-6: Astrocyte loading routine consisting of an initial approach to the cell to a pre-load of 0.3 nN to establish contact (green dash), a 15 s pause for equilibration (green solid), 3 sets of load-unload cycles to a 1 μm indentation depth at 3 different loading rates (10 μm/s (black solid), 1 μm/s (cyan solid), and 0.1 μm/s (blue dash)), and a 2 minute stress relaxation test (red dash)..... 59

3-7: Top (A) and side (B) views of an astrocyte to be indented with polystyrene sphere (darker blue in side view); cytoplasm (calcein-AM; green); nucleus (Hoechst 33342; cyan)..... 59

3-8: (A) Schematic of cell material model, including 8 material parameters. (B) Representative finite element model geometry for an astrocyte tested on glass. (C) Representative geometry and meshing for a neuron grown on gel, with the gel layer included in the model. 68

4-1: AFM data for a representative neuron of diameter 14.2 μm and height 7.6 μm. Force versus displacement response at the 3 consecutive loading rates of 10 μm/s (red dash-dot), 1 μm/s (green dot), and 0.1 μm/s (blue solid)..... 71

4-2: Force versus time responses measured for one representative neuron of diameter 14.2 μm and height 7.6 μm (black) and simulated in Abaqus with actual cell geometry (red dash). Material parameters for this cell were found to be: μ_o = 13 Pa, λ_L = 1.06, G_o = 85 Pa, G_∞ = 80 Pa, η = 3000 Pa.s, σ_o = 0.005 Pa, and n = 1. Error measure for the model fit was: 1.09×10^{-4}..... 71

4-3: (A) Average force versus time response for 87 cells (black line) with plus and minus standard deviations (grey line); model fit (red dashes) to average response. The pictured model fit corresponds to an error measure of 1.1×10^{-4}. (B, C, and D) Average force versus displacement response at 10, 1 and 0.1 μm/s respectively. Error bars represent standard deviations and red dashes correspond to model fit. Material parameters obtained by fitting the force-indentation response to the average experimental response were found to be: μ_o = 16 Pa, λ_L = 1.05, G_o = 75 Pa, G_∞ = 40 Pa, η = 3000 Pa.s, σ_o = 0.005 Pa, and n = 1. K was held constant at 10,000 Pa. (E) Distribution in maximum force level at the end of the first loading ramp for each displacement rate. Outliers are displayed with a red + sign. Rate effects were found to be statistically significant ($P < 0.0001$, one-way ANOVA)..... 73

4-4: (A) Mean (black) and standard deviation (grey) for 10 neurons indented with loading rates in reverse order (0.1, 1, 10 μm/s). Model predictions (red dash) using the mean set of parameters obtained for indenting a neuron in 10, 1, 0.1 μm/s loading rate order ; (B) Peak forces reached at the end of the first loading ramp for each displacement rate. Rate effects were found to be significant ($P < 0.006$, one-way ANOVA)..... 74

4-5: (A, B) Force versus displacement response for processes at 10 and 1 μm/s, respectively (Black=mean; Grey=standard deviation, N=25). (C, D) Sample Hertz fits for a single process at 10 and 1 μm/s, respectively (AFM data= black dots; Hertz Fit= Red Line). (E) Box plot showing pseudo-elastic Young's Modulus dependency on loading rate. Differences are statistically significant with $P<0.01$ 76

4-6: AFM data (black) and elastic model fit (red dashes) for neuron soma indented at 10 μm/s (A) and 1 μm/s (B). Young's Modulus values used for fitting were 725 Pa at 10 μm/s and 350 Pa at 1 μm/s with the cells assumed to be incompressible with a Poisson's ratio of 0.5. 78

4-7: AFM data for a representative astrocyte of diameter 36 μm and height 5 μm. (A) Force versus displacement response at the 3 consecutive loading rates of 10 μm/s (blue dash-dot), 1 μm/s (cyan dash), and 0.1 μm/s (red solid). (B) Force versus time response..... 79

4-8: Average force versus time response for 37 astrocytes (black line) with plus and minus standard deviations (grey line); model fit (red dashes) to average response. Material parameters obtained by fitting the force-indentation response to the average experimental response were found to be: $\mu_o = 13$ Pa, $\lambda_L = 1.08$, $G_o = 275$ Pa, $G_\infty = 80$ Pa, $\eta = 300$ Pa.s, $\sigma_o = 0.005$ Pa, and $n = 0.80$. K was held constant at 10,000 Pa..... 80

5-1: A. Sample Hertz fit for a representative Gel 1 (AFM data- black dots; Hertz model fit- red solid). B. Representative Gel 3 tested using cell loading routine at 10, 1, and 0.1 μm/s and in relaxation (to a depth of 0.8 μm)..... 87

5-2: Dye versus no dye AFM force vs. time data for astrocytes (A) and neurons (B). Mean response for cells with no dye is shown in red with +/- standard deviation in grey (Astrocytes N=9; Neuron N=9). Mean response for cells with dye is shown in black dashes with +/- standard deviation in blue (Astrocytes N=37; Neuron N=15)..... 88

5-3: Force versus time response for astrocytes (A) and neurons (B) grown on gels of 4 different stiffnesses and glass (glass > Gel 4 > Gel 3 > Gel 2 > Gel 1) show astrocyte response to be more dependent on changing substrate stiffness with two groups emerging (Glass and Gel 4) and (Gel 1, Gel 2, and Gel 3)..... 89

5-4: Maximum force reached for first 10 μm/s loading ramp for astrocytes (A) and neurons (B) Astrocytes grown on Gel 4 were statistically different from Gels 1, 2, and 3 ($P<0.001$) while no statistical significance was shown for neurons grown on different gels..... 89

5-5: Scatter in height and radius measurements for neurons (A) and Astrocytes (B) grown on different substrates; values obtained from confocal images..... 91

5-6: Sample morphology of astrocytes grown on A. Gel 1, B. Gel 2, C. Gel 3, D. Gel 4, and E. Glass, and neurons grown on F. Gel 1, G. Gel 2, H. Gel 3, I. Gel 4, and J. Glass; all scale bars 20 μm. 92

5-7: AFM force response for astrocyes grown on Gel 4 classified as having a rounded (A) or spread (B) morphology based on height/radius ratio. (Mean=black line; standard deviation= grey line; rounded N=8; spread N=19). Sample astrocytes classified as spread (C.) and round (D). E. Box plot showing the maximum force reached during the first 10 μm/s loading. Force for round and spread are statistically significant with $P<0.001$..... 93

5-8: Neuron response and simulation results for cells on (A) Gel 1, (B) Gel 2, (C) Gel 3, and (D) Gel 4. Mean AFM data shown in black with +/- standard deviation in grey and simulation results with parameters obtained from fitting mean response on glass (Chapter 4). $\mu_o = 16$ Pa, $\lambda_L = 1.05$, $G_o = 75$ Pa, $G_\infty = 40$ Pa, $\eta = 3000$ Pa.s, $\sigma_o = 0.005$ Pa, and $n = 1$. K was held constant at 10,000 Pa..... 95

5-9: Neuron response and simulation results for cells on (A) Gel 1, (B) Gel 2, (C) Gel 3, and (D) Gel 4. Mean AFM data shown in black with +/- standard deviation in grey and simulation results with parameters calibrated to data for each gel and listed in Table 5-2..... 96

5-10: Neuron response and simulation results for cells on (A) Gel 1, (B) Gel 2, (C) Gel 3, and (D) Gel 4. Mean AFM data shown in black with +/- standard deviation in grey and

simulation results with parameters obtained by taking the mean of optimized parameters obtained for all substrates (Listed as mean in Table 5-2)..... 97

5-11: Astrocyte response and simulation results for cells on (A) Gel 1, (B) Gel 2, (C) Gel 3, and (D) Gel 4. Mean AFM data shown in black with +/- standard deviation in grey and simulation results with parameters obtained from fitting mean response on glass (Chapter 4). μ_o = 13 Pa, λ_L = 1.08, G_o = 275 Pa, G_∞ = 80 Pa, η = 300 Pa.s, σ_o = 0.005 Pa, and n = 0.80. K was held constant at 10,000 Pa..... 99

5-12: Astrocyte response and simulation results for cells on (A) Gel 1, (B) Gel 2, (C) Gel 3, (D) Gel 4. Mean AFM data shown in black with +/- standard deviation in grey and simulation results with parameters calibrated to data for each gel and listed in Table 5-3..... 100

5-13: Astrocyte response and simulation results for cells on (A) Gel 1, (B) Gel 2, (C) Gel 3, and (D) Gel 4. Mean AFM data shown in black with +/- standard deviation in grey and simulation results with parameters obtained by taking the mean of optimized parameters obtained for all substrates (Listed as mean in Table 5-3)..... 101

5-14: Astrocytes grown on Gel 4 classified as round (A) or spread (B) with simulation results obtained with mean parameters for astrocytes on all substrates (Table 5-3) and round (C) and spread (D) with simulation results obtained using parameters optimized for all astrocytes grown on Gel 4 (mean in table 5-3)..... 103

6-1: Collagen gel cell culture system consisting of a thin upper layer containing cells and a thick lower layer with no cells..... 109

6-2: Confocal image of representative gel, containing both neurons and glia, showing cells are in close proximity and able to contact and communicate with one another. The cytoplasm is stained with calcein-AM (green) and the nuclei with Hoechst (blue). 110

6-3: Shockwave system set-up: needle hydrophone, Flexcell plate with cell cultures in collagen gel, Dolorclast machine, and computer running data acquisition system. 112

6-4: Mechanism of shockwave generation of Dolorclast machine: a compressed-air impulse accelerates a projectile in the gun; the projectile contacts the tip of the applicator; the resulting shockwave is delivered to object in contact with the tip. (Image taken from http://www.dolorclast.com/page_productinfo_devicebrochure.php)..... 113

6-5: Onda HNS needle hydrophone used for measuring pressures in collagen gels. From http://www.ondacorp.com/images/brochures/Onda_HNS_DataSheet.pdf..... 114

6-6: Characterization of the pressure signal measured at different locations in the Flexcell well in PBS with respect to the tip of the Dolorclast gun: (A) Centered, (B) at edge of tip, (C) off edge of tip. 116

6-7: Characterization of pressure signal of 2 consecutive pulses (A) and 10 consecutive pulses (B) in a Flexcell well containing PBS showing the time between pulses and the pressures reached for pressure trains taken at 15 pulses per second. 117

6-8: Characterization of the change in pressure signal between the first and tenth shock taken at a frequency of 15 shocks per second in a Flexcell well containing PBS. Zoomed in view of the first pulse (A) and the tenth pulse (B) in the series for 4 different sequences of 10 shocks showing the timing of the initial pulse is consistent but there is some variation in the timing of the tenth pulse, with the sample in blue arriving earlier than the other 3 samples. Zoomed in view of the first (C) and the tenth pulse (D) for a single pressure measurement showing the change in pressures reached between the initial and final shock. 118

6-9: Comparison of the shockwave obtained with the standard Dolorclast tip (red) and with a tip with elongated shaft (black). The longer tip produced an elongated shockwave. Measurements were taken in Flexcell wells in PBS. 119

6-10: Comparison of the shockwave generated with the high-powered gun (black), the normal gun (green) and the normal gun at reduced output (red). 120

6-11: Characterization of the reproducibility of the shockwave when switching between 8 different wells containing unseeded collagen gel and culture media..... 121

6-12: Pressure profiles measured in 3 wells containing collagen gels seeded with astrocytes. The full signal including reflections is shown in (A) and a zoomed in view of the initial shockwave is shown in (B). 122

6-13: Viability assay on astrocytes subjected to one shock (A, B) and Control samples (C, D). Live cells labeled with Calcein-AM (Green) and dead cell nuclei labeled with Ethidium Homodimer 1 (Red). 123

6-14: Schematic of the key components of the custom voice coil device used to compress cell cultures. 124

6-15: Compression device and cell culture set up in the laminar floor hood (A) and being used to compress cell cultures in a 24 well plate (B). 125

6-16: Reproducible displacement and force profiles obtained for compressive loading of collagen gels at 1 Hz (A, C, E) and 10 Hz (B, D, F) for 6 wells tested at each rate. 126

6-17: Percent viability for control neuron samples as well as those compressed once at 0.01 Hz and 1 Hz. Data taken from counts of live and dead cells in representative images taken throughout the collagen gel constructs. 127

6-18: Viability assays for neurons deformed to approximately 20% strain at 1 Hz (A) and 10 Hz (B), and for control with no contact (C), and with contact with gel (D). Live cells labeled with Calcein-AM (Green) and dead nuclei with Ethidium Homodimer 1 (Red). 129

6-19: Viability assays for co-cultures of neurons and glia deformed to approximately 20% strain at 1 Hz (A) and 10 Hz (B), and for control with no contact (C), and control with contact with gel (D). Live cells labeled with Calcein-AM (Green) and dead nuclei with Ethidium Homodimer 1 (Red). 130

List of Tables

3-1: Height estimates of neuron soma determined with both AFM height determination methods and confocal imaging Z-stacks. 60

3-2. Ratios of Acrylamide (AA) and Bis-acrylamide (Bis-A) used to create gels and the measured Young's Moduli (E). Data taken over 2 gel sample preparations and at multiple locations on each sample. 62

4-1: Distribution in parameters (mean and data range) obtained by fitting model response to experimental data for 33 cells, accounting for actual cell configuration by varying the model geometric parameters to match the measured height and cell radius. K was assumed to be constant for all cells and set at 10,000 Pa. 75

5-1: Dimensions of neurons and astrocytes grown on substrates of varying stiffness (mean +/- standard deviation) obtained from confocal images. 91

5-2: Model parameters obtained by calibrating simulated response to mean AFM force data for neurons grown on different substrates. K was held constant at 10,000 Pa for all simulations. 94

5-3: Model parameters obtained by calibrating simulated response to mean AFM force data for astrocytes grown on different substrates. K was held constant at 10,000 Pa for all simulations. 98

6-1: Specifications reported on the Dolorclast device. Adapted from Kearney [4]. 113

Chapter 1

Introduction

A thorough understanding of the biomechanics of the central nervous system (CNS) is essential for understanding injury and pathology. While there are large bodies of research on the morphology, biochemistry, and electrophysiology of CNS cells, there is comparatively very little information on their biomechanical properties. Research dealing with the causes and disease progression of traumatic brain injury (TBI) is one area that would benefit greatly from a better characterization of the biomechanics of all cell types present in the CNS. CNS cells include neurons and glial cells, with glial cells consisting of astrocytes, microglia and oligodendrocytes. Glial cells were discovered in 1856 by a German pathologist, Rudolf Virchow [5] and named based on the idea that glial cells served as glue to hold the neurons together. Since their discovery, it has been shown that glial cells have many critical roles in brain function and the response to injury. Astrocytes perform a variety of functions in the CNS including release of neurotransmitters and synthesis of extracellular matrix (ECM) molecules [6-8]. They are also

involved in the process of synaptic neurotransmission and are capable of dynamically changing the coverage of synapases [9-11]. In addition, unlike neurons, which are excited electrically via action potentials, astrocytes can be excited non-electrically. Oligodendrocytes play critical roles in myelination and microglia are involved in the host defense system. Microglia respond to chemokines released by astrocytes and localize to sites of injury during inflammation responses [11]. In addition, both neurons and glia are involved in the cell response after TBI. A better understanding of the biomechanics of neurons and glia will fill an important gap in characterizing the cellular response to mechanical trauma.

TBI is the result of various types of mechanical loading on the brain. A blow to the head, motor vehicle accident, sports injury, fall, or shock wave from an explosion are all examples of forces that elicit a mechanical response at both the cellular and tissue level in the brain [12]. This mechanical response ultimately leads to a pathophysiological response involving both neurons and glial cells, and eventually leads to brain damage and observed behavioral and cognitive changes. While it is well established that various mechanical loading scenarios can cause brain injury, there is still work to be done to fully connect the initial mechanical response with secondary signaling and eventual damage. A key component to filling in this knowledge gap is to have tools to study TBI at the cellular level *in vitro*. This includes having computational models to simulate how cells deform under various types of mechanical loading, as well as developing *in vitro* damage devices to subject cells to a variety of mechanical insults. In addition, since the initiator of the damage cascade is a mechanical load, it is critical to have measurements of cells grown in a mechanical environment that is biologically relevant. These experiments are critical for determining cellular injury thresholds and identifying potential therapeutics.

The work presented in this thesis provides a characterization of the biomechanics of neurons and glia in addition to developing important tools for studying and quantifying TBI at the cellular level. It builds on what is currently known about the mechanical response of single neurons and astrocytes, as well as on the existing *in vitro* cellular damage systems, as described in depth in Chapter 2. This work contributes significantly to the basic knowledge of the biomechanics of CNS cells.

Both experimental and computational approaches are utilized in this thesis to quantify the response of neurons and astrocytes to mechanical loading. Chapter 3 describes the methods used to measure single cell properties and create computational models for both neurons and astrocytes and contrasts these with previously published methods. This includes atomic force microscopy (AFM) indentation techniques to test cells at three different loading rates and in relaxation, as well as the formulation of a finite element model used to characterize the cell response. The AFM and modeling techniques are applied to test cells grown on substrates of different stiffness. Results and discussion of the single cell experiments and simulations are presented in Chapters 4 and 5. Chapter 4 quantifies and compares the mechanical response of neurons and astrocytes grown on glass, while Chapter 5 expands on this work and presents results of cells grown on gels of different stiffness to address how the stiffness of the substrate influences the mechanical properties of CNS cells.

In addition, this thesis presents the design and preliminary characterization of two *in vitro* cell injury systems. Details on the systems are described in Chapter 6. One system compresses the cell cultures, simulating what might occur with an impact. The second system sends a shock wave through the cell culture, simulating loading associated with a blast wave from an explosion. Both systems utilize what was learned in Chapter 5 about the importance of substrate selection

on ensuring cells have morphology and force response similar to what would be expected *in vivo*, and damage the cells in a soft, 3-dimensional collagen gel. In addition, preliminary data and future plans for further characterizing the cellular damage and biochemical response are presented.

As summarized in Chapter 7, this thesis provides insight into how CNS cells respond to mechanical loading. The single cell models and measurements at a range of loading rates and on substrates of different stiffness provide a comprehensive characterization of the biomechanics of CNS cells in a variety of conditions and provide critical information for simulating TBI at the cellular level and determining damage thresholds. The quantification of cell properties, coupled with devices to damage cells *in vitro,* provides key tools to link well-defined stresses and strains to measured biochemical responses. These systems provide efficient ways to study TBI, identify new target molecules, and screen potential therapeutics.

Chapter 2

Background

2.1 Traumatic Brain Injury

TBI is a major cause of death and morbidity in the United States, affecting some 2 million civilians each year [13] and an estimated 20% of the 1.6 million veteran population returning from Iraq and Afghanistan [14, 15]. In addition, based on statistics collected from 2002 to 2006, the Centers for Disease Control and Prevention (CDC) estimated that TBI results in 1.365 million emergency room visits and 52,000 deaths each year in the United States [12]. They also found that TBI is a contributing factor in one third of the injury related deaths in the United States [12]. Cases of TBI can range from mild to severe, however, mild cases are much harder to diagnose, and as a result, accurate incidence estimates are hard to obtain. Mild TBI is characterized by a brief loss of consciousness (although not in all cases) and ongoing symptoms of headaches, dizziness, memory and concentration problems, and other behavioral and cognitive

changes [3]. Civilian TBI is often due to falls, sports injuries, and motor vehicle accidents, with falls being the leading cause of TBI and motor vehicle accidents being the leading cause of TBI-related death [12]. In the case of the veteran population, an additional cause of TBI is blast injury, which has become so prevalent in recent years it is often referred to as the signature injury of military troops today [16, 17].

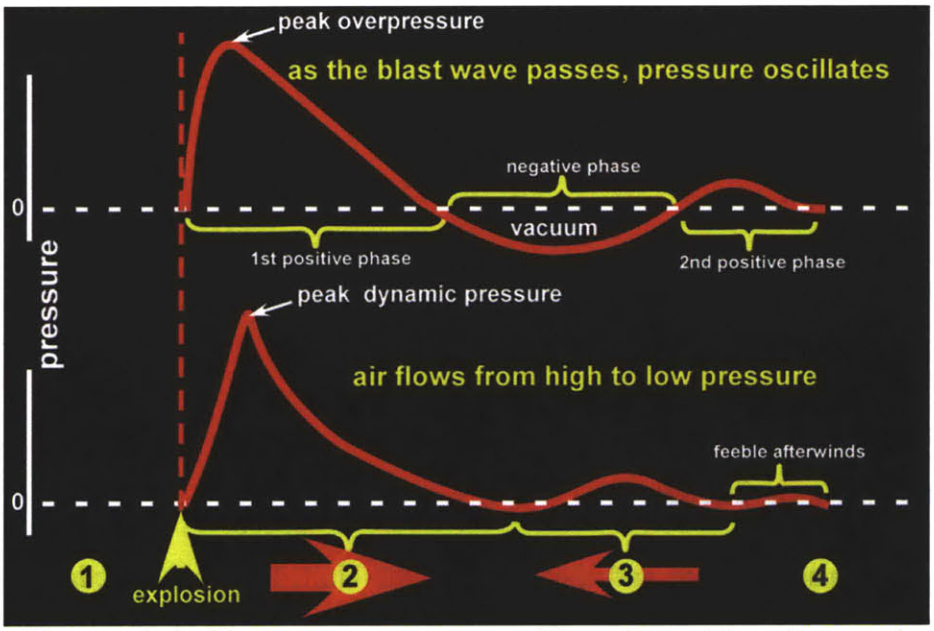

Figure 2-1: Characteristic blast wave pressure profile and resulting changes in atmospheric pressure. Before the explosion (1) atmospheric pressure is normal. After the explosion and upon passage of the shockwave (2), the blast wind flows away from the explosion. When a drop in atmospheric pressure occurs below normal, the direction of the blast wind reverses (3). Reproduced with permission from Taber *et al* [1]

Blast TBI (bTBI) is caused by the interaction of a shockwave with the brain. After an explosion, the blast wave rapidly expands and propagates through the air and tissues. The blast wave is characterized by a near instantaneous rise in pressure followed by a decay profile reaching negative pressures (Figure 2-1). This quick rise in pressure results in a blast wind due to the kinetic energy transmitted to the air particles. bTBI is classified into four main categories, depicted in Figure 2-2 [14, 16-18]. Primary blast injury results from the shock wave itself. The

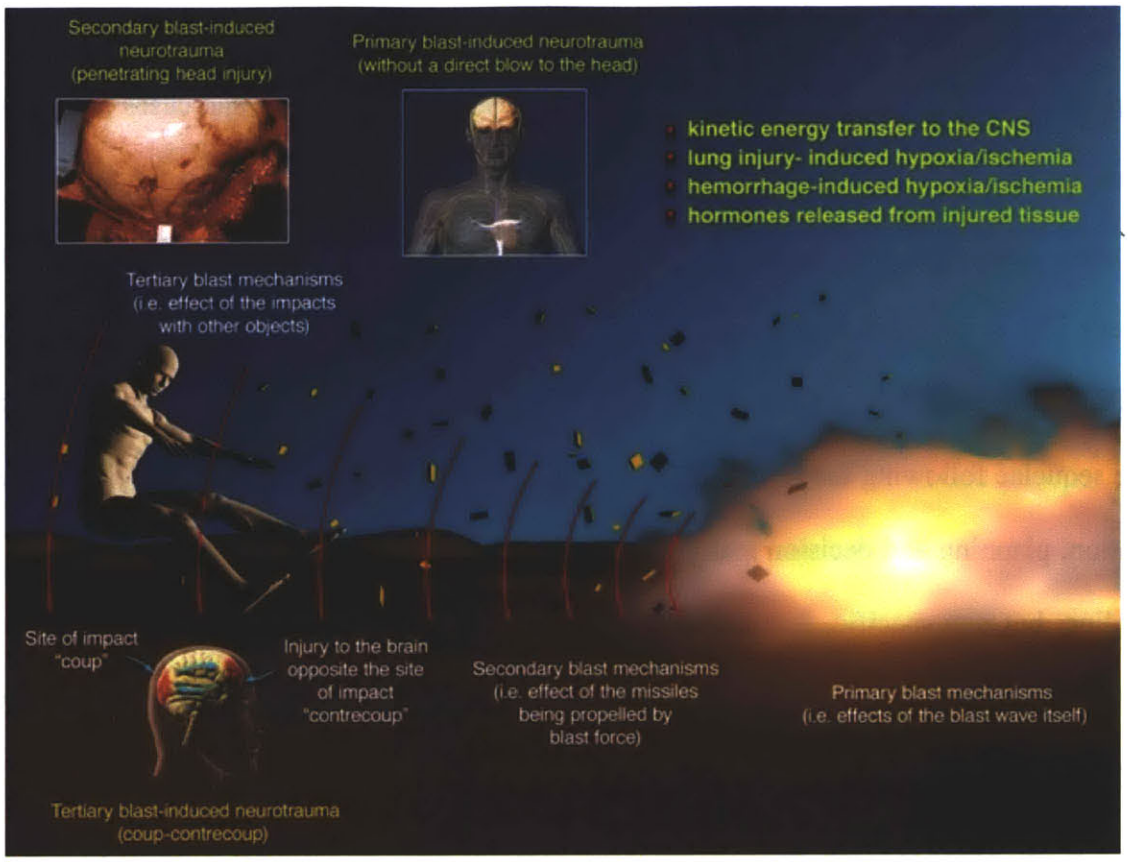

Figure 2-2: Schematic of the primary, secondary, and tertiary blast mechanisms and the characteristic brain injuries. Reprinted with permission from Macmillan Publishers Ltd: Journal of Cerebral Blood Flow and Metabolism, copyright 2010 [2]

shock wave consists of both over and under-pressures that travel through the brain tissue and act to compress and stretch the tissue. In addition, shockwaves can be concentrated and reflected at air-fluid interfaces, rendering certain regions of the body especially vulnerable. Typical shockwaves take place over millisecond timescales, but the exact pressure profile changes with the type and size of the explosive [16]. In secondary bTBI, shrapnel penetrates the head and causes damage. Tertiary injury occurs when the head is accelerated by the blast wind, potentially causing impact with surrounding objects. Finally, quaternary injury includes all other factors not accounted for in the first three phases. This could include chemical or thermal burns or breathing problems from smoke inhalation. Often, primary blast injury can be classified as mild TBI, or

concussion, and results in a brief loss of consciousness or altered mental status [17]. Mild bTBI is especially hard to diagnose but the consequences are still significant and cases are prevalent. In two studies of sample populations of U.S. soldiers, 15-16 % [17, 18] were found to have symptoms consistent with mild TBI. In addition, based on the most up-to-date numbers for military TBI in Iraq and Afghanistan (shown in Figure 2-3), it is clear that the vast majority of the TBI occurrences fall in the group of mild TBI, a category based on the characteristics of the acute sequelae following the injury. Memory and executive dysfunction (e.g. deficits in selective attention, planning and decision making, cognitive flexibility) are among the most common and disabling, but non-specific, features of mild bTBI. The prevalence of bTBI highlights the need for a better understanding of damage thresholds, injury progression, and potential therapeutics and preventative measures for both mild and more severe forms of bTBI.

Blast TBI has been studied in various animal models, showing that the primary blast wave alone is sufficient to cause TBI [19-29]. The animal studies indicated the involvement of both neurons and glial cells in the injury response. For example, Kaur and colleagues found both microglia and astrocytes to be activated in rats after being subjected to an explosive-generated blast [21, 25, 26]. Changes in neurons after blast injury have also been detected in animal models. For instance, Kato *et al.* studied the effects of a blast on rats and showed the characteristics of neuronal damage varied with the magnitude of the overpressure. Pressures greater than 10 MPa resulted in an increase in TUNEL positive neurons, indicating involvement of apoptotic signaling pathways. For lower overpressures (1 MPa), morphological changes in neurons were identified, with neurons taking on a spindle shape and their nuclei becoming elongated [29]. Despite recent advances from what has been learned in animal models of blast TBI, there remains a need for a better understanding of the damage progression and injury

thresholds, especially at the cellular level, to enable development of preventative measures and potential therapeutics.

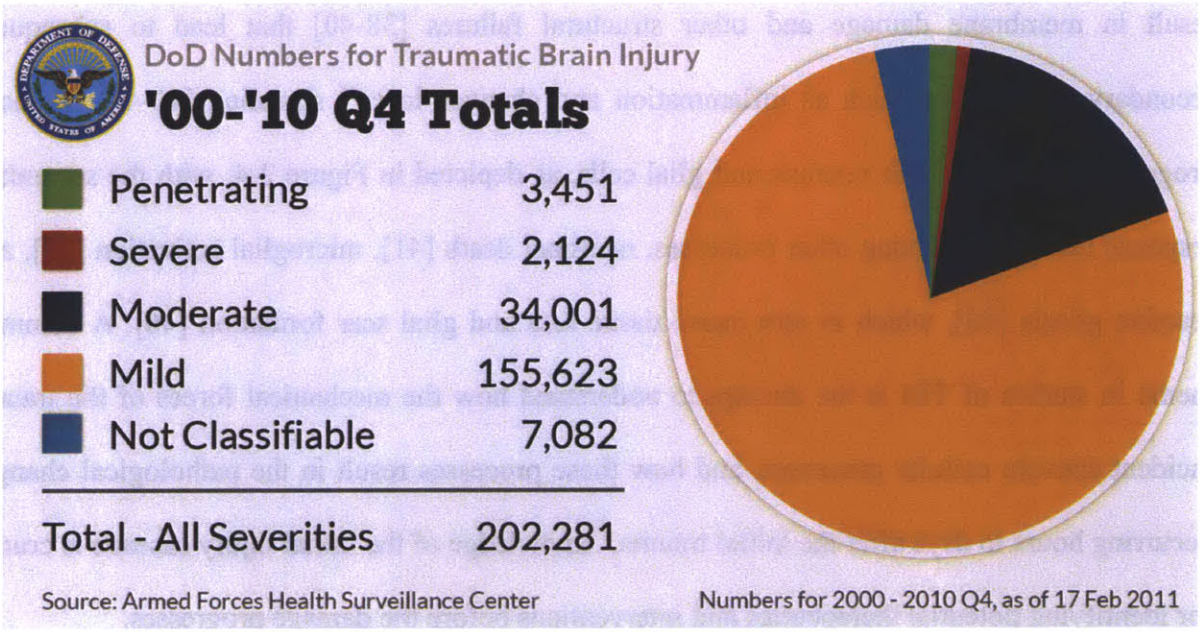

Figure 2-3: Official Department of Defense numbers for different severities of Traumatic Brain Injury (from http://www.dvbic.org/TBI-Numbers.aspx)

While the most common damage occurrences leading to mild or moderate forms of TBI (e.g. motor vehicle accidents or falls [30-32], sports concussions [33-35], and blast exposures [1, 32, 36, 37]) have been widely acknowledged and thoroughly reviewed, the etiology of the ensuing cognitive, behavioral or neuropsychological disorders/impairments (e.g. memory loss, language difficulties, concentration deficiencies, behavioral abnormalities and/or depression) remains poorly understood. In particular, little is known about the multiple damage mechanisms suspected to unfold at the CNS cell level in the seconds to hours (and probably days) following initial mechanical insult(s) to the brain, and likely to result in cell/tissue alteration.

Cellular damage following TBI is a complex process involving both the initial damage caused from deforming the cells and tissue and secondary cellular responses involving diverse

damage pathways. Due to the time lag between the initial primary damage and secondary injury, there is hope that a better understanding of secondary damage mechanisms could lead to meaningful therapeutics and minimization of lasting damage [3]. The initial deformation can result in membrane damage and other structural failures [38-40] that lead to subsequent secondary mechanisms such as inflammation and changes in cell signaling [41-44]. Damage progression involves both neurons and glial cells, as depicted in Figure 2-4, with the secondary response leading to, among other processes, neuronal death [41], microglial activation [45], and reactive gliosis [46], which in turn cause tissue loss and glial scar formation [46]. A common theme in studies of TBI is the attempt to understand how the mechanical forces of the trauma incident activate cellular processes, and how these processes result in the pathological changes occurring hours to days after the initial trauma. Knowledge of the initial injury cascade is crucial for identifying potential therapeutics and interventions before the damage progresses.

One of the immediate consequences of mechanical trauma is an increase in plasma membrane permeability or mechanoporation [38, 39, 47, 48]. This can be a result of mechanically activated ion channels as well as tearing of the membrane. While mechanoporation may not kill the cells, especially in mild TBI, it does result in changes in cell function, ion homeostasis, electrical activity, and cell signaling [49]. In addition, it causes conduction block [50], neurofilament compaction [42], and impaired axonal transport [51], suggesting a role in connecting initial mechanical damage with cell biochemical response. Increased membrane permeability after mechanical trauma has been shown in both animal models [38] and *in vitro* cellular models [52-54]. In addition, work at the cellular level has shown that P-188, a nontoxic, nonionic, tri-block amphiphilic co-polymer that has been shown to reseal membranes, is able to block the mechanically induced increase in membrane permeability [53, 54].

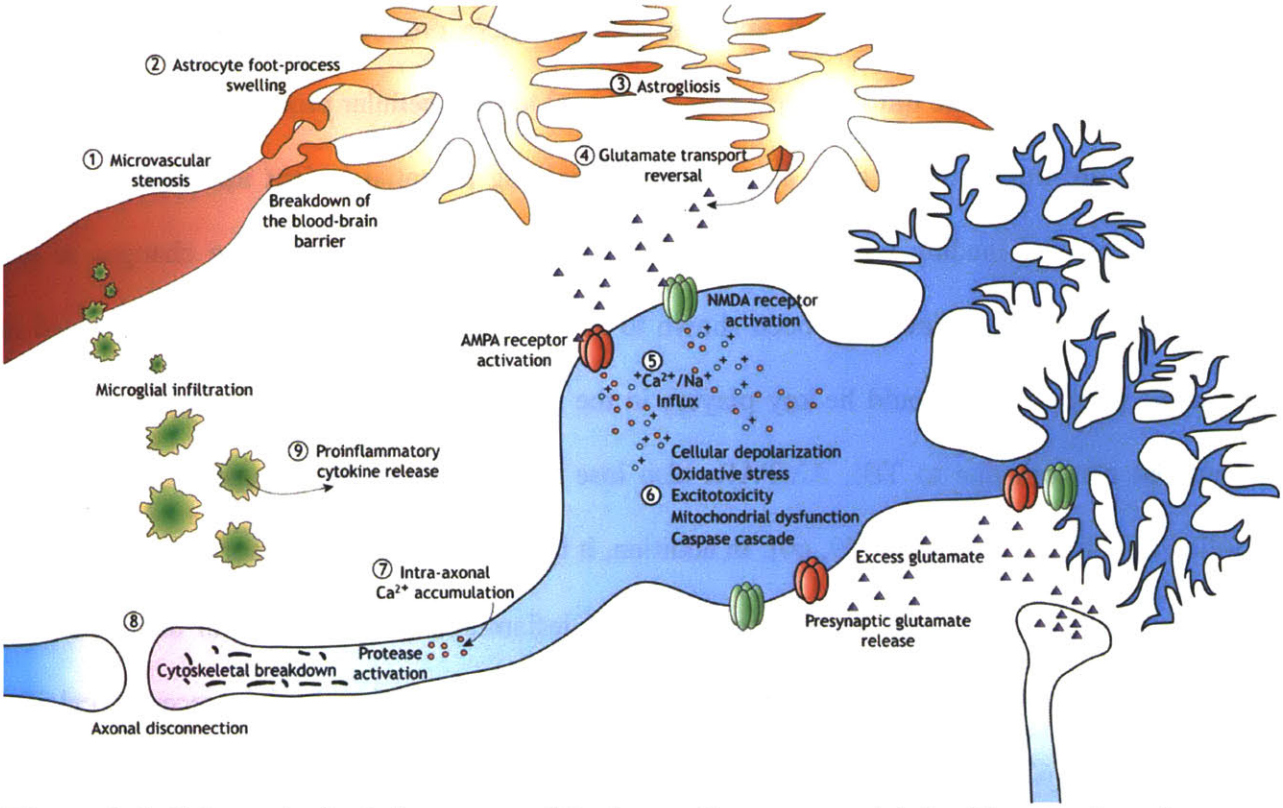

Figure 2-4: Schematic depicting some of the key pathways associated with secondary damage after TBI, involving neurons (blue), astrocytes (orange), and microglia (green). Reproduced with permission from Park *et al.* [3] © Canadian Medical Association. Copied under license from the Canadian Medical Association and Access Copyright. Further reproduction prohibited.

Excitotoxicity also occurs after TBI, as a result of an increase in extracellular concentration of glutamate, an excitatory neurotransmitter (for a detailed review see Yi and Hazell [55]). This increase in glutamate levels is thought to also be involved in the toxic increase in intracellular calcium levels following TBI [3]. In neurons, abnormal calcium homeostasis is involved in cell death processes. Changes in the glutamate receptors are among the causes for the observed increase in glutamate levels. There are two main classes of glutamate receptors, N-methyl D-aspartate receptors (NMDARs) and α-Amino-3-hydroxy-5-methyl-4-isoxazolepropionic acid receptors (AMPARs). NMDARs have been shown to be especially critical in the loss of ionic homeostasis after TBI [56]. For instance, they have been shown to be involved in the increase in cytosolic calcium levels [57]. NMDARs are also coupled to the

generation of reactive oxygen and nitrogen species. These products, coupled with other free radicals produced by the mitochondria eventually lead to fatal cellular processes [3]. In addition, NMDARs are linked to the actin cytoskeleton, providing potential insight into how stretch or other mechanical loading results in activation of NMDARs and the resulting changes in ion levels [58]. AMPARs have also been shown to be involved in TBI. AMPARs are involved in synaptic plasticity and could be key players in the immediate and long-term alterations of the neuronal network due to TBI. AMPARs also lose their desensitization property for 24 hours following mechanical injury [59, 60]. In addition, it has been shown that tumor necrosis factor α (TNFα), which is released from injured glia and inflammatory cells, leads to an increase in expressed AMPARs lacking the GluR2 subunit [61], a subunit involved in receptor calcium permeability [62]. As a result, this change in AMPAR subunit content could be a major contributor to the post-injury increase in calcium levels [3]. For a detailed review of the glutamate receptors and their role in TBI see Yi and Hazell [55] and Whalen *et al* [43].

The changes in levels of excitatory amino acids, free radicals, and intracellular calcium, along with many other complex pathways can ultimately result in loss of function and cell death. Cell death can occur via either a necrosis or apoptosis pathway. For detailed reviews of the cell death pathways see Raghupathi [41], Yuan *et al* [63], and Whalen *et al* [43]. Apoptosis, or programmed cell death, can occur as the result of multiple pathways, one of which involves the activation of death-inducing proteases. One class of proteases, the caspases, has been found to be activated in TBI [41, 43, 64]. It is believed that caspases cleave multiple proteins and the additive effects lead to cell death [65]. Cytoskeletal proteins, cell survival enzymes, and inhibitors of DNA endonucleases are all substrates on which the caspases act [43]. Work by Yakovlev and colleagues showed that cell death following fluid-percussion brain injury was

reduced when a caspase inhibitor was administered to the rats [66]. There are also both intrinsic and extrinsic pathways of apoptosis. The intrinsic pathway is triggered by the injured mitochondria. In the extrinsic pathway of apoptosis, membrane bound receptors such as Fas and TNFR1 are activated. This leads to recruitment of cytosolic adapter proteins. In turn, activated adapter proteins bind procaspases and form a death-inducing signaling complex (DISC). TNFRs are also involved in intracellular signaling pathways that can lead to cell survival. Activation of NFκB has been shown to be antiapoptotic and offers protection against TNF and Fas induced apoptosis by promoting increased transcription of antioxidant and antiapoptotic genes [43]. In addition, it has been shown that inhibition of Fas receptor and TNF-α improves neurologic function after brain injury in both adult and immature mice [43, 67].

Cell death following TBI can also occur via the necrosis pathway. Severe insults to the brain result in increased membrane permeability, organelle swelling, changes in both cellular and nuclear size and decreases in cell energy levels that lead to cell death [43]. This type of cell death is characterized as necrosis and occurs early in the damage progression and results in an inflammatory response [63]. There is also some work that suggests that necrosis can occur as a type of programmed cell death initiated by members of the tumor necrosis factor receptor family [68]. Since most of the damage leading to necrosis occurs early after injury, potential treatments targeting necrosis would need to be administered very soon after injury to be successful interventions.

Glial cells also play a unique and significant role in responding to CNS damage via a process known as reactive gliosis. Reactive gliosis involves hypertrophy and proliferation of microglia, astrocytes, and NG2 cells. Microglia are activated first [69], followed by increased proliferation of NG2 cells [70], and finally astrogliosis occurs [71]. Astrogliosis involves

astrocytes in the region surrounding the lesion responding to damage by proliferating, increasing process length, producing extracellular matrix, and increasing intermediate filaments and glial fibrillary acidic protein (GFAP) [7, 72, 73]. Initially, reactive gliosis has seemingly positive effects, minimizing tissue damage and helping to re-establish the blood-brain barrier [74]. Within days after injury, astrocytes "wall off" the damaged area and the resulting glial scar replaces the damaged neuronal cells. However, this glial scar is ultimately detrimental to neuron regeneration, as it has been shown that the neurites cannot penetrate the scarred region [46, 75].

The processes described in this section are just some of the complex cellular processes occurring after mechanical trauma that ultimately result in observed phenotypes associated with TBI. As described, these are complex processes involving both neurons and glial cells. Better understanding of these events requires not only knowledge of the activated biochemical pathways, but also a quantitative analysis of cell biomechanics, to truly connect the initial mechanical damage with injury thresholds and downstream cellular responses.

2.2 Biomechanics of Single Neurons and Glia[1]

One line of approach towards better elucidating some of the key damage mechanisms involved in TBI relies on addressing two distinct, yet interrelated, questions: (1) how mechanical transients applied to the organ boundary (head) translate into local stress–strain (force–displacement) distribution maps at the mesoscopic tissue level and microscopic cell level, and (2) how the cell machinery responds to these mechanical stimuli. An improved quantitative knowledge of material properties at the CNS cell level is necessary to understand the former on a quantitative

[1] Section 2.2 is adapted from [76] Bernick K.B., Prevost T.P., Suresh S., Socrate S. Biomechanics of Single Cortical Neurons. Acta Biomaterialia 2011;7:1210. with permission from Elsevier

basis and to better characterize the latter in a controlled environment. Such characterization inevitably calls for measurable external mechanical inputs (e.g. pressure waves and imposed deformation profiles) to be applied to the boundary of *in vitro* cell systems (e.g. two-dimensional (2D)/ three-dimensional (3D) cell culture constructs or organotypic tissue slices) in a reproducible manner so that the latter inputs may systematically be associated with reliable estimates of force and deformation magnitudes at the single cell level.

Probing mechanical properties of individual cells has been made possible in recent years through the advent of novel testing techniques (for a review, see *e.g.* [77-79]) including magnetic twisting cytometry [80-83], particle-tracking microrheology [84-86], atomic force microscopy (AFM) [87-92], micropipette aspiration [93-98], optical tweezing and stretching [99-102], and microplate rheometry [103-105]. The last three techniques, which have been successfully employed to characterize the deformability of certain cell types in suspension (*e.g.* red blood cells [95, 101], white blood cells [93, 96], Müller glial cells [102], chondrocytes [98], myofibroblasts [94], and pancreatic cancer cells [105]), may not be easily applied to CNS neuronal cultures because neurons *in vitro* form intricate networks of adherent cells interconnected via multiple processes whose continuous growth and viable maintenance require the support of a substrate. Magnetic twisting cytometry is a powerful measurement technique providing local material properties at the membrane level but is not suited to examine global properties at the cell body level. AFM, originally developed to image surfaces of inorganic materials with atomic resolution [106], has proven to be a highly versatile testing tool in mechanobiology, enabling the measurement of material properties at the cell/subcellular level over a large range of forces (from pico- to nanonewton levels), speeds (from quasistatic to dynamic load levels), and length scales (from nano- to micrometers) via a variety of tip

geometries [107]. The diversity in available AFM tip geometries allows for a range of experiments to be performed under various loading conditions. Sharp tips may probe local properties at the cytoskeletal level or fine cellular structures such as neuronal processes, while large spheres may provide global "homogenized" properties at the whole cell level. Although widely used to characterize the mechanical response of numerous cell types including fibroblasts [87], leukocytes [91], cardiac myocytes [90] and blood cells [89, 92], AFM has been infrequently utilized to examine the response of CNS cells.

Limited information on the material properties of neurons and glia is currently available in the literature. To our knowledge, only Lu *et al* [102] have reported dynamic mechanical measurements on single CNS neurons – with measurements conducted in the linear infinitesimal strain regime only. Elastic storage and viscous loss moduli were extracted from the force-displacement output of oscillating 3 μm spherical AFM probes actuated to small indentation depths at the cell surface. These measurements, aimed at characterizing some of the local viscoelastic properties of neural cells, could not provide significant insights into the global mechanical response of single neural cell bodies, nor were they directed at investigating the mechanical nonlinearities observed at finite deformation typical of anticipated cell response in TBI cases, for which strains larger than 15-20% may be expected [108-111]. Although astrocytes have been studied more readily than neurons, there is still limited information on the global mechanical response of astrocytes. In addition, there is considerable variation in reported moduli values. Shiga *et al* [112] used both force-mapping and contact mode AFM techniques to measure the elasticity and topography of membranes of astrocytes cultured on glass and found the cell membrane (and immediate underlying areas) above the nucleus to be relatively soft with an elastic modulus between 1 and 5 kPa when compared to the membrane above the cytosol, which

they measured to have an elastic modulus between 1 and 35 kPa. Vergara and coworkers also measured the mechanical properties above the nucleus of astrocytes grown on tissue culture plastic using force mapping methods, finding the Young's modulus to range from roughly 30 to 60 kPa [113], values considerably stiffer than those measured by Shiga *et al.* In contrast, using the same methods used for measuring properties of neurons, Lu *et al* found the elastic moduli of astrocytes to range between 300 Pa and 520 Pa [102]. While there are many experimental differences between these three astrocyte studies, one of interest is that Shiga *et al* and Vergara *et al* kept astrocytes in culture on stiff substrates, either on glass or on tissue culture plastic, for weeks before testing. In contrast, Lu *et al* acutely isolated astrocytes and measured their properties after the cells had only been exposed to glass for a short time period. This suggests that the culture conditions, especially substrate properties, could be one variable responsible for measured differences in astrocyte properties.

The influence of substrate properties on measured cell mechanical response is a very important issue when connecting *in vitro* measurements to those expected *in vivo*, especially when developing multi-scale mechanical models. It is well established that cells are able to sense their mechanical environment and respond in a variety of ways [114-121]. In the case of cells found in the CNS, astrocytes have been shown to change morphology and cytoskeletal content on substrates of different stiffness, appearing small and rounded on softer substrates and more spread on stiffer substrates [122-124]. In addition, astrocytes grown on soft gels have been shown to have less F-actin stress fibers running through the cell, while astrocytes grown on hard substrates have very distinct stress fibers [122]. In contrast, neurons have been shown to have increased neurite branching on soft substrates [122, 125] and a corresponding increased F-actin content [122], while their process length remains unaffected by substrate stiffness [126, 127].

Soft substrates also promote the maturation of neural stem cell derived neurons, supporting growth of long neurites and synaptotagmin positive presynaptic terminals [128]. Further influence of substrate stiffness on neural stem cell behavior was shown by Saha and colleagues [129]. They found that in mixed differentiation conditions, that should favor both neuron and glial cell development, the proportion of neurons versus glial cells was dependent on the modulus of the substrate. In addition, soft substrates have been shown to select for neuronal growth over glial cell growth, with stiff materials allowing for more astrocyte spreading and adherence when compared with soft substrates [122]. In some cases, soft gels have been shown to result in glial cell death, with only neurons surviving [125]. In 3D culture systems, stiffness of the gel matrix has been shown to alter morphology as well. The mechanical stiffness of agarose gels has been shown to correlate inversely with the rate of neurite extension [130]. Sundararaghavan *et al* generated stable 1D gradients of mechanical properties in 3D collagen gels and showed that neurites favor growth down the gel stiffness gradient [131]. These observations show that the mechanical environment influences both neurons and astrocytes and is an important factor to consider when studying processes *in vitro* at the cellular level, especially mechanical phenomena such as TBI.

In order to develop accurate single cell mechanical models as well as multi-scale models, encompassing cell, tissue, and organism level data, it is very important to have accurate predictions of cellular properties *in vivo*. One major difference between cells *in vivo* and cells typically grown in tissue culture is the mechanical environment surrounding the cell. Brain tissue is one of the softest tissues in the body with a measured modulus reported on the order of a few kPa [132]. This is significantly different from traditionally used tissue culture plastic or glass, which are essentially rigid with moduli on the order of GPa. One way to begin to investigate

potential differences between *in vivo* and *in vitro* cellular mechanical properties, stemming from the mechanical environment surrounding the cell, is to grow cells on substrates of varying stiffness. While this cannot completely encompass the intricacies of an *in vivo* environment and all the extra cellular matrix interactions present in a 3D tissue environment, it does provide a measure of how sensitive cells are to changes in their mechanical environment and how much deviation from true *in vivo* properties may be observed in cells grown and tested on hard substrates such as glass or tissue culture plastic.

A critical component to understanding AFM data and creating models capable of accurately capturing the single cell response is the development of material models. AFM mechanical measurements conducted at the (whole) cell level on cell types other than neurons and astrocytes have been interpreted quantitatively with the aid of various continuum models. The modeling approaches most commonly used borrow their formulation from the contact theory developed by Hertz for linear elastic materials [87, 102, 133-135], many of which typically incorporate time-dependencies inherent in the cell response [87, 102]. The Hertz contact theory, however, relies on highly reductive assumptions including linearity, homogeneity, infinitesimal deformation, and infinite substrate dimensions – all of which are unlikely to hold for biological cell systems submitted to mechanical transients. In order to address some of these limitations, investigators have proposed alternative continuum approaches integrating part of the complexities observed in the mechanical response of biological cells. These approaches include piecewise linear elastic variations [136], linear hyper-elastic/viscoelastic composite material formulations [92, 137, 138], and biphasic linear elastic constitutive relations [139, 140]. More complex variations borrow elements from continuum and piecewise continuum models [141]. While successful at capturing specific quantitative features of the cell response under selected

test conditions, these formulations do not account for the combined strain and strain-rate nonlinear dependencies inherent in the cell behavior, as substantiated by a growing body of experimental observations [90, 104, 142]. These limitations highlight the need for new single cell models capable of capturing all aspects of typical cell responses, such as time and rate dependencies and non-linearities, and under a variety of loading conditions. Development of such models for neurons and glia would provide an improved quantitative understanding of the biomechanics of CNS cells and the resulting models would be useful tools in the study of TBI.

2.3 Existing Cellular Level Models of Traumatic Brain Injury

While measurements of cell response to mechanical loading and development of single cell material models provide important tools for the study of TBI and analysis of deformation gradients, additional tools to reproduce TBI at the cellular level *in vitro* are also needed to provide a more complete understanding and simulation of the complex processes unfolding at the cellular level after TBI. *In vitro* models of TBI provide important complementary information to *in vivo* experiments and clinical case studies. Studying TBI *in vitro* at the cellular level allows investigators to more precisely control for the influence of different cell types and key molecules in the damage cascade. Cell studies can be performed on individual cell types or on co-cultures, enabling investigation into how the various cell types interact. They provide a streamlined, well-controlled system, eliminating complexity from systemic responses of the body and also enable high throughput analysis of potential biomarkers and therapeutics when compared to *in vivo* animal studies.

A range of systems have been developed to recreate TBI in cell cultures [56]. Some models utilize 2D cell cultures, while others are compatible with 3D cell cultures. Existing 2D

trauma models include substrate stretch [52, 57, 143-150], acceleration of culture flasks [151], elevation of pressure [152], application of a fluid pulse [153], induction of shear forces [154, 155], and direct scratching or cutting of cell cultures [156-160]. While studies done on 3D cell cultures are less common, models currently exist to deform 3D cell cultures in both compression [51] and shear [161-163].

One of the most widely used 2D damage systems is the substrate stretch injury model in which cells are plated on elastic membranes and a pressure pulse is used to stretch the membrane, and thus deform the cells. This system has many advantages, including enabling both uniaxial and biaxial stretch as well as the ability to stretch isolated regions of the cell cultures. Stretching isolated regions of the cultures enables study of how secondary damage propagates from injured to uninjured cells. In addition, strain rate and magnitude can be varied in this model system. Studies using the stretch injury model have identified calcium level [146], membrane permeability [52], ATP levels [149], cell death [157], and generation of excitatory amino acids and reactive oxygen species [148] as key consequences of damage. In order to compare different damage mechanisms using the substrate stretch system, Geddes-Klein *et al* subjected cortical neurons to both uniaxial and biaxial stretching [147]. While both injury models resulted in an increase in intracellular free calcium levels, the magnitude of the increase was much greater in biaxially stretched cells. In addition, in uniaxially stretched cells, blocking membrane channels stopped the increase in calcium levels, whereas in biaxially stretched cells, a significant portion of the calcium transient remained after blocking the channels. This suggests that biaxial stretching results in membrane tears along with the opening of membrane channels. Stretch devices were also used to investigate how damage propagates from stretched regions to undeformed regions of the cell culture. For example, using a uniaxial stretching device to stretch

a subset of neurons in a culture, Lusardi and colleagues observed an increase in calcium levels, not only at the site of injury, but also in adjacent cells out of the range of the applied stretch [146]. Also, by controlling both the magnitude and rate of stretch, neuronal cells were found to be sensitive to both the magnitude and duration of the applied stretch [146]. In addition, stretch models have been used to identify differences in the levels of response and damage in cells from different regions of the brain (cortical, hippocampal, cerebellar). For example, Geddes *et al* found hippocampal neurons to respond differently than cortical neurons after mechanical stretch injury [149]. Hippocampal neurons had a larger increase in intracellular calcium concentration and exhibited a delay in the ATP deficit when compared to cortical neurons. These differences may be due to increased NMDA receptor densities and lower energy capacities in hippocampal neurons. An advantage of the cell stretching devices is the ability to apply controlled, sub-lethal mechanical stretches. Arundine *et al* exposed cells to sub lethal injury and then studied biochemical responses such as generation of reactive oxygen species and how these responses predisposed the cells to be more susceptible to secondary insult [148]. This may be applicable to mild TBI, and additionally, provides insight into what happens after cumulative insults to the brain. These studies highlight the diverse studies being carried out with cell stretching devices to better understand what happens at the cellular level in TBI and identify key variables in the damage response.

While the 2D stretch injury model provides significant insight into what happens at the cellular level during TBI, it requires cells to be grown in a very different mechanical environment than what is found *in vivo*. To address this limitation, it is useful to study cells grown in a 3D environment with similar mechanical properties to that of brain tissue. 3D cell culture environments, such as soft matrices or hydrogels, likely yield cells with characteristics

which are more similar to cells *in vivo* than to cells grown in 2D culture configurations [117, 164]. To address this issue, devices have been developed to induce injury in 3D cultures. 3D cultures offer the advantage of providing an environment with similar stiffness to that of brain tissue, as well as enabling a more accurate approximation of the structure and orientation of cells in the brain. Cell-cell and cell-matrix interactions are more complex *in vivo* and the use of a 3D culture system provides an important intermediate step between 2D cultures and tissue slices. LaPlaca and coworkers have designed a system to deform cultures in 3D [161]. They created a Sylgard cell chamber with top plate that enabled the 3D cultures to be deformed in shear. This device has been used in subsequent studies to examine membrane permeability [162] and compare damage in 2D and 3D cultures [163]. In addition, 3D neuron and glia cultures have been tested at different loading rates in compression [51]. These devices provide an important increase in complexity over 2D cultures, approximating the mechanical environment of tissue, while maintaining the simplicity of a cell culture level study.

As outlined above, considerable work has been done to recreate TBI in cell culture models; however, very little work has been done to study the effect of a shock wave on cell cultures. One study has examined the effects of overpressure on astrocytes. VandeVord *et al* designed a barochamber to simulate overpressure conditions similar to those of various head injury studies [165]. Their device generated a maximum overpressure of approximately 270 kPa with an average positive impulse of 3.239 +/- 0.848 kPa s. They looked specifically at the effects of pressure on astrocytes and examined changes in expression of apoptotic, reactivity, and survival genes at various time points after exposure to the overpressure wave. Initially, they found elevated levels of survival genes, followed at later time points by a decrease in expression of apoptotic genes. The level of pressure used in this study was below the pressure threshold

previously reported to cause glial cell injury. In this study, cells were cultured in 2D on petri dishes. Pressure-pulse loading cells in 3D gels would be a more relevant culture system and would greatly expand on this work by approximating the configurations the cells are likely to take on in the brain.

The studies outlined in this section highlight the importance of several key factors in studying TBI at the cellular level. First, it is important to consider the environment in which cells are grown, as evidenced by the different results found for 2D versus 3D cultures [163]. Secondly, it is necessary to select relevant loading rates, as this has been shown to be a key parameter in the severity of the damage response [52, 146, 150, 154, 166]. This is likely due to the viscoelastic nature of the cells. Finally, it is important to select an injury model that is relevant to the *in vivo* damage to be studied, as results have been shown to change with the mechanism of damage [147]. Depending on the trauma to be studied, stretch, compression, shear, or pressure-pulse models may be more relevant mechanisms to damage the cells. While many tools for studying TBI *in vitro* at the cellular level are well developed, there remains a need for new systems to study TBI, especially blast TBI, in biologically relevant 3D cultures.

Chapter 3

Methods for Determining Cell Material Properties

3.1 Overview

The homogenized material properties of both neurons and astrocytes were determined with atomic force microscopy (AFM) indentation methods developed in this thesis. These methods enabled testing of cells at different loading rates and under stress relaxation. In the case of neurons, methods were developed to characterize both the soma and the processes. Properties of astrocytes were measured in the cell region containing the nucleus. In addition, the developed protocols enabled testing of cells grown on different substrates, providing information on how cell material properties are influenced by the properties of their substrate. Methods for

determining height and geometry information of single cells at the time of AFM testing were developed using a combination of AFM, bright-field microscopy, and confocal microscopy.

The AFM data were used to calibrate a material model and the experimental geometry measurements provided information for creation of a finite element geometry representing the cells. The resulting constitutive models, implemented in a three-dimensional finite element framework yielded novel single cell models of both neurons and astrocytes grown on substrates of varying stiffness. Results presented in Chapters 4 and 5 utilize the AFM experimental methods and finite element modeling framework described in this Chapter. These methods build on existing work by providing an in depth characterization of CNS cell response to mechanical loading, as well as yielding models to quantify and simulate the cell response.

3.2 Atomic Force Microscopy Measurements[2]

3.2.1 Cell Culture

Primary neuronal cultures were prepared from cerebral cortices of postnatal day 1 Sprague-Dawley rats (Charles River Laboratories, Wilmington, MA). Tissue was provided by the laboratory of Professor Sebastian Seung, following a protocol approved by the Committee on Animal Care at the Massachusetts Institute of Technology. The dissociation procedure was adapted from a protocol detailed elsewhere [167]. Briefly, isolated cortices were minced, rinsed 3 times in modified Hank's buffered salt solution (HBSS) containing 25 mM HEPES, and digested for 12 minutes at 37 °C with an enzyme solution containing 1 mM L-cysteine, 0.5 mM EDTA, 1.5 mM $CaCl_2$, 200 units Papain (Sigma, P3125), and 1 μg/mL DNAse (Sigma) in modified HBSS. Tissue pieces were rinsed twice in culture medium (Neurobasal medium

[2] Parts of section 3.2 adapted from [76] Ibid. with permission from Elsevier.

supplemented with 1X B27 and 1X Glutamax (Invitrogen, 21103049, 17504044, 35050061)) and gently triturated in 1 mL ice-cold culture medium through 1 mL pipette tips. The resulting suspension was passed through a 70 μm cell strainer (BD Falcon, 352350) and subsequently centrifuged at 20 g for 7 minutes. The cell pellet was re-suspended in culture medium prior to plating at ~10^4 cells/mL density on 35 mm round coverslips (Carolina Biological Supply, Burlington, NC) or polyacrylamide gels coated with 0.1 mg/mL poly-D-lysine (PDL) (Sigma, P7886). Cultures were maintained at 37 °C in a 5% CO_2 humidified atmosphere. 1 h after plating, cultures were rinsed to remove debris and non-adherent cells. To obtain astrocytic cultures, the same protocol was followed with the resulting cell suspension plated in tissue culture flasks in neurobasal culture media supplemented with 0.5X B27, 1X Glutamax, and 10% fetal bovine serum. Astrocytes were grown to confluence, removed with trypsin, and plated on substrates for AFM experiments (either PDL coated coverslips or polyacrylamide gels). For both neuron and astrocyte cultures, half the culture media was changed every 3-4 days.

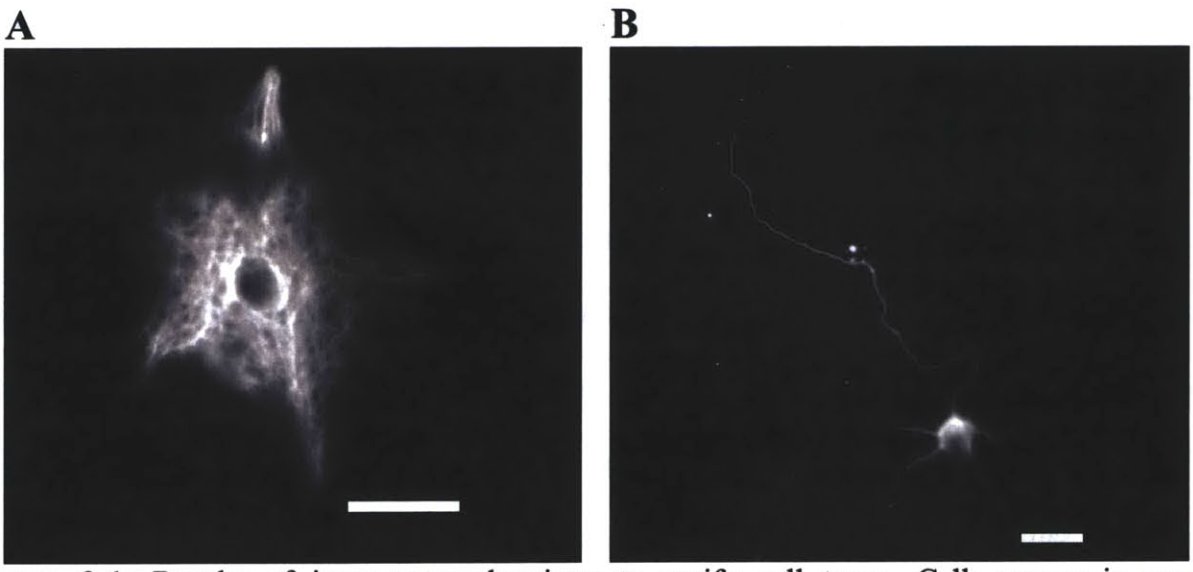

Figure 3-1: Results of immunocytochemistry to verify cell types. Cells grown in serum containing media were found to be primarily astrocytes (A) and those grown in serum free media primarily neurons (B). Scale Bars 20 μm

Immunocytochemistry assays were performed on representative samples to ascertain cell types. Anti-β-III tubulin (Abcam, ab24629) and anti-glial fibrillary acidic protein (GFAP) (Abcam, ab4648) were used to identify neurons and astrocytes respectively (Figure 3-1). Cells grown in serum free media were found to be primarily neurons and those grown in serum containing media were primarily astrocytes.

3.2.2 Measurements of Neuron Somata on Glass

Neurons were tested 5 days after plating, at which time they were well adhered with well-developed processes. Somata of single neurons were indented via an atomic force microscope (MFP 3D, Asylum Research, Santa Barbara, CA) mounted on an inverted optical microscope (Axio Observer.D1, Carl Zeiss MicroImaging Inc, Thornwood, NY). The mechanical probes selected for the tests were polystyrene spheres (45 μm diameter, Polybead® Microspheres; Polysciences Inc, Warrington, PA) mounted on tipless, triangular shaped silicon nitride cantilevers (Veeco Probes NP-OW, 0.06 N/m; Nanoworld PNP-TR-TL, 0.08 N/m). The microspheres were chosen deliberately larger than the cell soma in order to approximate loading conditions close to those prevailing in "uniaxial compression" experiments. The microspheres were attached to the end of the silicon nitride probes using UV curable Loctite 3211 glue and allowed to cure for 1 h under UV light. The size and positioning of the bead were verified for one representative sample via scanning electron microscopy (Figure 3-2 A). All tests, which lasted less than two hours, were conducted in culture medium at 37 °C in a fluid cell chamber (BioHeater™, Asylum Research, Santa Barbara, CA). Prior to testing, the spherical probe sitting above the sample was lowered into the medium and allowed to reach thermal equilibrium for about 30 min. Calibration of the spring constant was achieved for each probe using the thermal

method [168]. Cell viability was checked by visual inspection through the bright-field optical microscope during testing. Neurons were found to be well-adhered and visually healthy throughout the test procedure.

All tests were conducted under bright-field optical microscopy (Figure 3-2 B). The cantilever tip was positioned on top of the cell body via manual actuation of the micrometric screws controlling the horizontal X-Y positioning of the AFM optical stage. The center of the cell body was aligned with the vertical Z-axis of the indenting probe through the 20X magnification objective of the microscope (Figure 3-2 C). The indentation test sequence, implemented as a custom routine in IGOR Pro software (WaveMetrics, Inc, Portland, OR), consisted of an approach phase at 0.3 μm/s to a 0.3 nN contact force target (corresponding to an indentation depth of roughly 50-200 nm) followed by a 15 s dwell phase at contact with the cell body, and a subsequent series of load–unload segments at 10, 1, and 0.1 μm/s to 2 μm depth followed by a 120 s relaxation segment (Figure 3-2 D). The relaxation segment consisted of a 10 μm/s loading ramp to a target indentation depth of 2 μm held for 120 s. Note that at 2 μm indentation depth, which is roughly 14 to 40% of the height of the neuron soma, the influence of the nucleus on the measured cell response can no longer be neglected. The properties collected should therefore be viewed as global, "homogenized" properties of the whole cell body.

As cells may migrate, reorganize their cytoskeleton, and respond actively to external forces on timescales of seconds, a small population of neurons (N = 10) was tested in the reverse order of deformation rates, i.e. 0.1, 1 and 10 μm/s, to assess whether such cell activation processes could contribute significantly to the strain rate effects measured. The loading rates were selected to span the broadest range of deformation speeds compatible with the MFP 3D capabilities and the physical limitations pertaining to the test configuration.

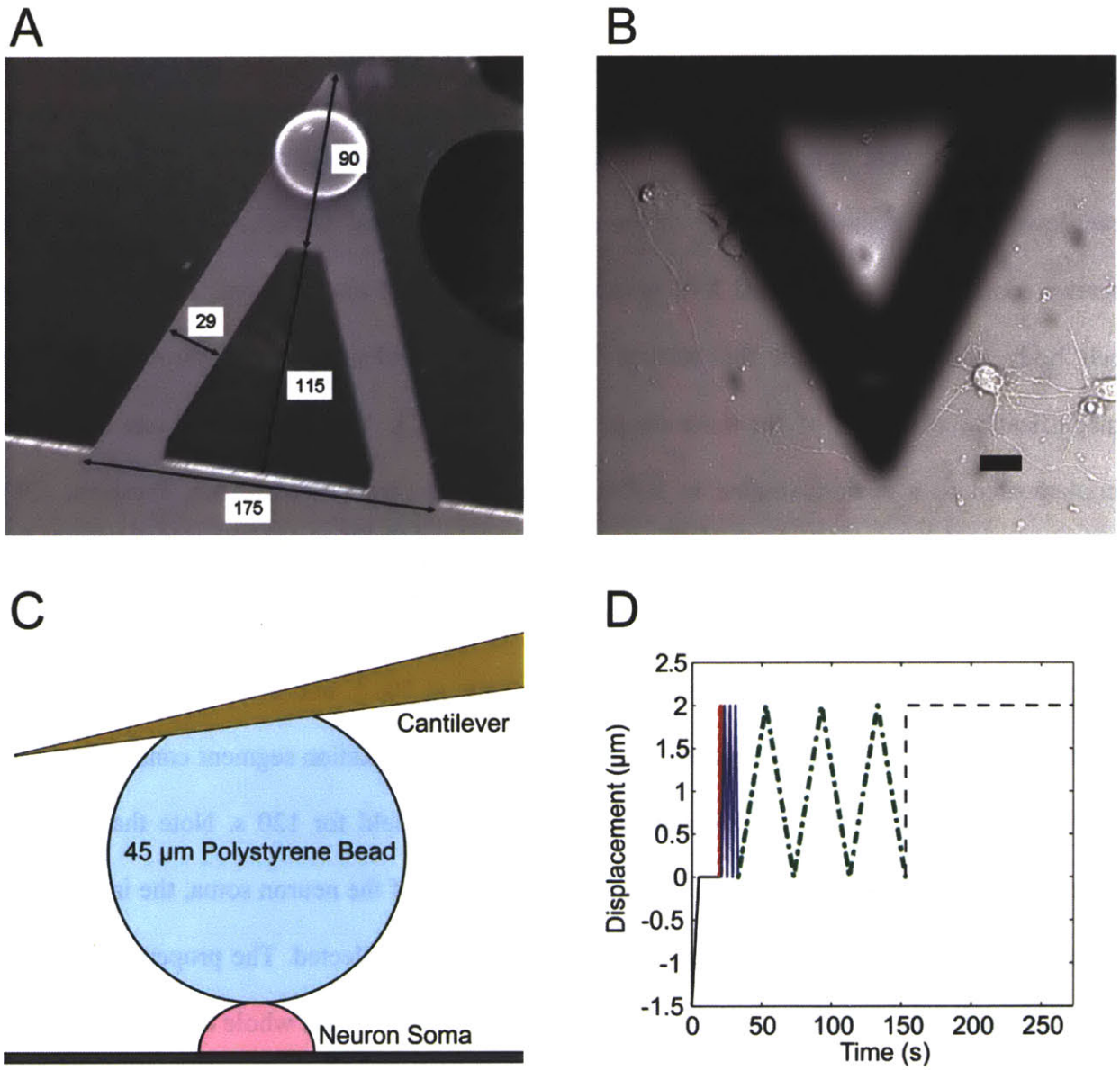

Figure 3-2: (A) SEM image of tipless cantilever with attached 45 µm polystyrene sphere (dimensions in µm). (B) Bright field image of AFM tip with bead adjacent to neuron to be indented; 20 µm scale bar. (C) Schematic of AFM experimental setup – Polystyrene bead compressing the cell body of a neuron plated on glass. (D) AFM testing procedure: sample approach, pre-load (black solid), sequences of load-unload segments at 10 µm/s (red dot), 1 µm/s (blue solid), 0.1 µm/s (green dash-dot), followed by stress–relaxation (black dash).

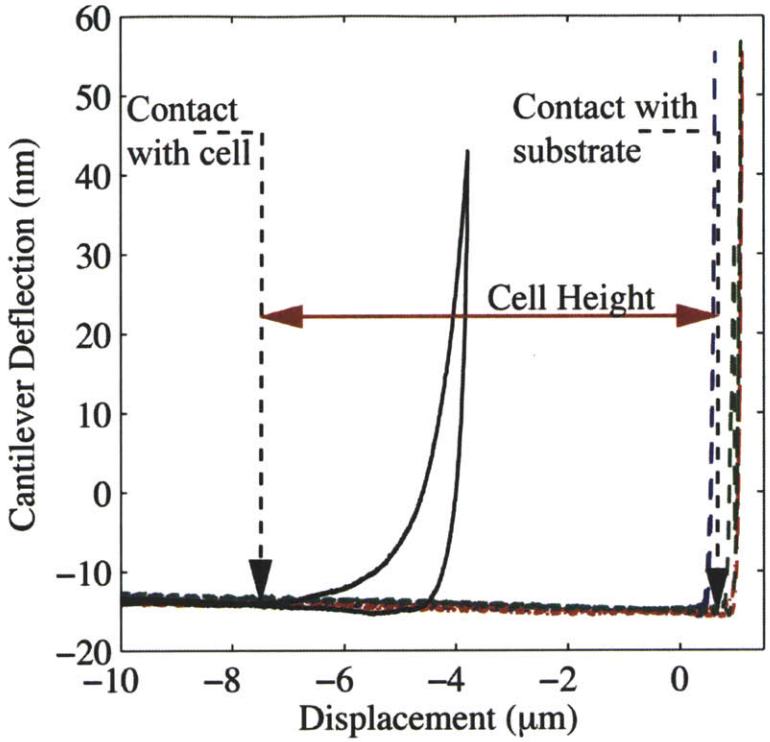

Figure 3-3: Cell height determination procedure: cell (black solid) and glass substrate (red, blue, green dash) indentation curves were used to retrieve relative piezo positions associated with contact events between cell/glass and cantilever, thereby providing an estimate for the cell height.

To account for some variations in the cell body size observed within and across cultures, height and "cross-diameter" estimates were collected for each cell body indented and incorporated in the 3D finite element simulations. The cross-sectional diameter, derived from the optical microscope images taken at the time of indentation (see *e.g.* Figure 3-2 B), was computed as the geometric mean between the largest and smallest edge-to-edge measured distances: $\sqrt{d_{\max} \cdot d_{\min}}$. Height estimates were obtained after completion of the indentation test, following a procedure adapted from previous cell height determination methods [92, 134]. Briefly, the cell body and 2-3 adjacent glass sites were indented at 10 μm/s extension/retraction rate to a target force of 4.5 nN. The differences in piezo positions at contact between cantilever and the cell body or the glass substrate were retrieved from the indentation curves to derive an estimate for

the cell height (Figure 3-3). The glass–cantilever contact point was determined as the intersection between the pre- and post-contact linear fit to the measured force–displacement indentation responses whereas the cell–cantilever contact point was recovered following a hierarchical Bayesian approach detailed in section 6.1 of Rudoy *et al* [169]. Briefly, the contact point and the pre- and post-contact regression coefficients were inferred – following Gibbs sampling techniques – from statistical distributions motivated by physical arguments. The post-contact force–displacement response in the small penetration depth regime was assumed to obey a polynomial law as predicted by the Hertz model for the response of an elastic substrate to indention by a rigid sphere (*i.e.* $F \propto d^{3/2}$, where F is the indenter force and d is the indentation depth). Use of the Hertz model to represent cell AFM response is widely established in the literature [170-172]. The height determination procedure was implemented in MATLAB.

3.2.3 Measurements of Neuron Processes on Glass

Neuron processes were also measured with the AFM. Processes were tested 5 to 6 days after dissociation and plating (Figure 3-4). Due to the small diameter of the processes, a pyramidal AFM probe, with radius of curvature less than 10 nm, was used (Nanoworld PNP-TR, 0.08 N/m). Processes were indented at 10 and 1 μm/s to a target force of 2 nN. Contact point was determined using the hierarchical Bayesian approach described previously for determining contact with the cell body for measuring neuron height [76, 169]. In order to obtain the pseudo-elastic Young's modulus for the processes, data were fit to the Hertz model for a conical indenter,

$$F = \frac{2}{\pi}\frac{E}{(1-\nu^2)}\tan(\alpha)\delta^2 \qquad (3.1)$$

where F is the force measured with the AFM, E is the Young's modulus, ν is the Poisson's ratio (assumed to be 0.5 in this case), α is the half angle of the AFM tip (35 degrees), and δ is the indentation depth. In order to avoid substrate effects, only the initial portion of the AFM force displacement curves were fit (roughly 600 nm).

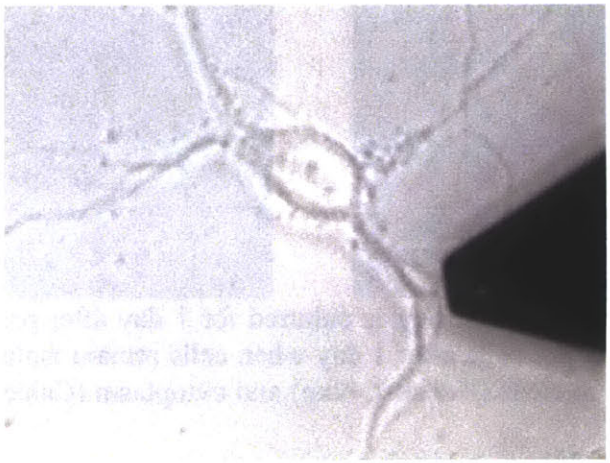

Figure 3-4: Representative neuron and AFM cantilever with pyramidal tip adjacent to process to be indented. Processes were indented close to the neuron soma.

3.2.4 Measurements of Astrocytes on Glass

Measurements of astrocytes on glass were performed in a similar manner to those described in 3.2.2 for neurons, with a few key differences due to the different morphology of astrocytes. Astrocytes were tested 1 day after passage. At this point, they were well adhered to their substrate and single cells were still easy to select for testing as shown in Figure 3-5 A. Due to the fact that astrocytes continue to divide in culture, waiting longer times after passage resulted in overlapping cells and less clear boundaries for single cells (Figure 3-5 B). In addition, due to the larger cell size of astrocytes, methods for whole cell compression and height determination developed for neurons were not applicable to the astrocyte samples. Finally, the indentation depth of the AFM loading routine was decreased to 1 μm to account for the decreased height of astrocytes when compared to neurons (Figure 3-6).

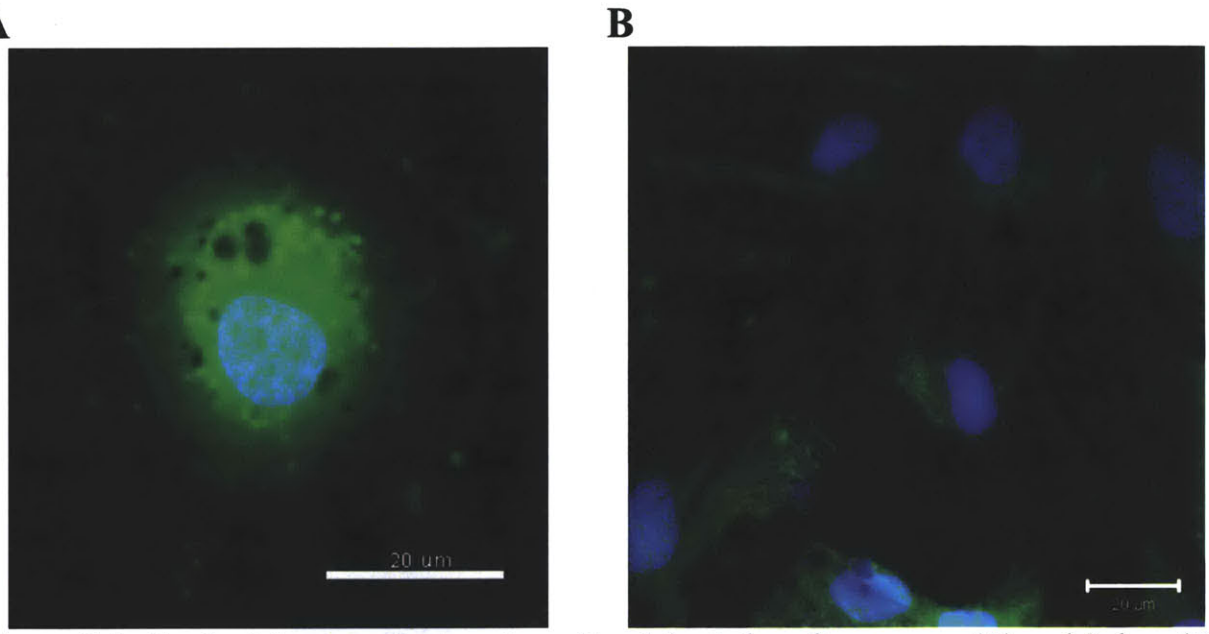

Figure 3-5: Confocal images of astrocytes cultured for 1 day after passage (A) and 3 days (B), highlighting the choice to test cells after 1 day when cells remain isolated and measurements on single cells are possible; nucleus (Hoechst, blue) and cytoplasm (Calcein-AM, green); scale bars 20 μm.

In order to obtain accurate cell geometry measurements, as well as information on the location of the nucleus relative to the AFM tip, the AFM was mounted on a confocal microscope (Zeiss LSM 700, Carl Zeiss MicroImaging Inc, Thornwood, NY) (Figure 3-7). Prior to AFM experiments, astrocytes were loaded with 2 μM calcein-AM (cytoplasmic stain; Invitrogen, L-3224) and 1.6 μM Hoechst 33342 (nuclear stain; Invitrogen, H3570) in PBS at 37 °C for 15 minutes. Following dye loading, cells were returned to culture medium and allowed to recover in the incubator at 37 °C for 45 minutes prior to loading on the AFM and testing. Use of calcein-AM, which only fluoresces upon entering a living cell, also verified the cells were viable at the time of testing. No morphology changes were observed upon addition of the dye. As a control, a small sample of cells grown on glass was tested both with and without the addition of dyes to test for any changes in material properties caused by the dyes. No changes were observed with the addition of dye (see Chapter 5, Figure 5-2 for results).

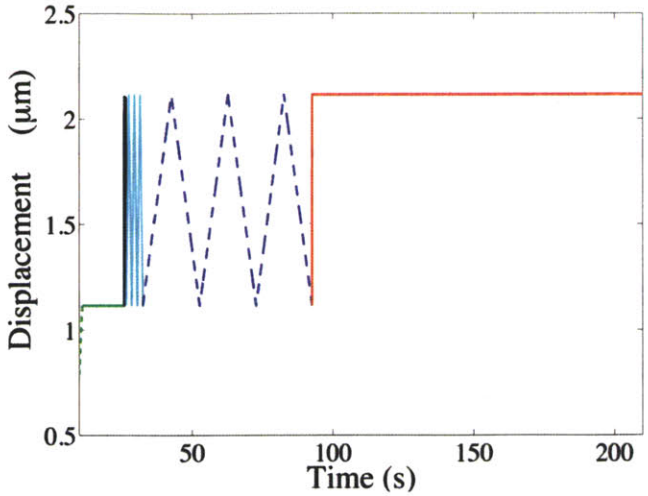

Figure 3-6: Astrocyte loading routine consisting of an initial approach to the cell to a pre-load of 0.3 nN to establish contact (green dash), a 15 s pause for equilibration (green solid), 3 sets of load-unload cycles to a 1 μm indentation depth at 3 different loading rates (10 μm/s (black solid), 1 μm/s (cyan solid), and 0.1 μm/s (blue dash)), and a 2 minute stress relaxation test (red solid).

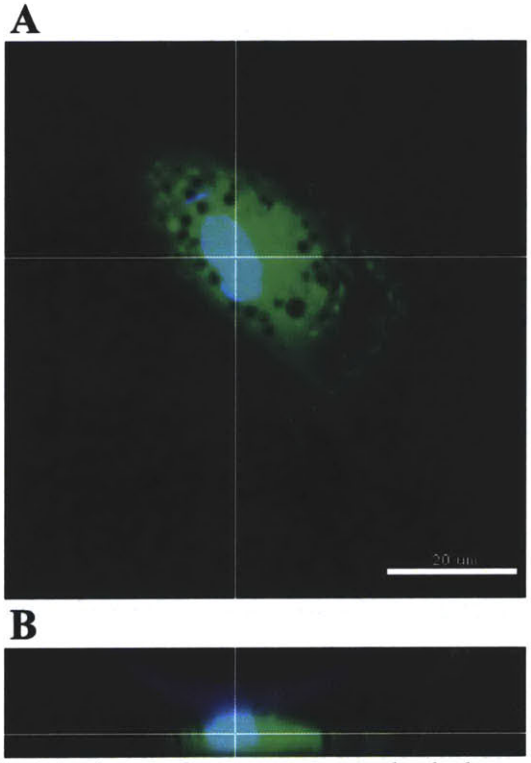

Figure 3-7: Top (A) and side (B) views of an astrocyte to be indented with polystyrene sphere (darker blue in side view); cytoplasm (calcein-AM; green); nucleus (Hoechst 33342; cyan)

Upon completion of the AFM testing procedure, a confocal Z-stack was obtained for each astrocyte. This enabled corresponding 3D geometry information for each set of AFM force curves. Confocal Images were taken after the AFM measurements to minimize any changes in cell properties due to the laser. Z-stacks were viewed in Zen (Carl Zeiss MicroImaging Inc, Thornwood, NY) and the heights of the cells, as well as the maximum and minimum diameters, were measured. An average cross-sectional radius for each cell was then computed as $\sqrt{R_{max} \cdot R_{min}}$. In order to ensure consistency of this height determination method with that described for neurons, height measurements for a sample of 10 neurons were taken with both the confocal Z-stacks and with the previously described height determination method utilizing the AFM to compare piezo position at contact with the cell and adjacent substrate [76]. The two methods produced comparable results as shown in Table 3-1.

Neuron	Height from AFM (μm)	Height from Confocal (μm)
1	9.85	9.93
2	8.39	8.32
3	9.95	9.89
4	7.10	7.12
5	7.48	7.56
Mean	8.55	8.56
Standard Deviation	1.32	1.30

Table 3-1: Height estimates of neuron soma determined with both AFM height determination methods and confocal imaging Z-stacks.

3.2.5 Measurements of Neurons and Astrocytes on Gels

Polyacrylamide gels of 4 different stiffnesses were prepared using a similar protocol to those described previously [114, 119, 123, 127]. 35 mm round coverslips (Carolina Biological Supply, Burlington, NC) were sterilized in ethanol followed by rinsing in distilled water. Coverslips were then washed in 0.1 N NaOH and allowed to air dry. Next, they were coated with (3-

Aminopropyl)trimethoxysilane (APTMS) (Sigma, 281778) for 4-5 minutes, followed by washing with distilled water. Coverslips were next coated with a 0.5% solution of glutaraldehyde (Sigma, G7526) in PBS for 30 minutes, washed in distilled water, and air-dried. Gel solutions were prepared in HEPES buffer from stock solutions of 40% acrylamide solution (Bio-Rad, 161-0140) and 2% bis-acrylamide solution (Bio-Rad, 161-0142) as described in Table 3-2. Polymerization was initiated with ammonium persulfate (Sigma, A9164) and N,N,N,N′-Tetramethylethylenediamine (TEMED) (Sigma, T7024). Solutions were passed through a 0.2 μm syringe filter and 100 μl were placed on the center of each activated 35 mm coverslip. A sterile, 25 mm round coverslip was carefully placed on top of the gel solution, being sure to avoid trapping any bubbles between the coverslips, and the gels were allowed to polymerize for 30 minutes. To facilitate removal of the top coverslip, the gels were soaked in 50 mM HEPES buffer (Sigma, 83264) and forceps were used to gently remove the top coverslip. In order to allow for binding of poly-D-lysine, the gel surface was activated with a coating of 0.5 mM Sulfo-SANPAH (Thermo Fisher Scientific, 22589) followed by exposure to UV light in a cell culture hood for 10 min. The gels were rinsed with 50 mM HEPES buffer and an additional treatment with Sulfo-SANPAH and UV light was performed. Gels were rinsed with 50 mM HEPES buffer and coated with 0.1 mg/mL Poly-D-Lysine (Sigma, P7886) for 4 hours. Gels were then rinsed and stored at 4 °C in PBS until use. This procedure resulted in gels of roughly 200 μm thickness as measured by light microscopy (Zeiss LSM700, Carl Zeiss MicroImaging Inc, Thornwood, NY) comparing Z position at the top and bottom gel surfaces.

Gel properties were measured using an AFM (MFP-3D-BIO, Asylum Research, Santa Barbara, CA). A 45 μm polystyrene bead was glued to a tipless AFM cantilever with nominal spring constant 2.7 N/m (AIO-TL, NanoAndMore, Lady's Island, SC). Gels were tested at 37 °C

in culture media to replicate the conditions of experiments containing cells. Gels were indented at 1 μm/s in scattered locations across gels from 2 different gel batches. In order to determine the Young's Modulus, E, AFM force-displacement curves were fit in MATLAB with the Hertz model [173] for a spherical indenter as described by equation 3.2.

$$F = \frac{4}{3}\frac{E}{(1-\nu^2)}\sqrt{R}\delta^{3/2} \tag{3.2}$$

where F is the measured force, R is the radius of the bead (22.5 μm), δ is the indentation depth, and ν is the Poisson's ratio. The Poisson's ratio was assumed to be 0.48 as used previously for polyacrylamide gels [123, 174]. To determine accurate indentation depths, contact point was determined independently of the Hertz model from a hierarchical Bayesian approach described previously [76, 169]. Cell properties were measured in the same way as on glass with geometry measurements taken with confocal microscopy methods as described for astrocytes in section 3.2.4.

Gel Number	AA (%)	Bis-A (%)	E (kPa) (mean +/- standard deviation)	N
1 (Softest)	5	0.07	1.682 +/- 0.0586	13
2	8	0.048	2.771 +/- 0.254	21
3	8	0.48	20.620 +/- 2.403	17
4 (Stiffest)	18	0.4	45.779 +/- 3.037	21

Table 3-2: Ratios of Acrylamide (AA) and Bis-acrylamide (Bis-A) used to create gels and the measured Young's Moduli (E). Data were taken over 2 gel sample preparations and at multiple locations on each sample.

3.3 Finite Element Simulations[3]

The mechanical data gathered on single neural somata and astrocytes, plated both on glass and on polyacrylamide gels, were interpreted with the aid of a finite element framework simulating

[3] Parts of section 3.3 adapted from [76] Ibid. with permission from Elsevier.

the experimental testing conditions. The continuum formulation selected for the homogenized "material properties" of the cell response is predicated upon the modeling framework developed in a recent study of the dynamic (macroscopic) behavior of porcine cortical tissue *in vitro* [175]. This formulation exhibits rheological features (*e.g.* rate effects, nonlinearities, conditioning, and hysteresis) similar to those observed at the single cell level. Briefly, the selected model comprises a hyperelastic network (A) accounting for the instantaneous response of the material and a viscoelastic resistance (BCDE) encompassing the strain rate/time effects prevalent at short (B) and long (CDE) time scales. A schematic of the rheological model is provided in Figure 3-8 A. As the model is intended to describe the cell response to large deformations, it is cast within a large-strain kinematics framework, using the concepts and standard notation of modern continuum mechanics (see, for example, Gurtin [176] or Holzapfel [177]).

Following Lee's decomposition [178], the total deformation gradient is expressed as:

$$\mathbf{F} = \mathbf{F}_A \cdot \mathbf{F}_B , \tag{3.3}$$

where $\mathbf{F}_A$ and $\mathbf{F}_B$ represent, respectively, the elastic (instantaneous) and viscoelastic (isochoric) components of the cell deformation. The viscoelastic response of the cell is captured by the combination of a nonlinear short-term viscous element (B) and a linear viscoelastic back stress network (CDE). With regard to the back stress network, the viscoelastic deformation gradient $\mathbf{F}_B$ is further decomposed as:

$$\mathbf{F}_B = \mathbf{F}_C \cdot \mathbf{F}_D , \tag{3.4}$$

where the linear viscous element (D) models the long-term relaxation of the back stress contribution. Both $\mathbf{F}_C$ and $\mathbf{F}_D$ are taken to be isochoric. The correspondence between deformation gradients and idealized rheological network components is shown in Figure 3-8 A.

The Cauchy stress $\mathbf{T}_A$ developed within the material is decomposed into its hydrostatic and deviatoric components:

$$\mathbf{T}_A = \mathbf{T}_h + \mathbf{T}_d, \tag{3.5}$$

where the hydrostatic component $\mathbf{T}_h$ and the deviatoric component $\mathbf{T}_d$ are physically associated with the deformation mechanisms prevailing in bulk and in shear.

The hydrostatic component $\mathbf{T}_h$ is obtained in terms of the volumetric jacobian, $J=\det(\mathbf{F})=\det(\mathbf{F}_A)$, according to the constitutive relationship:

$$\mathbf{T}_h = K \cdot \ln(J) \cdot \underline{\mathbf{1}}, \tag{3.6}$$

where K is the small-strain bulk modulus and $\underline{\mathbf{1}}$ is the second order identity tensor. The deviatoric component $\mathbf{T}_d$ is obtained in terms of the isochoric component of the elastic left Cauchy-Green tensor, $\overline{\mathbf{B}}_A = J^{-2/3} \cdot \mathbf{F}_A \cdot \mathbf{F}_A^T$, following a formulation derived from the freely-jointed 8-chain model for macromolecular elastic networks [179]:

$$\mathbf{T}_d = \frac{\mu_0}{J} \cdot \frac{\lambda_L}{\lambda} \cdot \mathcal{L}^{-1}\left(\frac{\lambda}{\lambda_L}\right) \cdot \left(\overline{\mathbf{B}}_A - \lambda^2 \underline{\mathbf{1}}\right), \tag{3.7}$$

$$\lambda^2 = \frac{1}{3} tr(\overline{\mathbf{B}}_A)$$

$$\mathcal{L}(\beta) = \coth(\beta) - \frac{1}{\beta}$$

where μ_0 and λ_L are model parameters which scale, respectively, with the initial shear modulus and the limiting extensibility of the network. $\mathcal{L}$ denotes the Langevin function.

The evolution of the viscoelastic component of the deformation gradient, $\mathbf{F}_B$, is constitutively prescribed through the nonlinear reptation-based viscous element (B), adapted from Bergstrom and Boyce [180]. The deformation gradient time derivative, $\dot{\mathbf{F}}_B = \mathbf{F}_A^{-1} \cdot \tilde{\mathbf{D}}_B \cdot \mathbf{F}$ is

obtained by aligning the stretching tensor $\tilde{\mathbf{D}}_B$ with the direction of the (deviatoric) driving stress $\mathbf{T}_B = \mathbf{T}_d - \mathbf{T}_C$, where $\mathbf{T}_C$ is the backstress from element (C), through the constitutive relationship:

$$\tilde{\mathbf{D}}_B = \dot{\gamma}_B \cdot \tilde{\mathbf{N}}_B = \dot{\gamma}_B \cdot \frac{\mathbf{T}'_B}{\sqrt{tr(\mathbf{T}'^2_B)}} = \dot{\gamma}_0 f_R \left(\frac{\sqrt{\mathbf{T}'_B : \mathbf{T}'_B}}{\sqrt{2}\sigma_0} \right)^n \cdot \frac{\mathbf{T}'_B}{\sqrt{tr(\mathbf{T}'^2_B)}} ; \tag{3.8}$$

$$f_R = \frac{\alpha^2}{(\alpha + \sqrt{(tr(\mathbf{F}_B \mathbf{F}_B^T)/3) - 1})^2} \tag{3.9}$$

where $\dot{\gamma}_0$ is a dimensional scaling constant ($\dot{\gamma}_0 = 10^{-4}$ s^{-1}). The reptation factor, f_R, accounts for the increasing resistance to viscous flow observed in macromolecular networks for increasing levels of accumulated viscous deformation. The factor α is a small constant introduced to eliminate the singularity at $\mathbf{F}_B$=1, and is set to α=0.005, as in the previous tissue study [175]. The rate sensitivity exponent, n, and the strength parameter, σ_o, are material properties.

The (deviatoric) backstress $\mathbf{T}_C$ is obtained from the standard linear solid network (CDE) as further detailed in Prevost *et al.* [175]. Briefly, the stress in the elastic elements, (C) and (E), is taken to scale linearly with the deviator of the respective Hencky strains through shear moduli G_o and G_∞. The stretching tensor, $\tilde{\mathbf{D}}_D = \mathbf{F}_C \cdot \dot{\mathbf{F}}_D \cdot \mathbf{F}_B^{-1}$ in the viscous element (D) is taken to scale linearly with the driving stress in element (D) through a viscosity η. Conceptually, element (C) is associated with short-term dissipation mechanisms, while the linear element (E) captures the long-term partial relaxation of the backstress.

A mechanistic interpretation of the material parameters is detailed in Prevost *et al.* [175], and can be briefly summarized as follows:

- K measures the small-strain resistance to volumetric deformation (bulk modulus);
- μ_o and λ_L mediate the instantaneous (elastic) nonlinear response of the cell in shear; more specifically, μ_0 correlates with the low-strain instantaneous shear response and λ_L correlates

with a limiting stretch associated with a marked increase in resistance to deformation;

- G_o, G_∞, and η address the time-dependencies unfolding at medium and long time scales; more specifically, the ratio $\tau_\infty = \eta/G_\infty$ scales with the characteristic long-term relaxation time, while G_o relates to the short term "backstress" stiffness of the material, modulating the recovery of viscous deformation at higher rates of loading; by neglecting the compliance of the non-linear instantaneous elastic response, an equilibrium (long term) shear modulus can be estimated as $G_{eq}=(1/G_o+1/G_\infty)^{-1}$;
- σ_o and n address the time-dependencies unfolding at short time scales; more specifically, σ_o relates to the resistance to viscous deformation in the nonlinear viscous element and n represents the strain-rate sensitivity of the viscous resistance. For n~1, and negligible accumulated viscous deformation, a single short term characteristic time for viscous relaxation can be estimated as: $\tau_o= (\sigma_o/G_o)(\dot{\gamma}_0^{-1})$. For $n\neq1$, the non-linear element captures the effects of superposing stress-activated viscous mechanisms, and a single time constant cannot be meaningfully defined.

Note that the long-term dissipation mechanisms are captured mainly through a single retardation time provided by the standard linear solid element (CDE). Although sufficient to account for the essential features of the cell relaxation behavior (as measured under the selected test conditions of the present study), the current formulation may require some refinements (e.g. the introduction of additional Kelvin-type viscoelastic components) to encompass the broader spectrum of relaxation mechanisms that are likely to unfold under more complex loading conditions. Further details on the constitutive equations, and a review of the main alternative modeling approaches developed within the brain biomechanics community, at the continuum tissue level, are provided in Prevost *et al.* [175].

The constitutive model was implemented as a user-defined material subroutine in the finite element software Abaqus (Simulia, Providence, RI). An axisymmetric representation was selected for the test configuration as shown in Figure 3-8 B, C. The cell body was idealized as a half oblate spheroid while the indenting probe was modeled as a rigid sphere. Frictionless contact was enforced between the two. For studies on glass, the underlying glass substrate was considered rigid, in slipless contact with the cell. For experiments on polyacrylamide gels, a 200 μm thick deformable layer under the cell was included to represent the gel. This accounted for any deformation of the gel included in the measured AFM response. A representative geometry and meshing is shown in Figure 3-8 C. The gel was modeled as an elastic material with Poisson's ratio of 0.48 [123, 174] and Young's Modulus as measured with the AFM and listed in Table 3-2. The physical dimensions of the cells were taken to match the measured estimates – cross-diameter and height – obtained for each cell. The entire loading history (approach – dwell – dynamic load–unload – relaxation) was simulated in Abaqus and the material model parameters for each (homogenized) cell were determined by fitting the experimental responses, where the quality of the fit was estimated based on the error measure:

$$Error = \frac{\sqrt{\left\langle \left(F_{\text{simul}} - F_{\text{exp}} \right)^2 \right\rangle}}{F_{\text{exp}}^{\max}}. \tag{3.9}$$

F_{simul} and F_{exp} refer to the discrete time vectors for the simulated and measured indenter forces respectively, and $F_{\text{exp}}^{\max}$ corresponds to the maximum reaction force as measured experimentally at the highest (10 $\mu m.s^{-1}$) displacement rate.

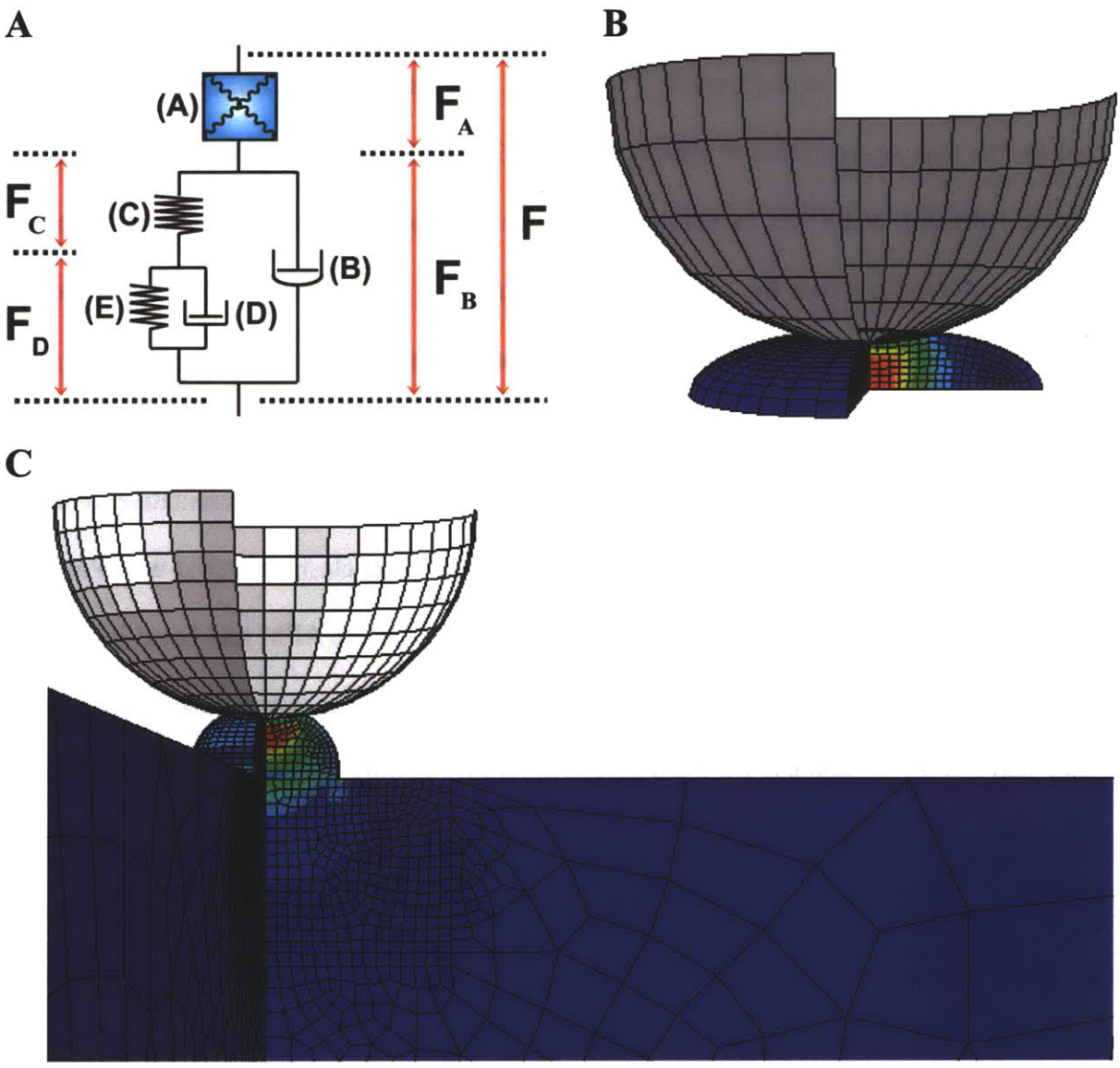

Figure 3-8: (A) Schematic of cell material model, including 8 material parameters. (B) Representative finite element model geometry for an astrocyte tested on glass. (C) Representative geometry and meshing for a neuron grown on gel, with the gel layer included in the model.

Chapter 4

Characterization of Neuron and Astrocyte Response on Glass

4.1 Introduction

In order to understand how neurons and astrocytes respond to mechanical loading transients characteristic of TBI, it is critical to characterize their mechanical response at large deformations and at various loading rates. In addition, single cell models with accurate material parameters are essential for simulating what happens at the cellular level during TBI. In this chapter, results of AFM indentation studies on neuron somata, neuron processes, and astrocytes are presented. In addition, the AFM results are used to calibrate material parameters of the constitutive model described in section 3.3, which was adopted for both neurons and astrocytes. This work highlights key characteristics of the cell response, as well as some interesting differences between the material properties of neurons and astrocytes. This chapter expands on existing

knowledge of CNS cell material properties by characterizing the deformation at large strains and under whole cell compression, yielding calibrated models capable of capturing all aspects of the cell responses at 3 different loading rates and under stress relaxation. These models enable simulations of other types of mechanical loading at the cellular level, and additionally, provide a quantitative comparison of the properties of neurons and astrocytes.

4.2 Neuron Results

Neuron force response was measured using two different AFM experimental set-ups. One method enabled compression of the whole neuron soma with a large microsphere, while the other allowed for the neuron processes to be probed using a pyramidal AFM tip. These two experiments enabled characterization of two important, yet different, areas of the neuron – both susceptible to damage in TBI.

4.2.1 Response of the Neuron Soma[4]

The mechanical response measured for single cortical neurons showed marked nonlinearities in the strain and strain rate domains and substantial hysteresis, as shown for one representative cell (diameter of 14.2 μm, height of 7.6 μm) in Figures 4-1 and 4-2. While these key response features – time/rate dependencies, nonlinearities, hysteresis – were consistently observed across the neuronal cell population (N = 87), some substantial variations were noted in force magnitude from one cell to the other. The average indentation response and standard deviation are reported in Figure 4-3, with the corresponding finite element model fit to the average response. The eight-parameter model captures the main characteristics of the cell behavior at large strains, including

[4] Section 4.2.1 is adapted from [76] Ibid. with permission from Elsevier

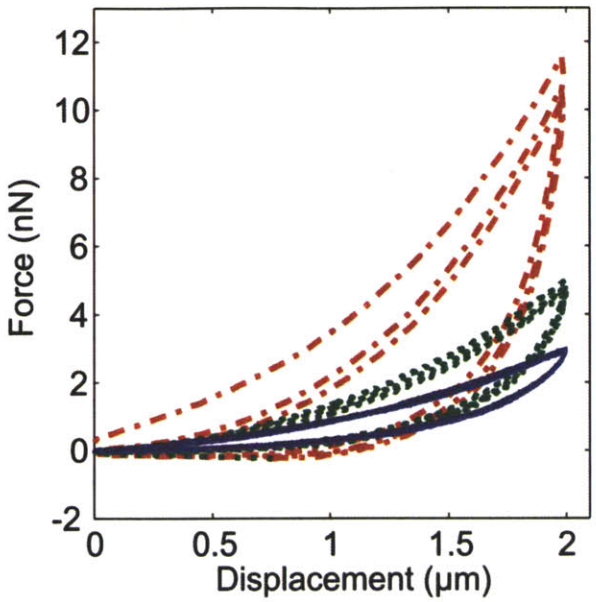

Figure 4-1: AFM data for a representative neuron of diameter 14.2 μm and height 7.6 μm. Force versus displacement response at the 3 consecutive loading rates of 10 μm/s (red dash-dot), 1 μm/s (green dot), and 0.1 μm/s (blue solid).

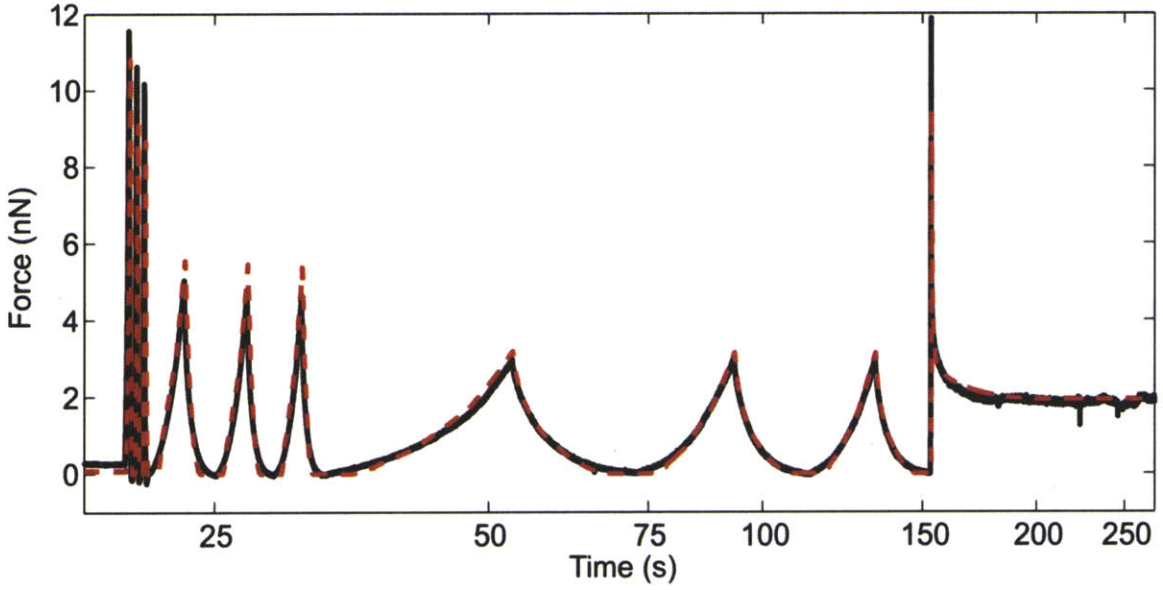

Figure 4-2: Force versus time responses measured for one representative neuron of diameter 14.2 μm and height 7.6 μm (black) and simulated in Abaqus with actual cell geometry (red dash). Material parameters for this cell were found to be: $\mu_o = 13$ Pa, $\lambda_L = 1.06$, $G_o = 85$ Pa, $G_\infty = 80$ Pa, $\eta = 3000$ Pa.s, $\sigma_o = 0.005$ Pa, and $n = 1$. Error measure for the model fit was: 1.09×10^{-4}.

stress-strain non-linearities, rate effects and long-term time dependencies. Values for the fitting parameters are reported in Figure 4-3. Since the AFM data provided a single force–displacement history response, the material bulk and shear contributions to the macroscopic cell response could not be isolated. Following common assumptions of near incompressibility in cell biomechanics, a relatively large value for the bulk modulus, *i.e.* K = 10,000 Pa, was selected, corresponding to a small strain Poisson's ratio of ν=0.499. Note that the set of model parameters associated with the "best" fit is not proven here to be unique, although optimal parameter values are expected to fall within a narrow range. This inference is based on the results of an automated parameter search study conducted in Prevost *et al.* [175], where the same modeling framework was used to fit the qualitatively similar response of brain tissue.

Upon inversion of the deformation rate order, the cell response was measured to exhibit similar rate dependencies (Figure 4-4). These response features were compared to the model predictions (obtained from the same set of best fit parameters in Figure 4-3) and a satisfactory match was found (Figure 4-4).

Given the observed wide range of variations in cell geometry, where both cross-diameter and height measurements showed some significant scatter (D = 16.8 ± 2.1 μm; H = 7.9 ± 2.0 μm; mean ± standard deviation, N = 79), we considered the hypothesis that the deviations in force–indentation response could be mainly ascribed to geometric effects. To investigate the validity of this hypothesis, we performed an approximate geometric normalization for the force indentation responses. A subset of cells (N = 33) for which height and cross-diameter estimates could be reliably obtained was selected to generate normalized plots of the cell response, *i.e.* "nominal stress" versus "nominal strain" diagrams where "nominal stress" and "nominal strain" refer to force and indentation depth normalized by characteristic cross-diameter area and height,

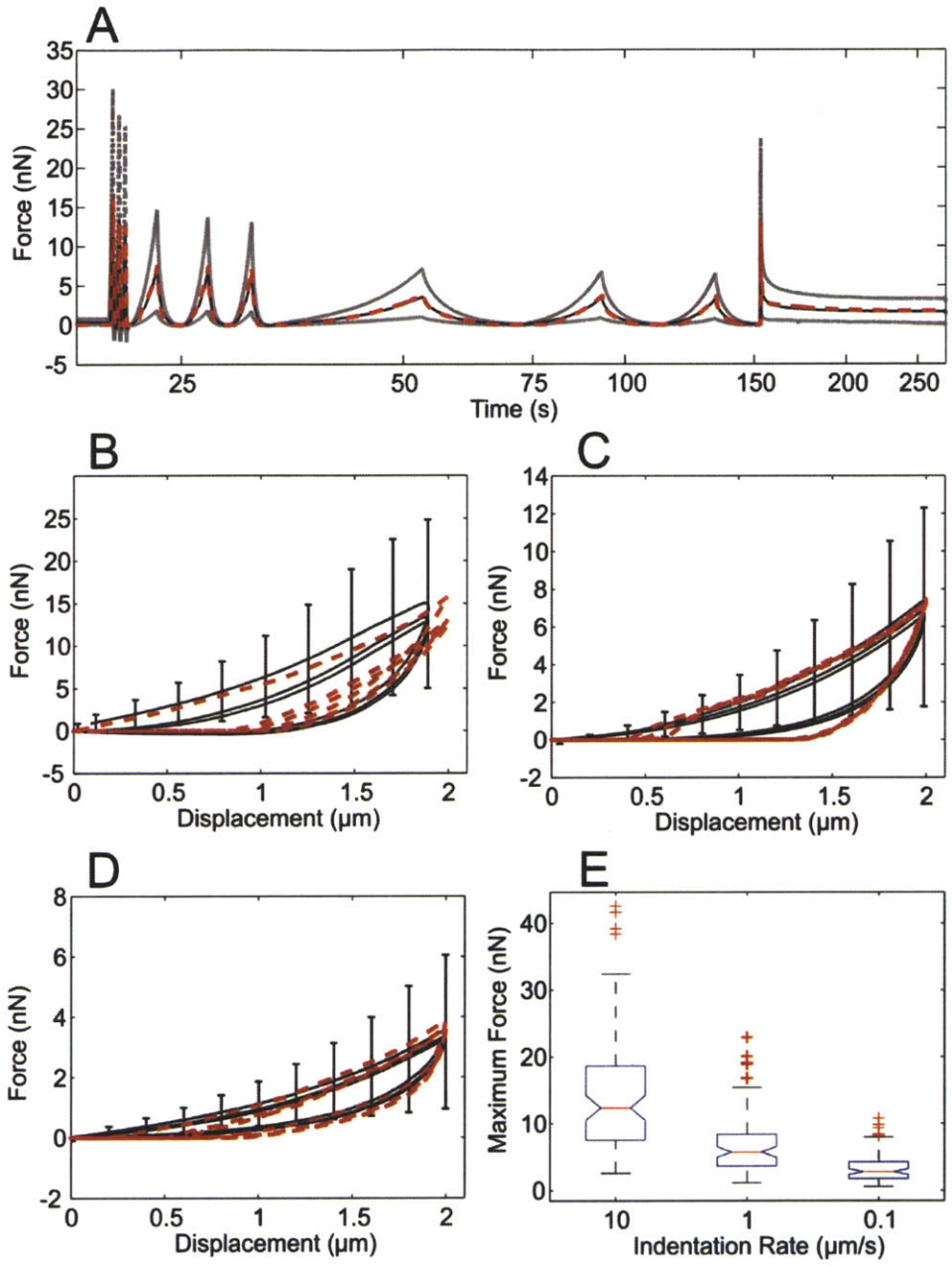

Figure 4-3: (A) Average force versus time response for 87 cells (black line) with plus and minus standard deviations (grey line); model fit (red dashes) to average response. The pictured model fit corresponds to an error measure of 1.1×10^{-4}. (B, C, and D) Average force versus displacement response at 10, 1 and 0.1 μm/s respectively. Error bars represent standard deviations and red dashes correspond to model fit. Material parameters obtained by fitting the force-indentation response to the average experimental response were found to be: $\mu_o = 16$ Pa, $\lambda_L = 1.05$, $G_o = 75$ Pa, $G_\infty = 40$ Pa, $\eta = 3000$ Pa.s, $\sigma_o = 0.005$ Pa, and $n = 1$. K was held constant at 10,000 Pa. (E) Distribution in maximum force level at the end of the first loading ramp for each displacement rate. Outliers are displayed with a red + sign. Rate effects were found to be statistically significant ($P < 0.0001$, one-way ANOVA).

respectively. The normalization procedure did not appear to substantially reduce the scatter in the data, indicating that the observed deviations in force-indentation responses might not simply be an effect of cell geometry variations, but may also reflect a degree of variability in the constitutive material response.

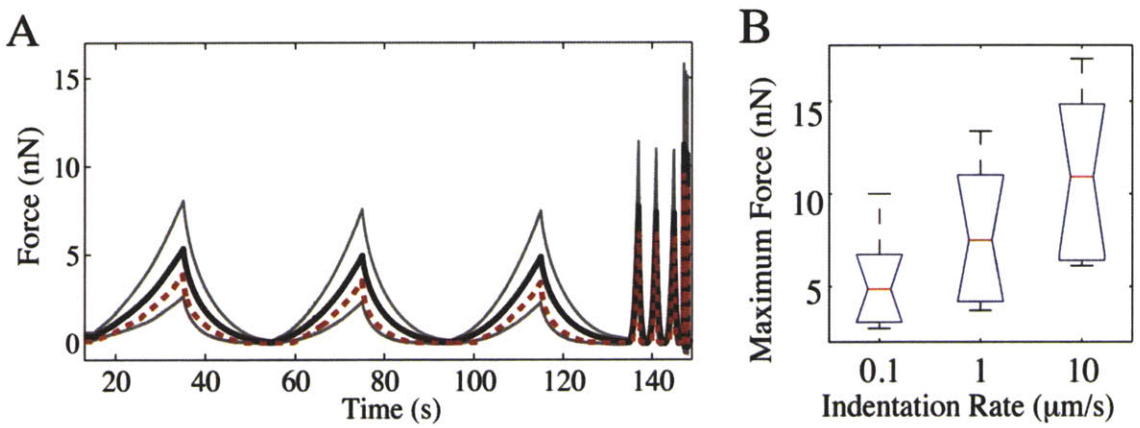

Figure 4-4: (A) Mean (black) and standard deviation (grey) for 10 neurons indented with loading rates in reverse order (0.1, 1, 10 μm/s). Model predictions (red dash) using the mean set of parameters obtained for indenting a neuron in 10, 1, 0.1 μm/s loading rate order; (B) Peak forces reached at the end of the first loading ramp for each displacement rate. Rate effects were found to be significant ($P < 0.006$, one-way ANOVA).

This conclusion is further supported by the data provided in Table 4-1, where the best fit model parameters for the subset of cells of known geometrical features ($N = 33$) are given in terms of their average values and ranges of variation. Here, in order to address possible shortcomings of the approximate normalization procedure, sets of model parameters for each cell were obtained by fitting the individual cell responses with finite element models accounting for the actual cell geometry (height and diameter) as shown for one cell in Figure 4-2. The mean squared errors between the simulated and measured responses, which ranged between 7.4×10^{-5} and 1.37×10^{-4}, were found to be comparable to those obtained between the simulated and average responses reported earlier in Figure 4-3 (1.1×10^{-4}). The scatter in the values of the fitting

parameters demonstrates that, even when accurately accounting for cell geometry effects, the cell constitutive response is found to exhibit substantial variability.

	G_o (Pa)	n	σ_o (Pa)	λ_L	μ_o (Pa)	η (Pa.s)	G_∞ (Pa)
Mean	78.48	0.9927	0.005455	1.051	15.99	2879	52.64
Data Range	30-200	0.92-1	0.004-0.009	1.015-1.17	1-75	400-4000	7-300

Table 4-1: Distribution in parameters (mean and data range) obtained by fitting model response to experimental data for 33 cells, accounting for actual cell configuration by varying the model geometric parameters to match the measured height and cell radius. K was assumed to be constant for all cells and set at 10,000 Pa.

Interestingly, in support of an inference of uniqueness for the optimized values, the average of each model parameter obtained by independently fitting data for 33 cells (Table 4-1), is in good agreement with the corresponding value (Figure 4-3) obtained by fitting the representative cell response. From the representative parameters G_o = 75 Pa, G_∞ = 40 Pa, η = 3000 Pa.s, σ_o = 0.005 Pa, with a value of n=1, it is then possible to estimate short-term and long-term characteristic times for viscous relaxation as: τ_o=0.67 s and τ_∞ = 75 s, with a long-term equilibrium shear modulus, G_{eq}, of the order of 25 Pa.

4.2.2 Response of the Neuron Processes

Results of the indentations on neuronal processes showed processes to be viscoelastic, with differences in force-displacement response observed between 10 and 1 μm/s loading rates (Figure 4-5 A, B). These responses are analyzed in the context of a Hertz model, with pseudo-elastic (rate-dependent) Young's moduli obtained by fitting the force-displacement responses at each testing rate, 10 and 1 μm/s, as shown for a representative process in Figure 4-5 C, D. The pseudo-elastic Young's modulus was found to be dependent on the loading rate as shown in

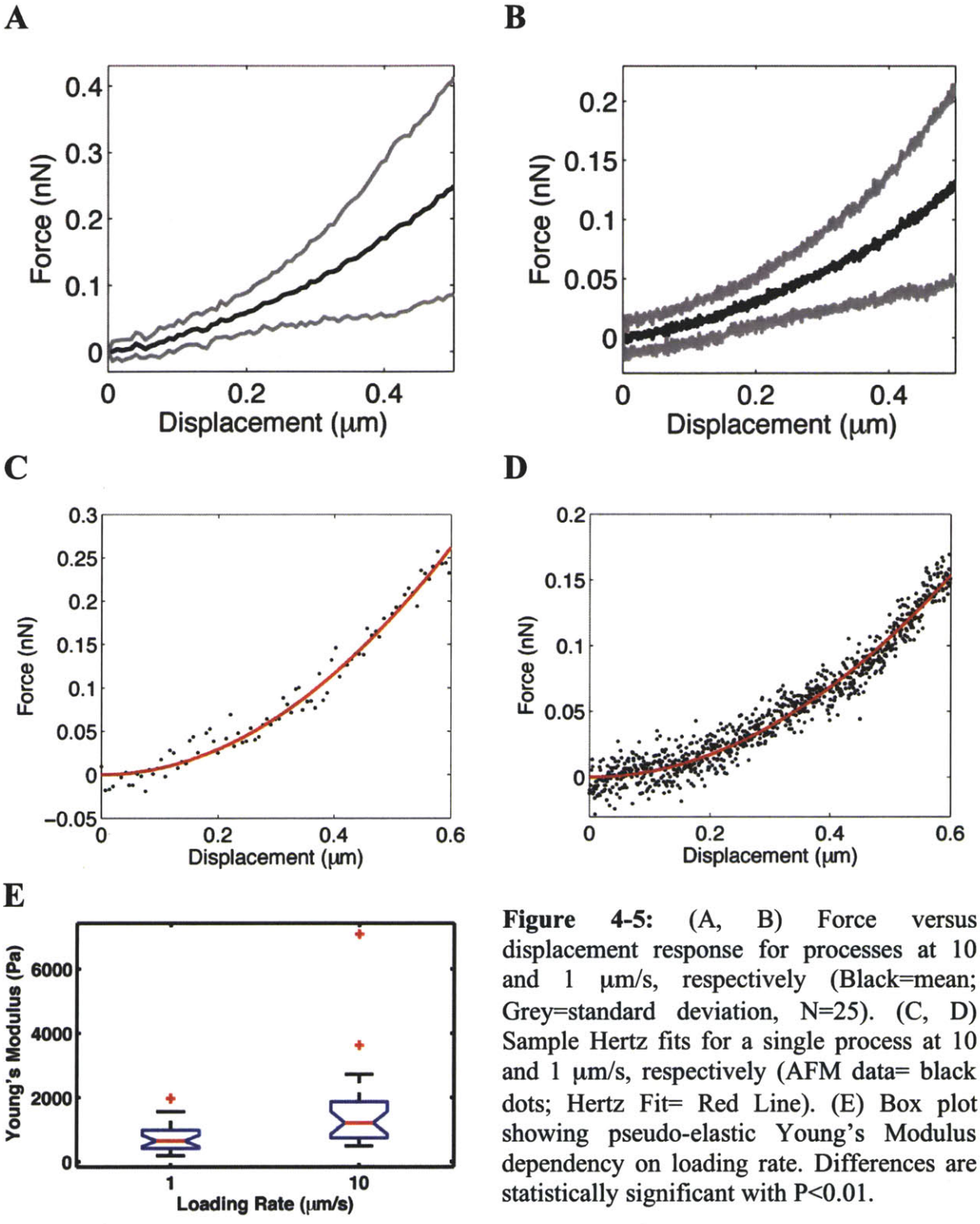

Figure 4-5: (A, B) Force versus displacement response for processes at 10 and 1 μm/s, respectively (Black=mean; Grey=standard deviation, N=25). (C, D) Sample Hertz fits for a single process at 10 and 1 μm/s, respectively (AFM data= black dots; Hertz Fit= Red Line). (E) Box plot showing pseudo-elastic Young's Modulus dependency on loading rate. Differences are statistically significant with $P<0.01$.

Figure 4-5 E. The pseudo-elastic Young's modulus at 10 μm/s was found to be 1618.8 +/- 1378.1 Pa and at 1 μm/s was determined to be 791.94 +/- 508.58 Pa (mean +/- standard deviation; N=25). The difference in modulus was statistically significant with a $P<0.01$. These results show that the mechanical response of the processes is rate dependent, and should be recast in a viscoelastic framework. Further characterization accounting for the response at multiple loading rates with a single set of material properties, as was done for the neuron soma, would provide a more substantial analysis of the viscoelastic characteristics of the neuron processes. Due to limitations in the current system capability to accurately image and measure the dimensions of the processes beneath the indenter tip (especially the thickness), this effort was deemed to be beyond the scope of the present investigation.

In order to compare the measured response for the neuron processes with the results for the neuron soma, a pseudo-elastic model was also considered for the soma at both the 10 and 1 μm/s loading rates. This was done by changing the material model in the Abaqus simulations to be that of the built in elastic model characterized with a Young's modulus, E, and a Poisson's ratio, ν. Due to the viscoelastic nature of neuron soma, and for comparison with the models used to fit the neuron process results, only the data for the first loading ramp at each rate were used for fitting and different Young's Moduli were obtained for each loading rate as shown in Figure 4-6.

While these results yield a lower Young's Modulus for the neuron soma than for the processes (725 Pa at 10 μm/s and 350 Pa at 1 μm/s for the soma and 1618.8 Pa at 10 μm/s and 791.9 Pa at 1 μm/s for the processes) we note that the same indentation rate results in different strain rates for the soma and the processes due to the significantly lower thickness of the processes. This suggests that it may be more reasonable to compare the results of the processes at 1 μm/s with the results of the soma at 10 μm/s. In addition, the different geometries of the AFM

tips used for testing the different regions of the neurons could potentially cause discrepancies in the measured response. The sharp tip used to test the processes enables probing of more local properties, when compared to the more global properties measured with the large spherical probe. Based on these results, the neuron processes and soma appear to have properties of a similar magnitude and it is arguable that a similar material model could be used to represent all regions of the neuron.

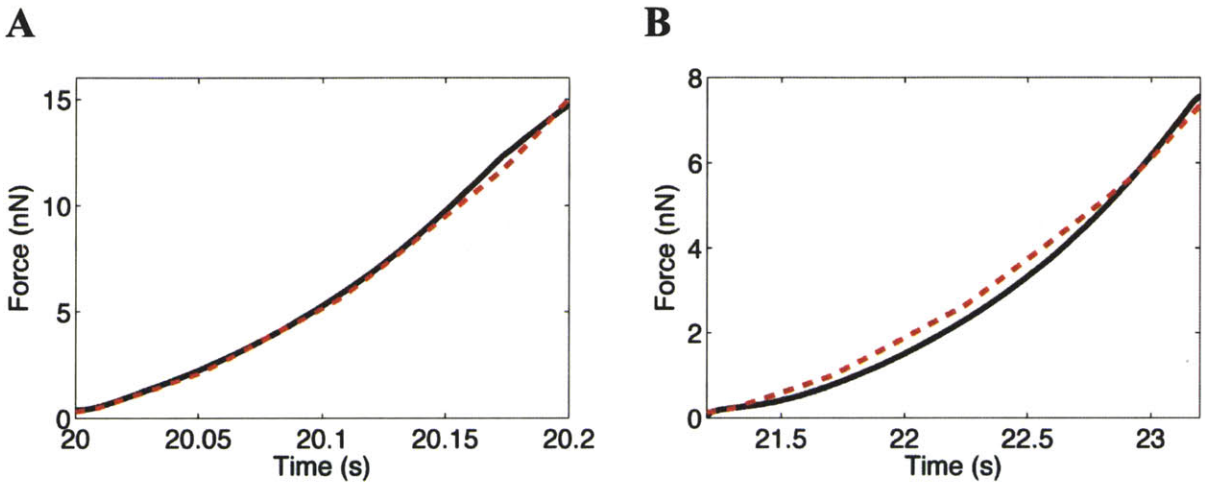

Figure 4-6: AFM data (black) and elastic model fit (red dashes) for neuron soma indented at 10 μm/s (A) and 1 μm/s (B). Young's Modulus values used for fitting were 725 Pa at 10 μm/s and 350 Pa at 1 μm/s with the cells assumed to be incompressible with a Poisson's ratio of 0.5.

4.3 Astrocyte Results

The dynamic astrocyte responses shared similar qualitative trends with those observed for neurons, showing non-linearities, hysteresis, and time and rate dependencies. However, there were notable quantitative differences in the measured response between neurons and astrocytes. The characteristics of the astrocyte response are shown for a single representative astrocyte of radius 18 μm and height 5 μm in Figure 4-7. While these qualitative trends held across all cells tested, like neurons, astrocytes showed considerable variation in force response as shown by the

standard deviation in Figure 4-8. Astrocytes also had considerable geometry variation with a mean measured height of 5.34 +/- 1.28 μm and a radius of 15.53 +/- 3.97 μm (mean +/- standard deviation).

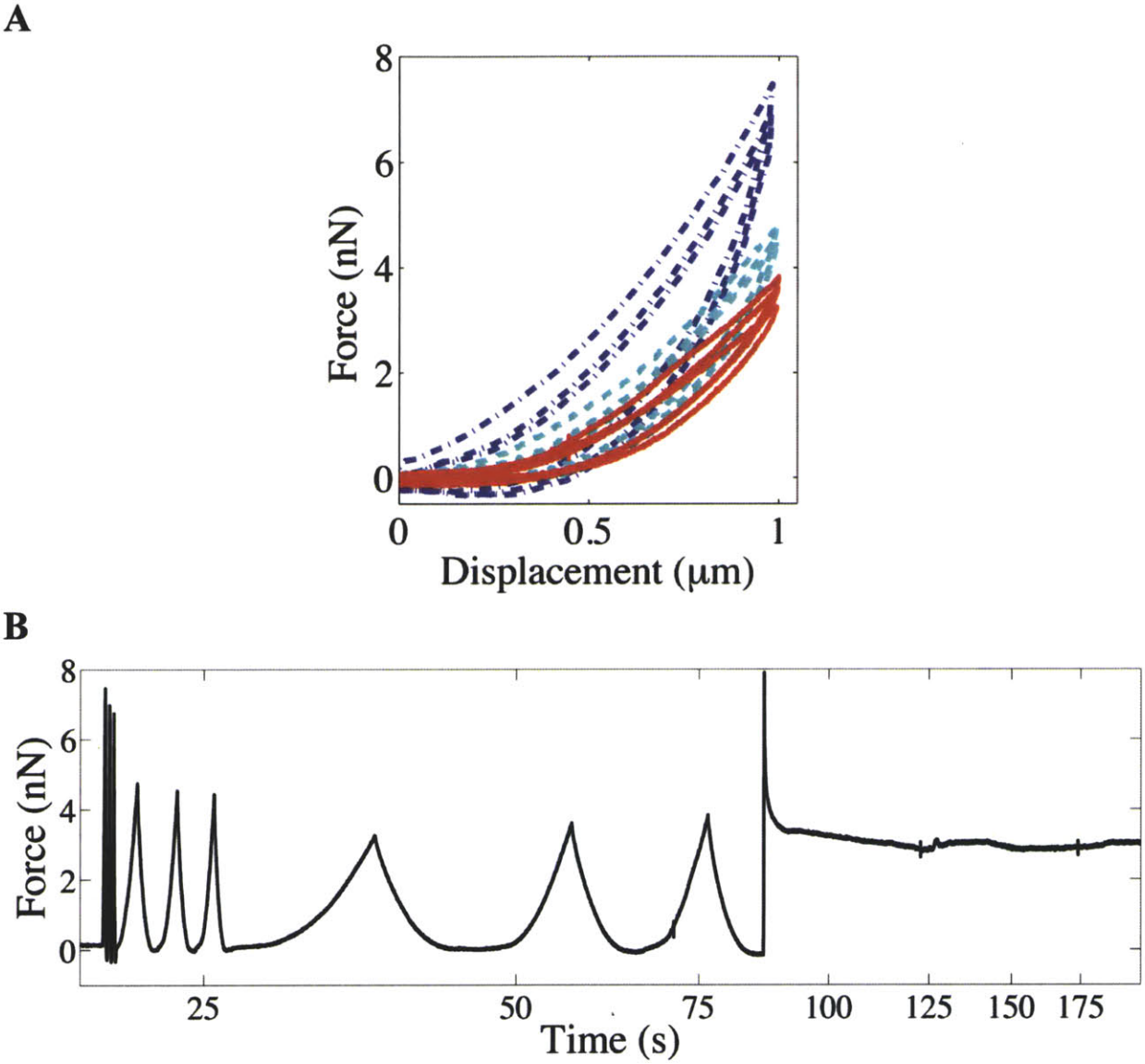

Figure 4-7: AFM data for a representative astrocyte of diameter 36 μm and height 5 μm. (A) Force versus displacement response at the 3 consecutive loading rates of 10 μm/s (blue dash-dot), 1 μm/s (cyan dash), and 0.1 μm/s (red solid). (B) Force versus time response.

The same constitutive model used to characterize the neuron response also accurately captured the response measured for astrocytes when calibrated with the set of material parameters listed in Figure 4-8. Both the AFM results and the resulting model parameters suggest that astrocytes are more elastic than neurons, exhibiting less rate effects as well as increased elastic parameters and decreased viscous contributions. Astrocyte responses were found to be less rate-dependent than neuron responses where the AFM force for the low-rate cycles is more significantly reduced for the neuron population, and the equilibrium response in relaxation is much lower than the peak force. This is reflected by differences between the optimized material parameter values shown in Figure 4-3 and Figure 4-8, where the ratios of viscoelastic to instantaneous moduli (G_o/μ_o and G_∞/μ_o) were found to be significantly higher for astrocytes. To our knowledge, this is the first time this trend has been reported in quantifiable terms.

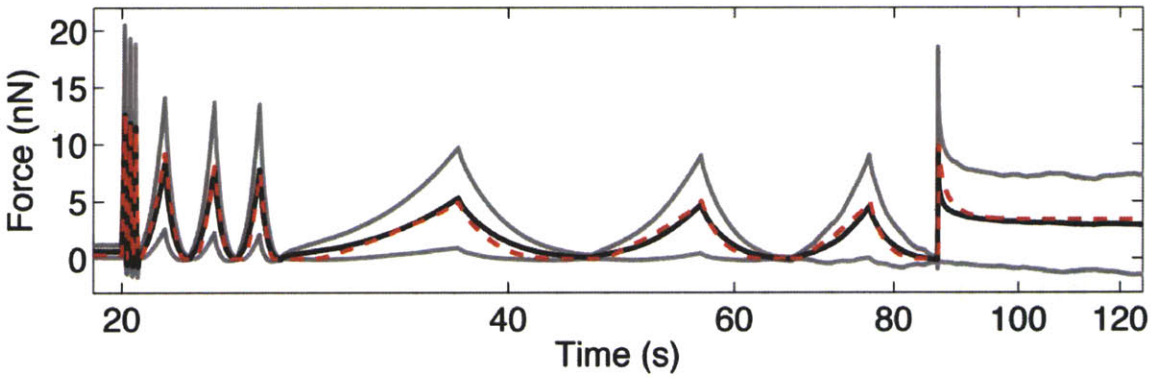

Figure 4-8: Average force versus time response for 37 astrocytes (black line) with plus and minus standard deviations (grey line); and model fit (red dashes) to average response. Material parameters obtained by fitting the force-indentation response to the average experimental response were found to be: μ_o = 13 Pa, λ_L = 1.08, G_o = 275 Pa, G_∞ = 80 Pa, η = 300 Pa.s, σ_o = 0.005 Pa, and n = 0.80. K was held constant at 10,000 Pa.

4.4 Discussion[5]

This study uncovers novel features pertaining to the large strain dynamic response of single primary neurons and astrocytes of the neonatal rat cortex and presents a general framework for a constitutive model in quantitative support of these observations. It is, to our knowledge, the first reported body of experimental measurements on the nonlinear, hysteretic, viscous behavior of single neurons (both somata and processes) and astrocytes at finite deformation. The cell response was characterized over three orders of deformation rate magnitude (10, 1 and 0.1 $\mu m.s^{-1}$) to either 1 μm (astrocytes) or 2 μm (neuron soma) indentation depth (corresponding to a pseudo-compression nominal strain of 15 to 40 %) in load, unload and relaxation according to decreasing and increasing orders of deformation rates (10, 1 and 0.1 $\mu m.s^{-1}$ for N = 87 neurons; 0.1, 1 and 10 $\mu m.s^{-1}$ for N = 10 neurons; 10, 1 and 0.1 $\mu m.s^{-1}$ for N = 37 astrocytes). In addition, the response of the neuron processes was measured at 10 and 1 $\mu m.s^{-1}$ for N=25 processes. Although quantified with a simplistic model, when compared to neuron soma modeled in a similar manner, results suggest the response of the soma and processes to be of the same order of magnitude and that a similar model can arguably account for the response of all regions of the neurons. The cell response for both neurons and astrocytes was found to exhibit substantial hysteresis, significant strain and strain-rate dependent nonlinearities, and marked long-term time dependencies. Given the characteristic length scale at which cell properties were probed, it is difficult to tease out information about the sub-cellular, structural basis of the various response features. However, it may be speculated that intermediate filaments and actin filaments are the main contributors to the nonlinear strain dependencies observed at the soma level, as substantiated by previous mechanical investigations on these cytoskeletal components [142, 181,

[5] Section 4.4 is adapted from [76] Ibid. with permission from Elsevier

182]. Key observations in the response at the single cell level (nonlinearities, hysteresis and time-dependencies) mirror those reported by several investigators at the cortical tissue level [175, 183, 184] and might pave the way for a unified understanding of the mechanical dynamics unfolding from the tissue level down to the cell level in response to mechanical insults. The corollary observation that the rate effects remain significant upon reversal of the deformation rate order in neurons suggests that the dynamic response features measured reflect intrinsic mechanical properties of the cell rather than manifestations of active cellular processes such as cytoskeletal rearrangement (although the involvement of the latter processes cannot be excluded). The present testing protocols may also be adapted/refined to characterize the dynamic properties of other neural and glial cell types and/or sub-cellular regions, thereby providing potentially unique insights into mechanically mediated biological responses of single neural cells under complex regimes of deformation. Among the limitations of the current experimental study, we note that the volumetric compliance of the cell and its response in other modes of deformation (tensile, shear) were not investigated. Further, the current experimental method relied on cells plated *in vitro* on two-dimensional, hard substrates. We cannot exclude the possibility that the properties hereby collected differ from those actually encountered in a full three-dimensional environment *in vivo*. This limitation is addressed in more depth in Chapter 5. In addition, some significant variations in the mechanical data collected (*e.g.* peak forces and cell compliances at large strains) were observed within the neuron and astrocyte populations considered. These differences may be attributed to numerous factors including: potential inaccuracies in the cell–cantilever contact point determination, disparities in cell body geometrical features, variations in cell/substrate contact surface area and adhesion conditions, intrinsic biological differences (cell types, development stages) in the cell population considered,

and variation in initial point of contact relative to the nucleus (which has been shown to be stiffer than its cytoplasmic counterparts [185, 186]). These sources of variation may make for interesting avenues of investigation to be explored in future studies. In particular, addressing the question of whether substantial differences in neuron properties exist across brain regions might help unravel the cascade of damage mechanisms suspected to unfold within the brain following the imposition of external mechanical transients.

The constitutive model proposed for the homogenized cell response, following previous continuum developments undertaken at the tissue level [175], was able to capture all major complexities of the cell response, for both neuron somata and astrocytes, in load, unload, reload and relaxation, via a relatively low number of material parameters. Although phenomenological, the model yielded quantitative assessments of different aspects of the cell response to deformation – *e.g.* elastic resilience at low to large strains, rate sensitivities in the quasi-static to dynamic regimes. The instantaneous elastic response was found to be well captured by a nonlinear hyperelastic formulation based on a freely-jointed chain model, while viscous relaxation was found to be associated with multiple mechanisms, with at least two characteristic times ($\sim$ 1 s and 100 s for neurons) necessary to account for the observed response within the probed range of deformation rates. As refined indicators of cell dynamics, the complete set of model parameters may also elicit subtler discriminations between cell types (as described here for cortical neurons and astrocytes) within and across brain regions, and allow for the establishment of susceptibility-to-damage maps at the mesoscopic level. The differences in material properties for neurons and astrocytes provide support that methods developed in this chapter can detect differences between populations of cells in the brain and may provide insight into how different cell types respond to mechanical trauma. These latter considerations may be

of particular significance as the potential existence of differential patterns in cell propensity for damage has been substantiated in recent years by observations of consistent mechanical heterogeneities within brain subregions [187]. The current constitutive formulation remains, however, reductive in its simplistic view of the cell as a single, isotropic continuum. The proposed modeling effort must therefore be considered as a preliminary set of constitutive framework developments – potentially enabling the establishment of local stress–strain maps at the cell level – on which structurally based multi-scale model refinements may be built.

4.5 Summary

The work presented in this chapter provides the first substantial quantitative set of mechanical measurements conducted at large strains on single neurons and astrocytes. The constitutive model proposed in support of these observations represents a critical first step towards the development of multi-scale models that may be used to study and simulate the effects of macroscopic mechanical transients on the local cell environment. In addition, it highlights a key difference between neuron and astrocyte response, namely, the fact that astrocytes were found to be more elastic than neurons, as characterized by the 8 material parameters.

Chapter 5

Effect of Substrate Stiffness on Neuron and Astrocyte Response

5.1 Introduction

Building on work from Chapter 4, in this chapter the hypothesis that the material properties of the substrate can influence the mechanical response of neurons and astrocytes is tested. While changes in morphology, cytoskeletal content, and adhesion have all been investigated for neurons and astrocytes grown on substrates of varying stiffness (as described in depth in Section 2.2), to our knowledge, no one has investigated how the material properties of neurons and astrocytes change in response to changes in their substrate stiffness. Changes in cytoskeletal content often correspond to changes in cell material properties. In addition, experiments on fibroblasts, which show similar morphological changes to those of astrocytes when grown on different substrates [124], show that fibroblasts alter their stiffness to match that of their

substrate, with levels of F-actin increasing with gel stiffness [188]. This suggests there could be a significant effect of substrate stiffness on measured astrocyte stiffness. By growing neurons and astrocytes on polyacrylamide gels of different stiffness, substrate dependent changes in AFM force response were measured. To our knowledge, these results represent the first quantitative analysis of how material properties of neurons and astrocytes change depending on the stiffness of their substrate.

5.2 Results

AFM characterization of the gel substrates showed the properties of the gels to be consistent across different regions of a single gel and across different sample preparations as shown by the mean and standard deviations in Table 3-2. The Hertz model for a spherical indenter accurately fit the data for all of the gels, with a sample fit for data from Gel 1 shown in Figure 5-1 A. In addition, testing with the same loading protocol used on cells (*i.e.* at 10 μm/s, 1 μm/s, and 0.1 μm/s and in relaxation), supported our choice to model the gels as elastic materials, defined by a Poisson's ratio and Young's modulus. As shown for a sample Gel 3 in Figure 5-1 B, very limited rate effects were observed over the span of the loading rates used in the cell experiments with the force reaching almost the same peak level at all 3 loading rates. In addition, limited relaxation occurred in the stress relaxation segment.

Results for experiments controlling for the effects of labeling the cells for confocal imaging, in which neurons and astrocytes grown on glass were tested both with and without the addition of dye, show that the dye did not noticeably alter the measured force response of either neurons or astrocytes. As shown in Figure 5-2, both the mean and standard deviation of the response for astrocytes (Figure 5-2 A) and neurons (Figure 5-2 B) remain very similar with the

addition of dye, and any observed differences are well within the observed scatter in the experiment for the given sample sizes. This verifies that the properties measured with dye under the described experimental conditions are what would be expected for unlabeled cells and supports the use of the described methodology.

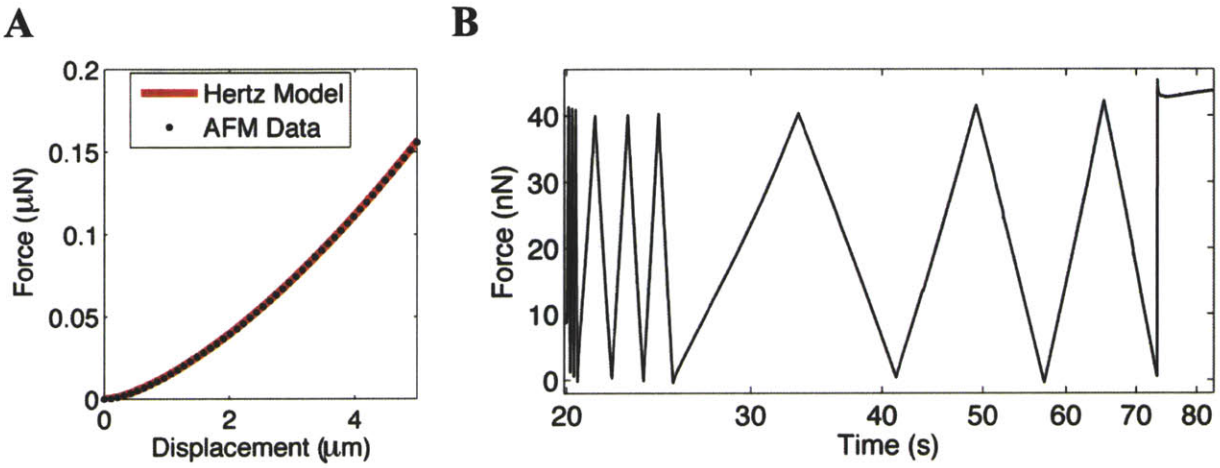

Figure 5-1: (A) Sample Hertz fit for a representative Gel 1 (AFM data- black dots; Hertz model fit- red solid). (B) Representative Gel 3 tested using cell loading routine at 10, 1, and 0.1 μm/s and in relaxation (to a depth of 0.8 μm).

Force response for astrocytes and neurons showed some key differences. As described in Chapter 4 for studies on glass, the response of astrocytes grown on gels showed less rate effects than neurons, suggesting astrocytes to be more elastic than neurons. In addition, astrocytes were considerably more sensitive to substrate stiffness than neurons. Astrocyte AFM indentation data reached significantly lower forces for cells grown on Gels 1, 2, and 3, while the response of astrocytes grown on Gel 4 was more similar to that of astrocytes grown on glass (Figure 5-3 A). In contrast, the change in force response for neurons was considerably smaller, with no drastic changes in force levels observed (Figure 5-3 B). To quantify the significance of the observed dependence of force response on substrate stiffness, a one way Anova followed by multiple comparison test was run to compare the maximum force reached in the first 10 μm/s loading

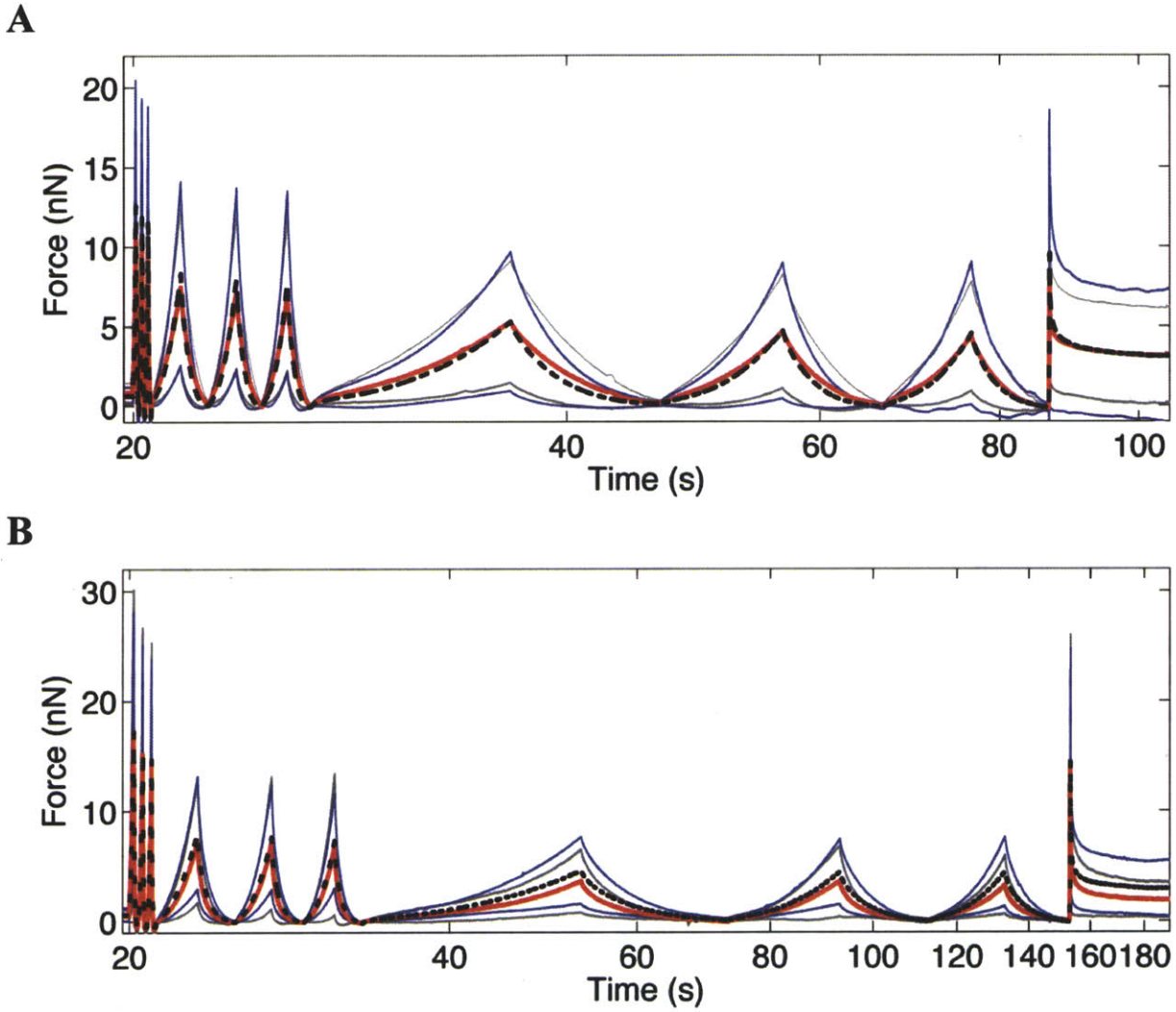

Figure 5-2: Dye versus no dye AFM force vs. time data for astrocytes (A) and neurons (B). Mean response for cells with no dye is shown in red with +/- standard deviation in grey (Astrocytes N=9; Neurons N=9). Mean response for cells with dye is shown in black dashes with +/- standard deviation in blue (Astrocytes N=37; Neurons N=15).

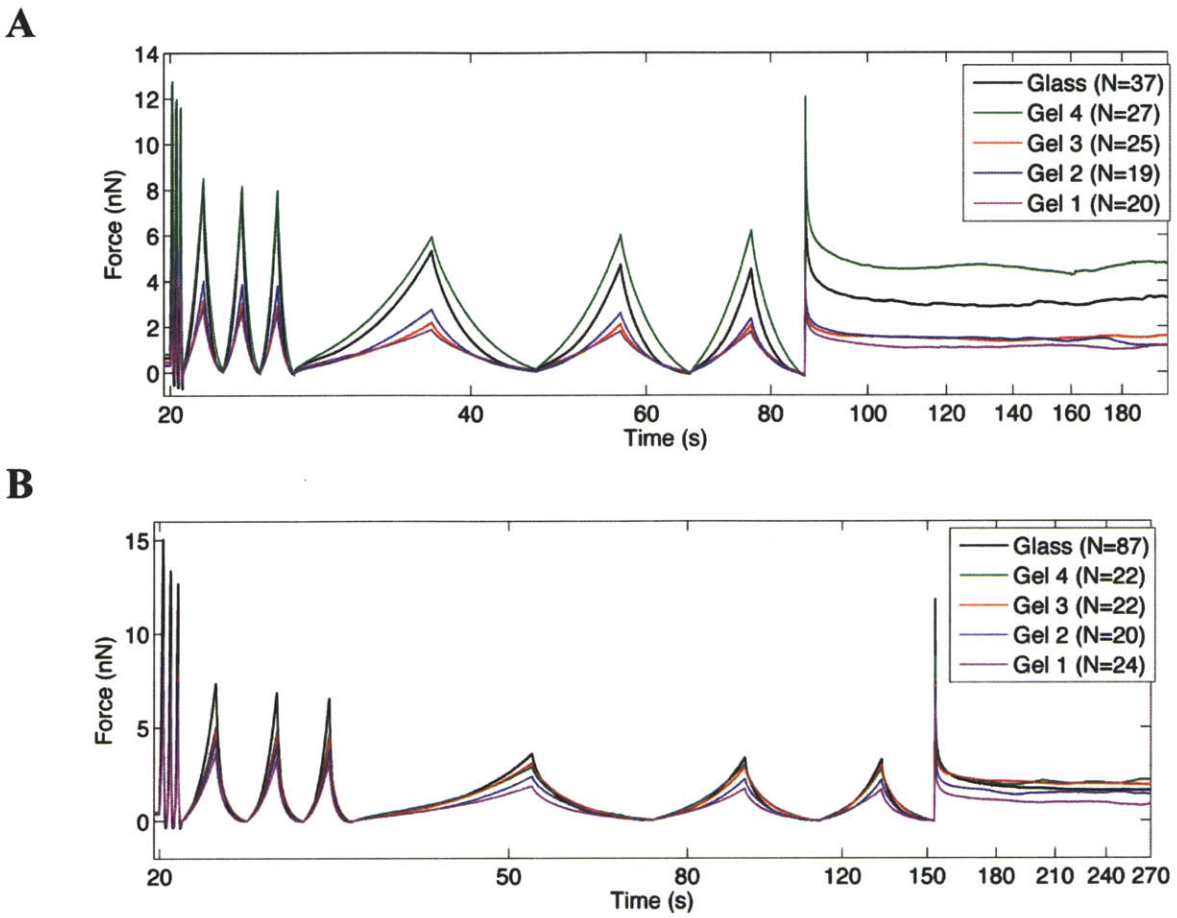

Figure 5-3: Force versus time response for astrocytes (A) and neurons (B) grown on gels of 4 different stiffnesses and glass (glass > Gel 4 > Gel 3 > Gel 2 > Gel 1) show astrocyte response to be more dependent on changing substrate stiffness with two groups emerging (Glass and Gel 4) and (Gel 1, Gel 2, and Gel 3).

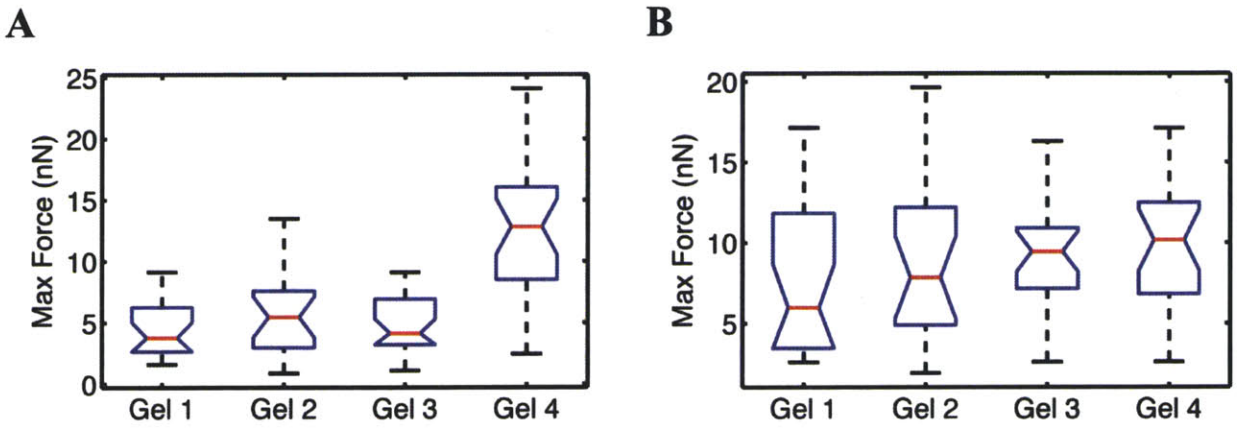

Figure 5-4: Maximum force reached for first 10 μm/s loading ramp for astrocytes (A) and neurons (B) Astrocytes grown on Gel 4 were statistically different from Gels 1, 2, and 3 ($P<0.001$) while no statistical significance was shown for neurons grown on different gels

ramp for cells grown on the different substrates. This showed astrocytes grown on Gel 4 to reach a significantly higher force than those grown on Gels 1, 2, and 3 with $P < 0.001$ (Figure 5-4 A). There were no statistical differences between maximum force reached between Gels 1, 2, and 3. For the maximum force in the neuron response, no statistically significant differences were found between cells grown on any of the gels (Figure 5-4 B). In addition, as described previously by others [122-124], confocal imaging showed the astrocytes changed morphology on different substrates, taking on a larger, more spread shape on stiffer substrates and a smaller, more rounded morphology on soft gels. This morphology change is shown in representative confocal images in Figure 5-6 A, B, C, D, E as well as in the cell dimensions in Figure 5-5 B and Table 5-1 in which average radius is shown to increase with increasing gel stiffness. Mean height and radius values as well as the scatter in the measurements are similar for astrocytes on Gels 1, 2, and 3 as shown in Figure 5-5 B. However, astrocytes grown on Gel 4 have an additional population of cells that have much greater radii values, growing even more spread than the astrocytes grown on glass. This suggests that despite using the same concentration of cell adhesion molecule (poly-D-lysine) on all substrates, the properties of Gel 4 favor more astrocyte spreading than the properties of glass. This suggests a substrate of intermediate stiffness for maximal astrocyte spreading. In contrast, neuron morphology remained similar on all substrates as shown by confocal images in Figure 5-6 F, G, H, I, J and height and radius values shown in Figure 5-5 A and Table 5-1.

Although, astrocytes grown on stiff substrates were mostly spread and those grown on softer substrates were predominately rounded, some rounded astrocytes were observed on stiff gels and some spread astrocytes were found on soft gels (as shown by the scatter in Figure 5-5 B). To determine if rounded astrocytes grown on Gel 4 have a similar mechanical response to

those grown on softer substrates, astrocytes from Gel 4 were divided in to two groups based on the ratio of their height to radius. Astrocytes with a ratio greater than 0.7 were considered to have a more rounded morphology (Figure 5-7 D), whereas those with a ratio less than 0.7 were classified as being more spread (Figure 5-7 C). Results from this classification show that astrocytes grown on Gel 4 with a more rounded phenotype have a lower AFM force response than those classified as spread (Figure 5-7 A, B). The maximum force reached during the first 10 μm/s loading were statistically different with a $P < 0.001$ (Figure 5-7 E). In addition, the response for the rounded astrocytes on Gel 4 is very similar to that observed for astrocytes grown on Gels 1, 2, and 3.

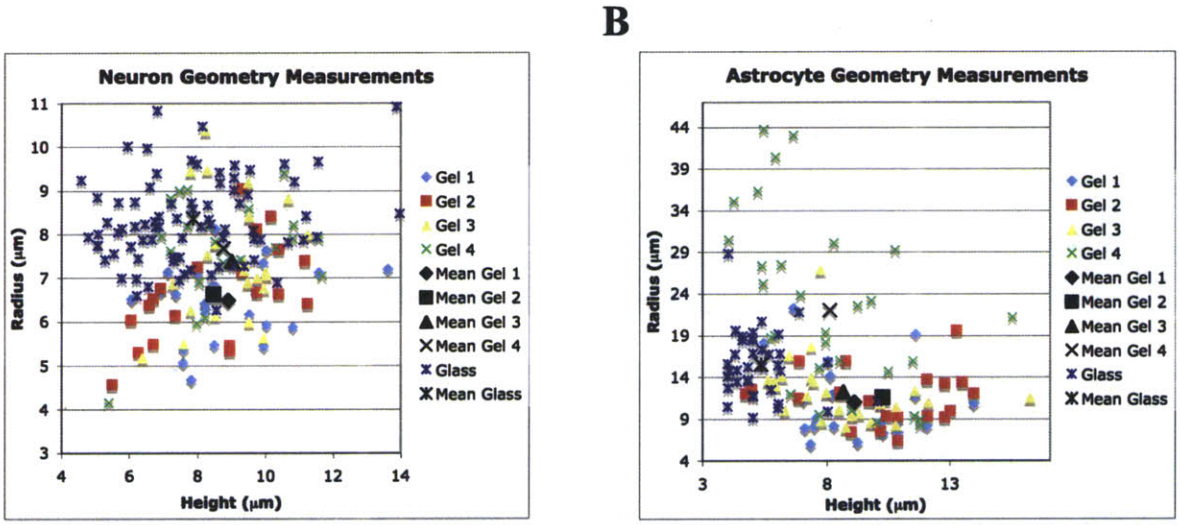

Figure 5-5: Scatter in height and radius measurements for neurons (A) and Astrocytes (B) grown on different substrates; values obtained from confocal images.

	Neurons					Astrocytes				
Cell Dimensions	**Gel 1**	**Gel 2**	**Gel 3**	**Gel 4**	**Glass [76]**	**Gel 1**	**Gel 2**	**Gel 3**	**Gel 4**	**Glass**
Height (μm)	8.89 +/- 1.66	8.47 +/- 1.82	8.99 +/- 1.17	8.76 +/- 1.63	7.9 +/- 2.0	9.10 +/- 2.21	10.26 +/- 2.80	8.65 +/- 2.44	8.107 +/- 2.71	5.34 +/- 1.28
Average Radius (μm)	6.50 +/- 0.86	6.64 +/- 1.14	7.39 +/- 1.38	7.67 +/- 1.17	8.4 +/- 1.05	11.05 +/- 4.64	11.60 +/- 3.25	12.32 +/- 3.92	22.07 +/- 10.52	15.53 +/- 3.97

Table 5-1: Dimensions of neurons and astrocytes grown on substrates of varying stiffness (mean +/- standard deviation) obtained from confocal images.

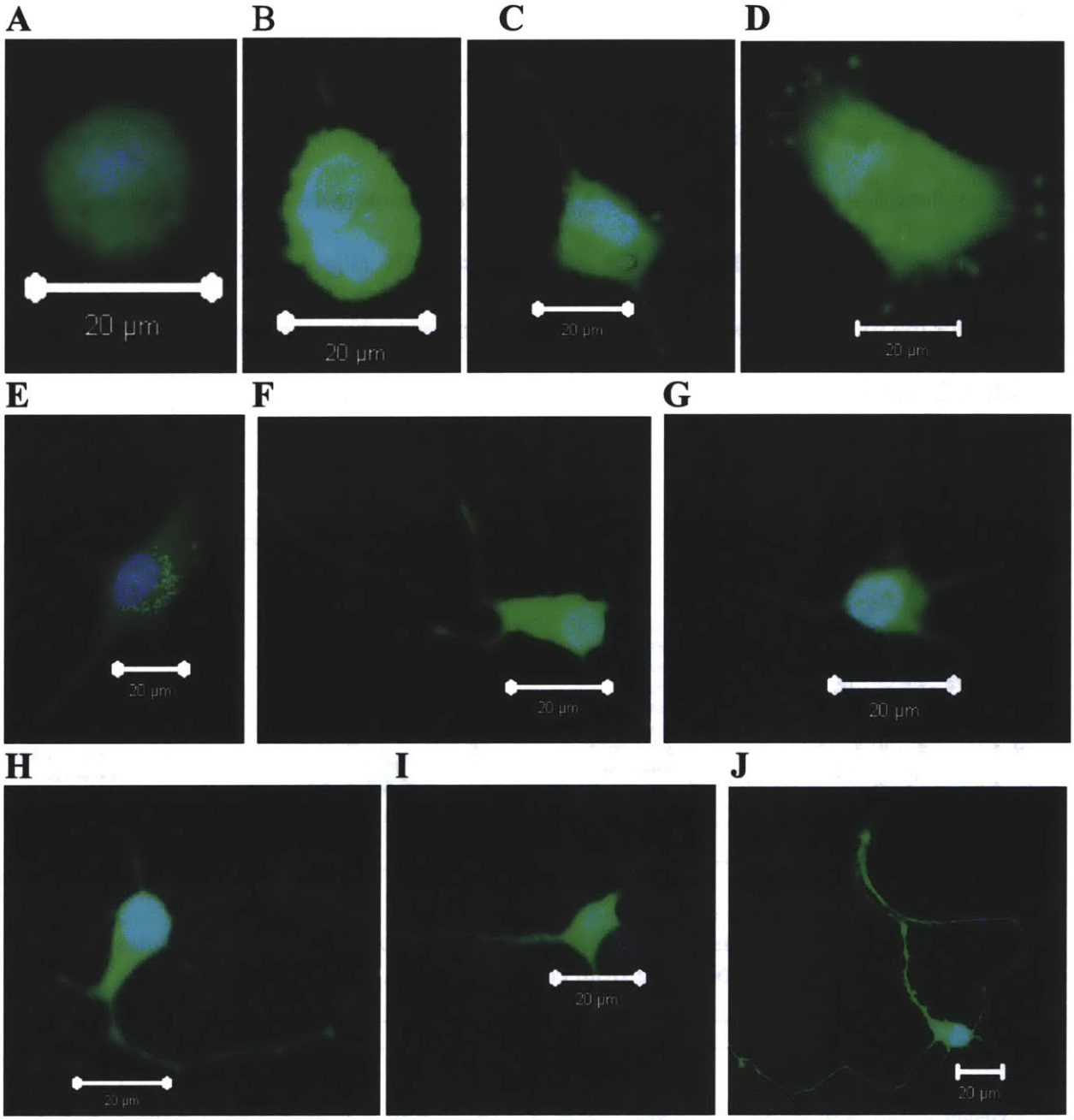

Figure 5-6: Sample morphology of astrocytes grown on (A) Gel 1, (B) Gel 2, (C) Gel 3, (D) Gel 4, and (E) Glass, and neurons grown on (F) Gel 1, (G) Gel 2, (H) Gel 3, (I) Gel 4, and (J) Glass; all scale bars 20 µm.

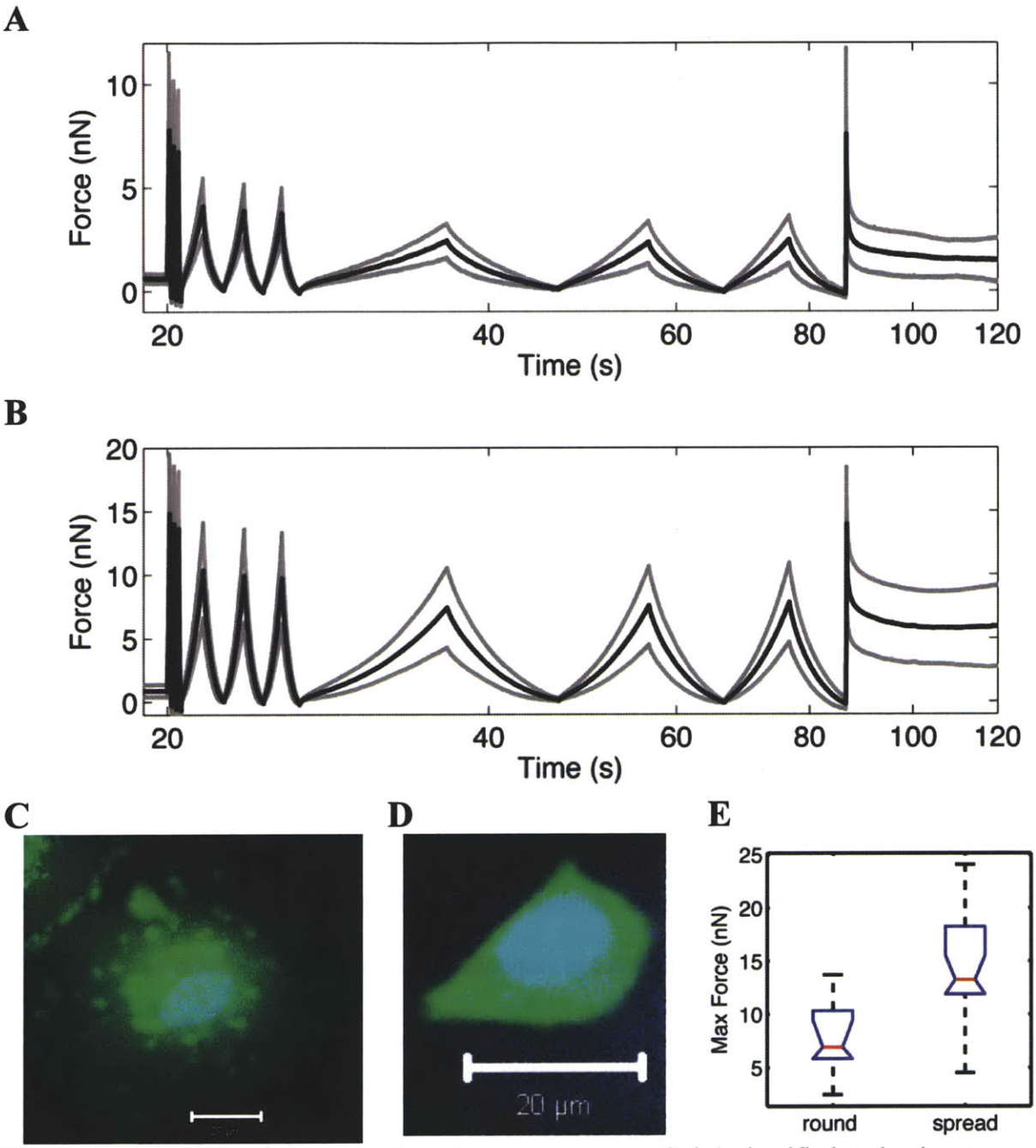

Figure 5-7: AFM force response for astrocyes grown on Gel 4 classified as having a rounded (A) or spread (B) morphology based on height/radius ratio. (Mean=black line; standard deviation= grey line; rounded N=8; spread N=19). Sample astrocytes classified as spread (C) and round (D). (E) Box plot showing the maximum force reached during the first 10 μm/s loading. Force for round and spread are statistically significant with $P < 0.001$.

Results of simulations including both the cell and gel substrate showed that the previously described constitutive model [76] can also accurately capture the response of cells

grown on soft substrates. Due to the similarities between the neuron data for cells grown on different substrates, the parameters obtained in Chapter 4 for neurons grown on glass were initially used in the simulations of neurons on gels. This showed that with no parameter changes the model provided a sufficient approximation of the neuron data (Figure 5-8). For neurons grown on all gels, the model response obtained with the glass parameters falls close to within one standard deviation of the mean. Considering the spread in the data and the small sample sizes, these fits help support the conclusion that neuron properties do not change considerably with their substrate. Next, the mean AFM data for neurons grown on each gel was used to recalibrate the model and yield parameters representing neurons grown on each gel. The resulting optimized fits and parameters are shown in Figure 5-9 and Table 5-2. The resulting spread in parameter values is well within the range obtained for individual neurons grown on glass (Table 4-1). In order to attempt to find an average set of parameters that could represent neurons on all substrates, the parameters obtained for neurons grown on all 5 substrates were averaged and used to simulate the neuron response on each of the gels as shown in Figure 5-10. This set of parameters provides higher quality fits than the parameters obtained for neurons grown on glass and is able to approximate the response for neurons on all substrates.

	Neurons					
Parameters	**Gel 1**	**Gel 2**	**Gel 3**	**Gel 4**	**Glass [76]**	**Mean**
G_0 (Pa)	55	75	85	85	75	75
n	1	1	1	1	1	1
σ_0 (Pa)	0.007	0.005	0.005	0.005	0.005	0.0054
λ_L	1.05	1.06	1.069	1.07	1.05	1.06
μ_0 (Pa)	13	13	14.1	11	16	13.4
η (Pa.s)	5000	3000	2050	1700	3000	2950
G_∞ (Pa)	30	50	75	80	40	55

Table 5-2: Model parameters obtained by calibrating simulated response to mean AFM force data for neurons grown on different substrates. K was held constant at 10,000 Pa for all simulations.

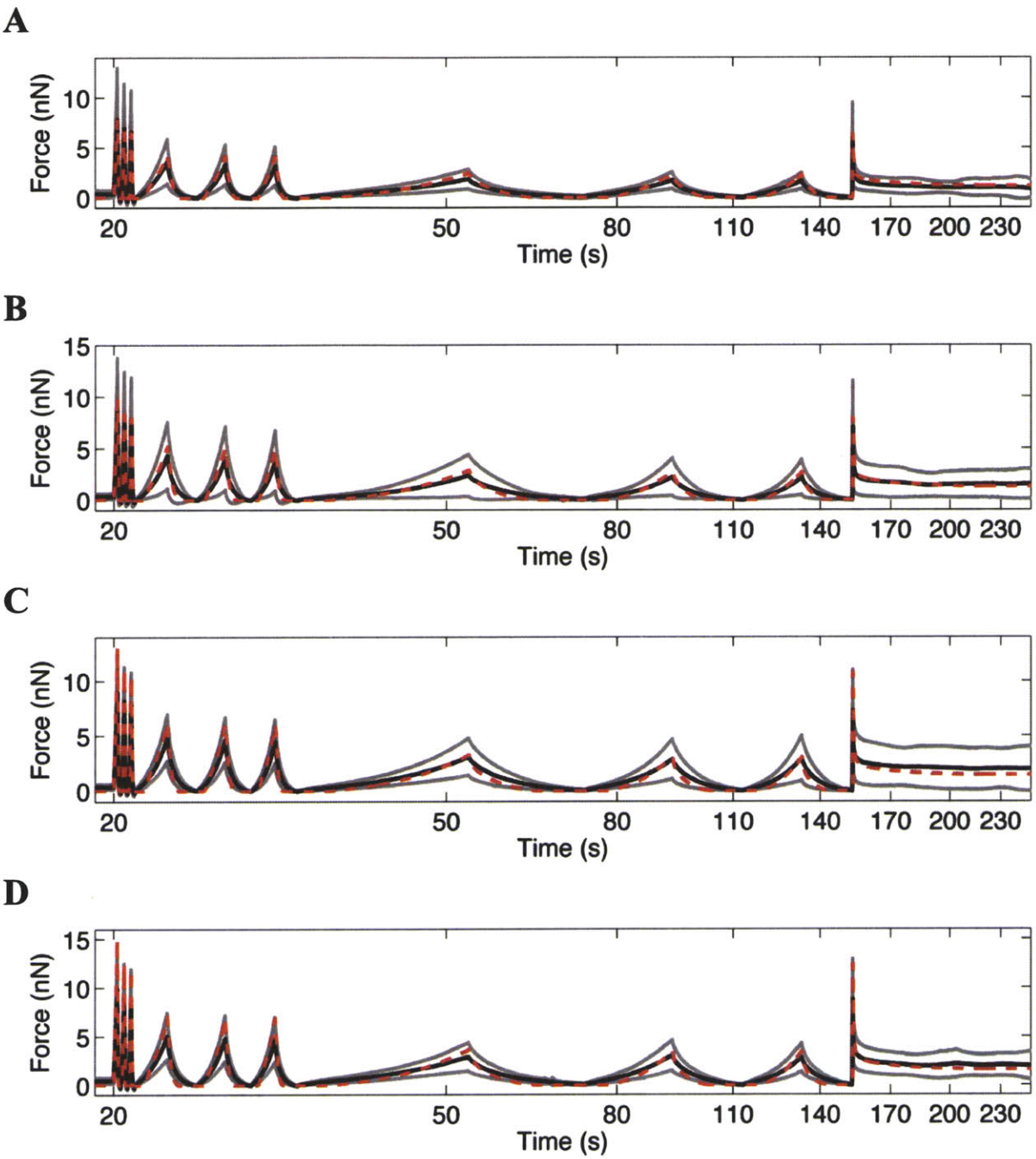

Figure 5-8: Neuron response and simulation results for cells on (A) Gel 1, (B) Gel 2, (C) Gel 3, and (D) Gel 4. Mean AFM data shown in black with +/- standard deviation in grey and simulation results with parameters obtained from fitting mean response on glass (Chapter 4). μ_o = 16 Pa, λ_L = 1.05, G_o = 75 Pa, G_∞ = 40 Pa, η = 3000 Pa.s, σ_o = 0.005 Pa, and n = 1. K was held constant at 10,000 Pa.

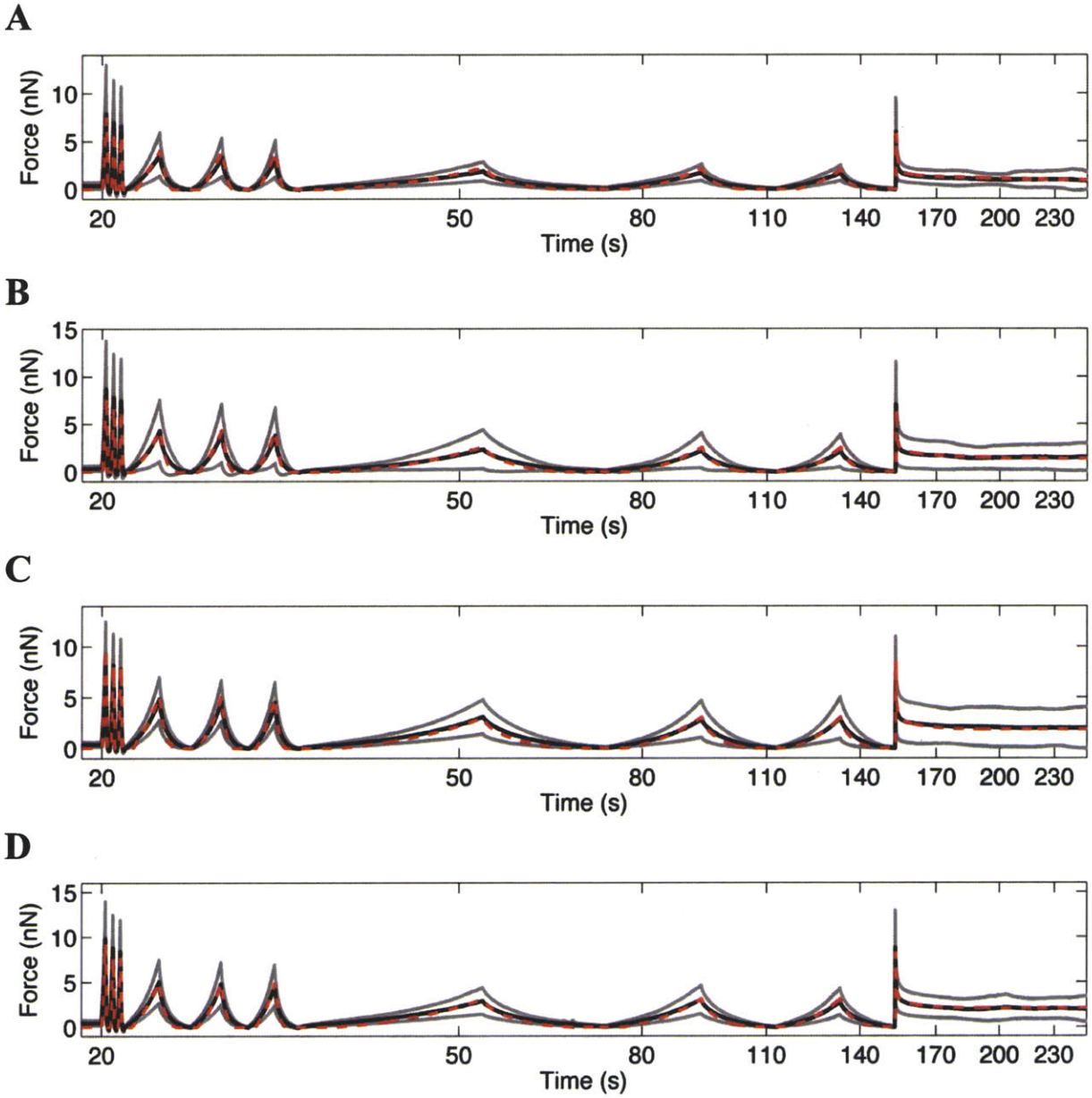

Figure 5-9: Neuron response and simulation results for cells on (A) Gel 1, (B) Gel 2, (C) Gel 3, and (D) Gel 4. Mean AFM data shown in black with +/- standard deviation in grey and simulation results with parameters calibrated to data for each gel and listed in Table 5-2.

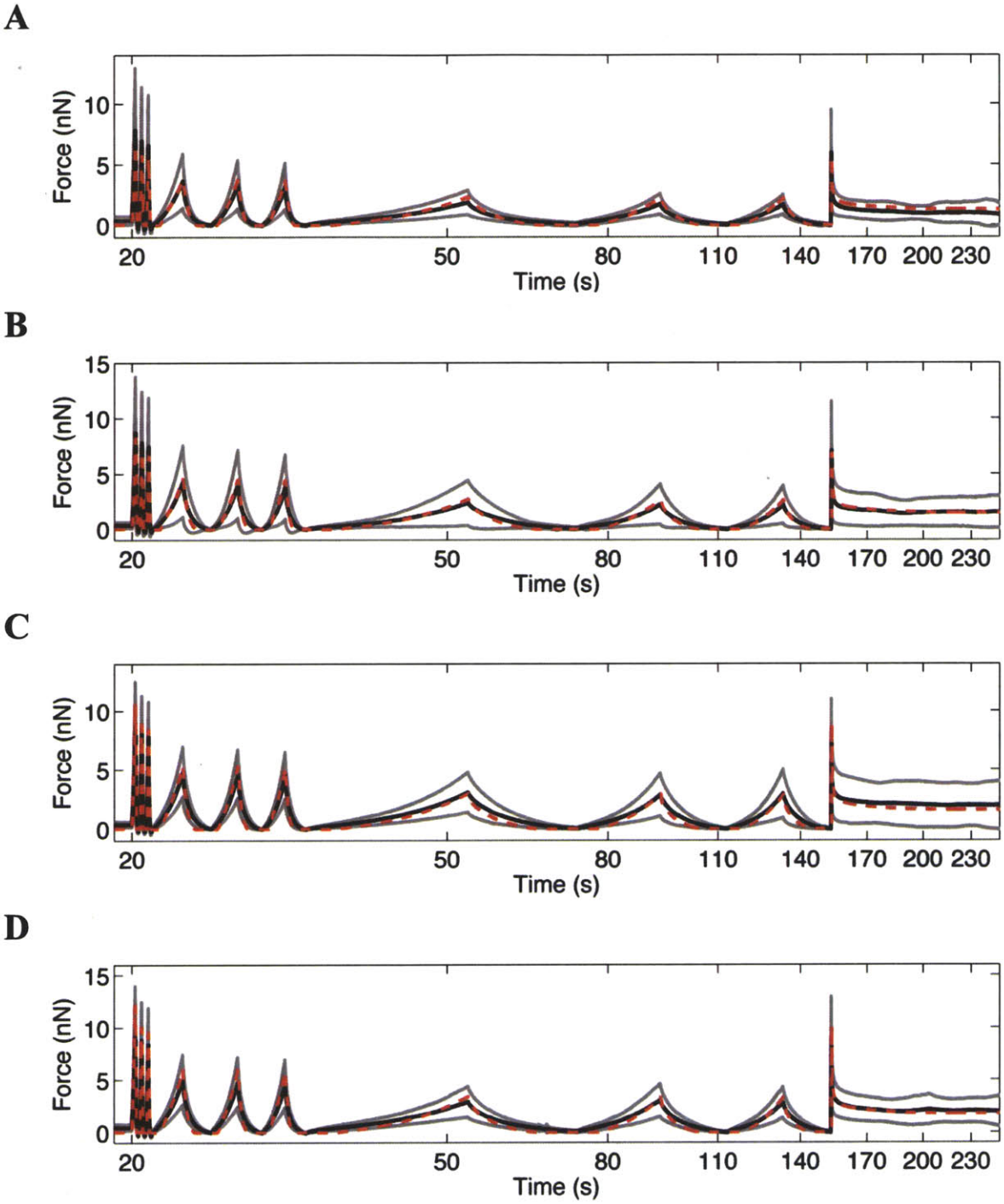

Figure 5-10: Neuron response and simulation results for cells on (A) Gel 1, (B) Gel 2, (C) Gel 3, and (D) Gel 4. Mean AFM data shown in black with +/- standard deviation in grey and simulation results with parameters obtained by taking the mean of optimized parameters obtained for all substrates (Listed as mean in Table 5-2).

A similar analysis was performed for astrocytes. As an initial test, simulations for astrocytes grown on each gel were run using material parameters obtained in Chapter 4 for characterizing the astrocyte response on glass. The simulation results and corresponding AFM data are shown in Figure 5-11. Interestingly, the parameters for glass are able to approximate the astrocyte response, including the significant decrease in force levels for astrocytes grown on Gels 1, 2, and 3, with the simulation results falling within one standard deviation of the mean for all substrates. This suggests that the shape change associated with softer substrates is more important in the observed changes in force response than the material properties of the astrocytes. In order to obtain a sense of the parameter variation required to obtain quality fits, mean data for astrocytes grown on each substrate were used to calibrate the model and yield sets of parameters for astrocytes grown on each substrate as shown in Figure 5-12 and Table 5-3. In order to attempt to find a set of unified parameters to represent astrocytes grown on all substrates, the simulations were run with the material parameters taken as the mean of the parameters obtained by fitting force response on each substrate (mean in Table 5-3). These results are shown in Figure 5-13.

	Astrocytes					
Parameters	**Gel 1**	**Gel 2**	**Gel 3**	**Gel 4**	**Glass**	**Mean**
G_0 (Pa)	240	200	240	275	275	246
n	0.90	0.75	0.92	0.80	0.80	0.83
σ_0 (Pa)	0.005	0.005	0.005	0.005	0.005	0.005
λ_L	1.08	1.08	1.09	1.08	1.08	1.082
μ_0 (Pa)	14	17	12	15	13	14.2
η (Pa.s)	300	300	300	300	300	300
G_∞ (Pa)	70	110	70	180	80	112

Table 5-3: Model parameters obtained by calibrating simulated response to mean AFM force data for astrocytes grown on different substrates. K was held constant at 10,000 Pa for all simulations.

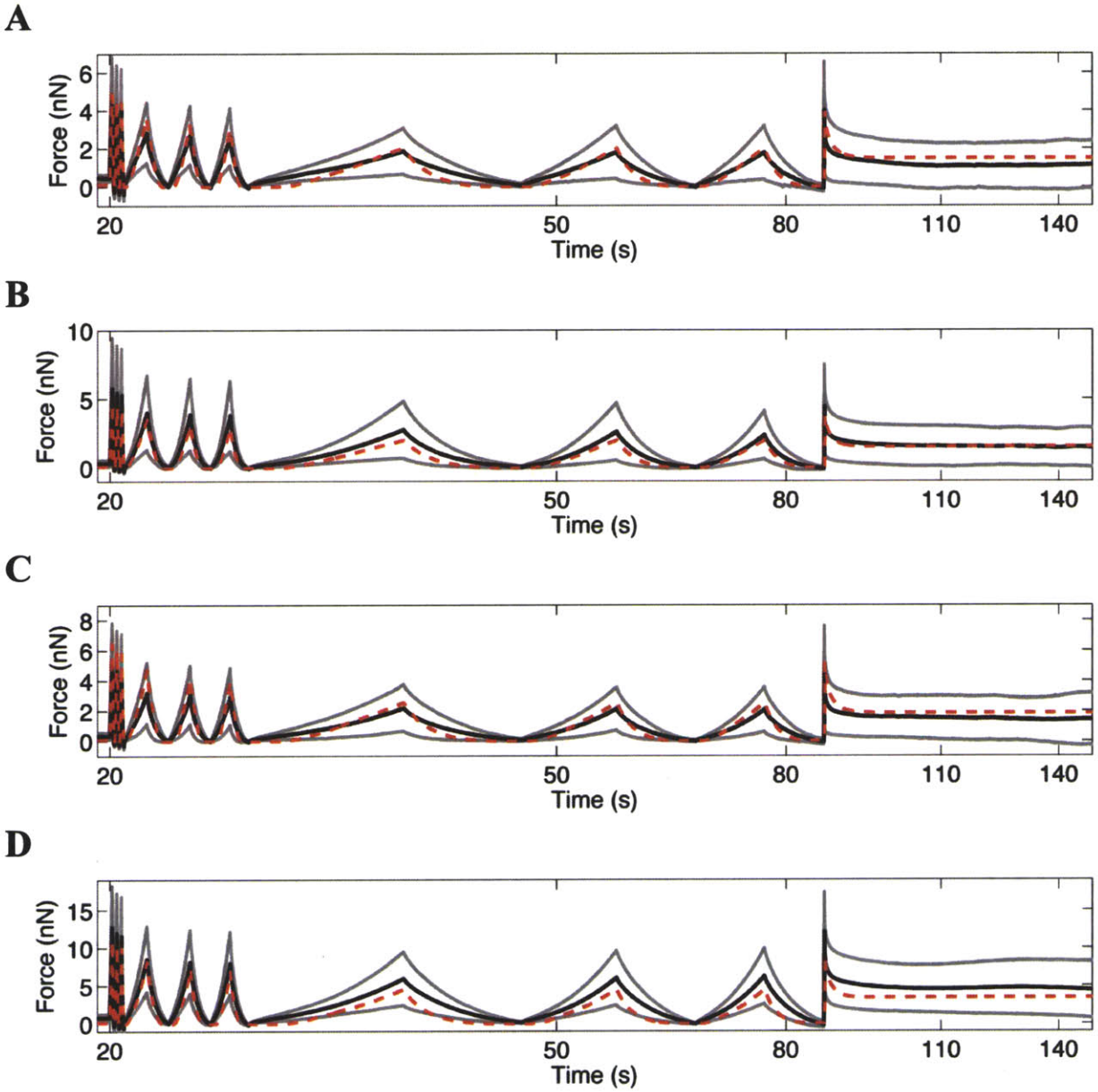

Figure 5-11: Astrocyte response and simulation results for cells on (A) Gel 1, (B) Gel 2, (C) Gel 3, and (D) Gel 4. Mean AFM data shown in black with +/- standard deviation in grey and simulation results with parameters obtained from fitting mean response on glass (Chapter 4). μ_o = 13 Pa, λ_L = 1.08, G_o = 275 Pa, G_∞ = 80 Pa, η = 300 Pa.s, σ_o = 0.005 Pa, and n = 0.80. K was held constant at 10,000 Pa

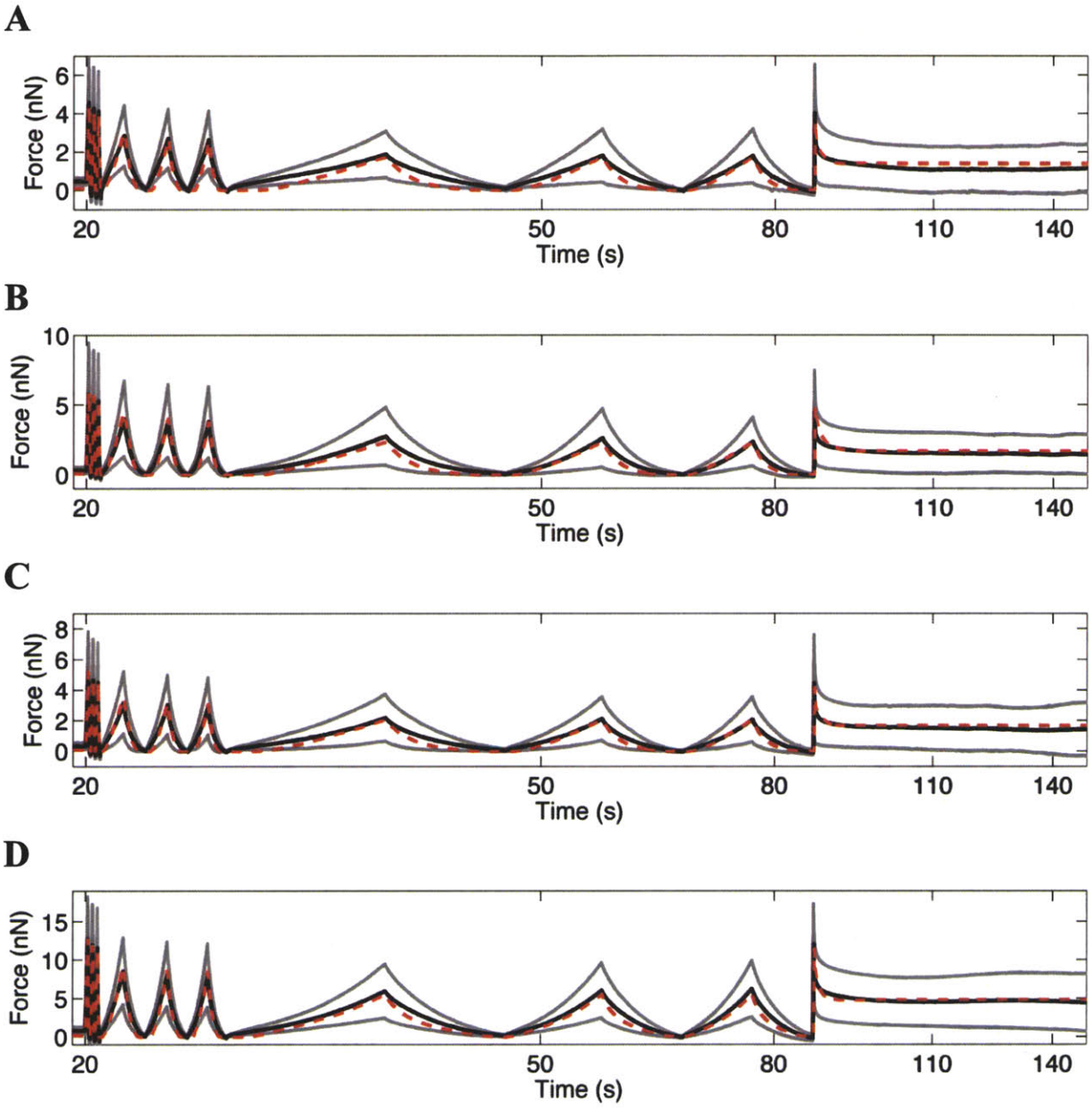

Figure 5-12: Astrocyte response and simulation results for cells on (A) Gel 1, (B) Gel 2, (C) Gel 3, and (D) Gel 4. Mean AFM data shown in black with +/- standard deviation in grey and simulation results with parameters calibrated to data for each gel and listed in Table 5-3.

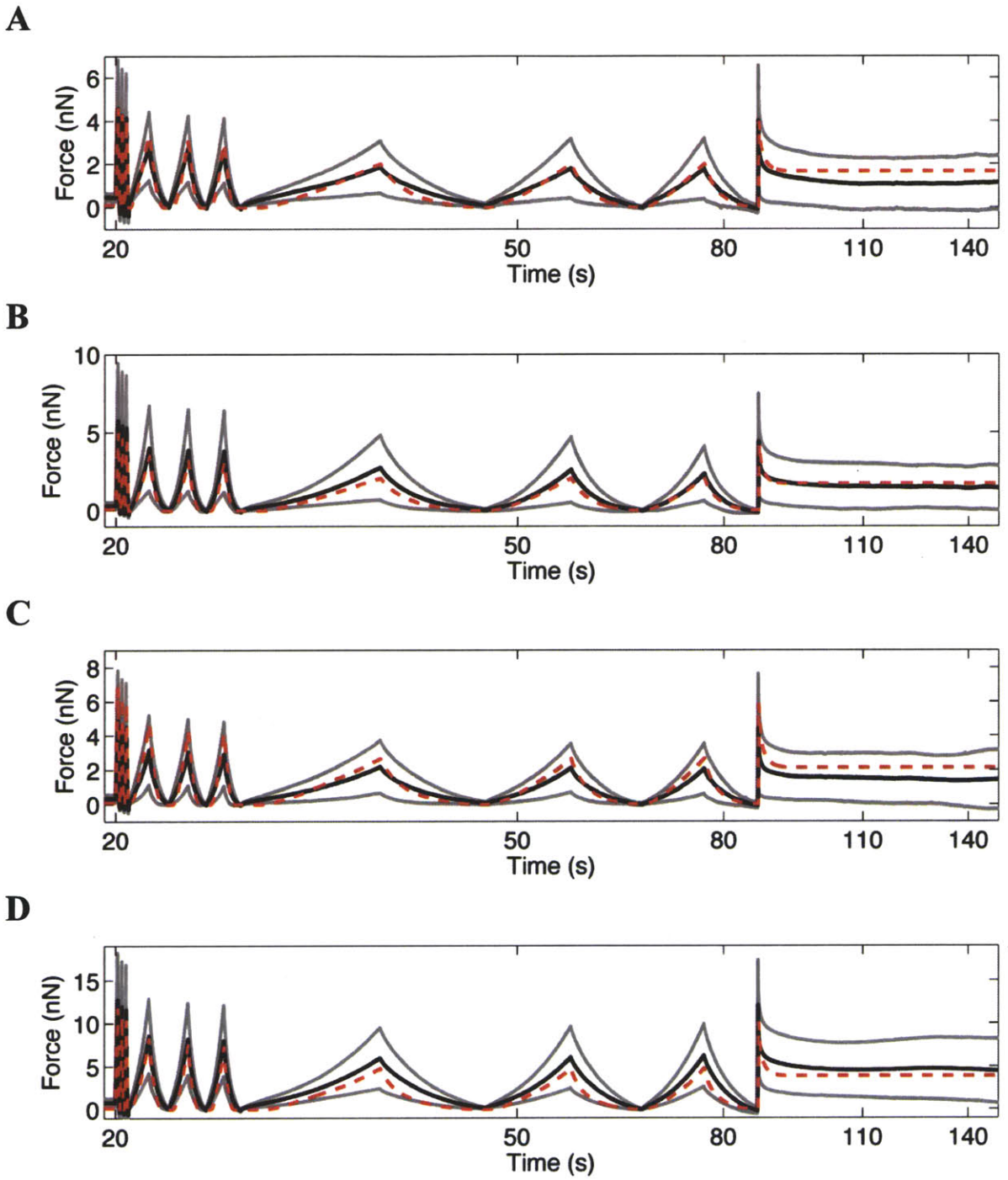

Figure 5-13: Astrocyte response and simulation results for cells on (A) Gel 1, (B) Gel 2, (C) Gel 3, and (D) Gel 4. Mean AFM data shown in black with +/- standard deviation in grey and simulation results with parameters obtained by taking the mean of optimized parameters obtained for all substrates (Listed as mean in Table 5-3)

To further investigate if morphology alone accounts for the observed changes in force response, the data for astrocytes grown on Gel 4 was separated into round versus spread populations as in Figure 5-7. Two new model geometries were created to match the average height and radius measured for both astrocytes classified as rounded and astrocytes classified as spread. The simulations were run using both the mean material properties and those obtained for fitting the average response of all astrocytes grown on Gel 4 (from Table 5-3). Rounded astrocytes were measured to have a height of 11.11 +/- 2.18 μm and a radius of 11.44 +/- 4.34 μm (mean +/- standard deviation). More spread astrocytes had a height of 6.95 +/- 2.03 and a radius of 26.77 +/- 9.71 μm. Results of the simulations showed that just changing the morphology in the model could account for the decreased force levels reached in the rounded cells (Figure 5-14). While there is error in the fits obtained with theses sets of parameters, with the simulations actually exhibiting a larger change in force levels than was measured in the experiments, considering the small sample size of rounded astrocytes grown on Gel 4 (N=8) and the fact that the simulations fall within 1 standard deviation of the mean, the simulations provide a sufficient approximation of the actual data for both sets of parameters tested and suggest that the changing morphology is mainly responsible for the changes in measured force response.

5.3 Discussion

This study investigates the influence of substrate properties not only on cell morphology, but on the cell material properties as well. Interestingly, while we noticed significant changes in the AFM force response of astrocytes grown on soft gels, simulations showed changing astrocyte morphology was more critical in accounting for this difference than changing cell material properties. When material properties were held constant at those obtained for astrocytes grown

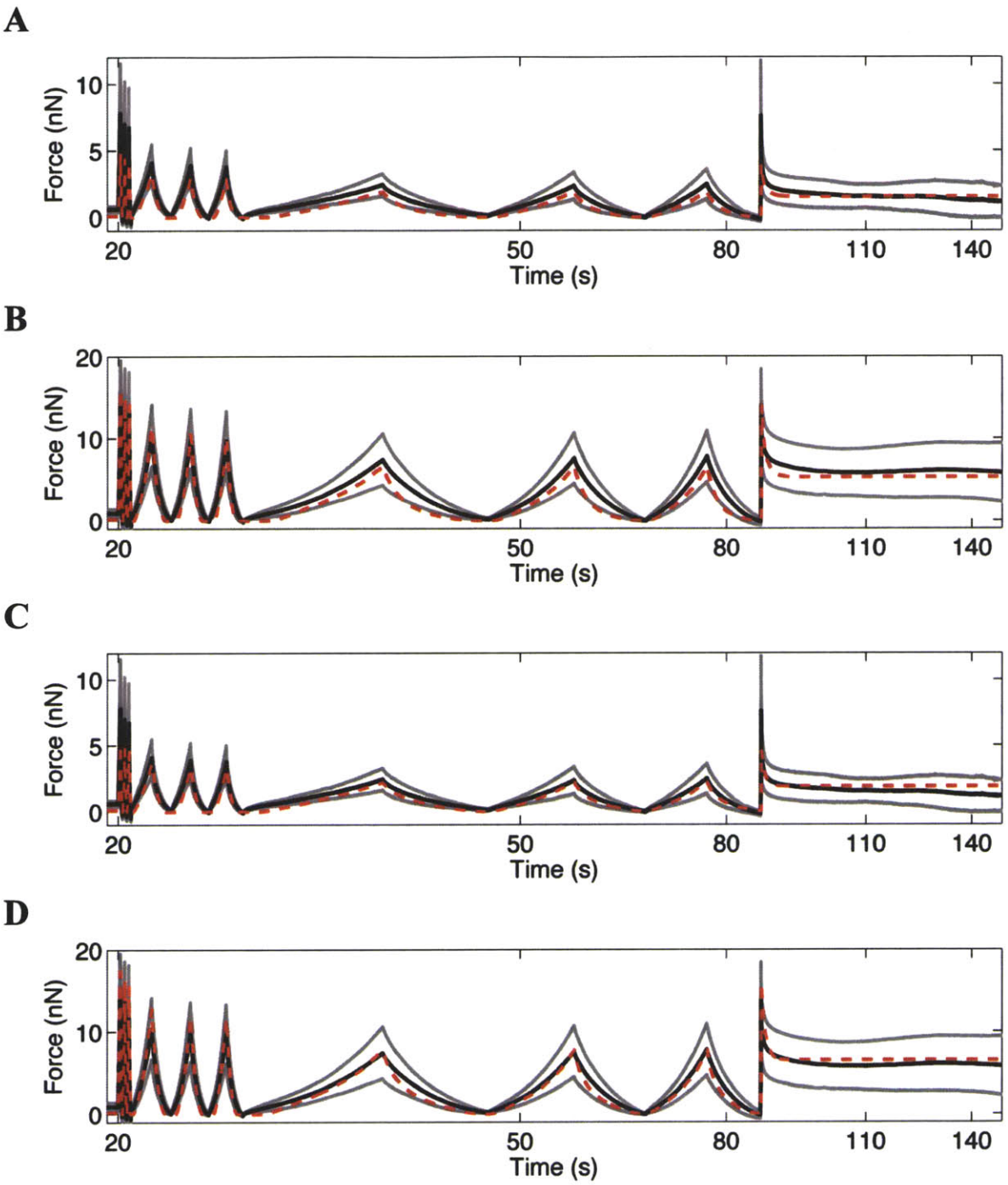

Figure 5-14: Astrocytes grown on Gel 4 classified as round (A) or spread (B) with simulation results obtained with mean parameters for astrocytes on all substrates (Table 5-3) and round (C) and spread (D) with simulation results obtained using parameters optimized for all astrocytes grown on Gel 4 (mean in Table 5-3).

on glass and cell geometry was changed to take on the more rounded phenotype observed on soft gels, the model also predicted a decrease in force levels. In contrast for neurons, no significant changes were observed in material properties or geometry. While morphological changes have been observed for neurons on different substrates [122, 125, 127], these changes were primarily in the growth cones and processes, which could explain why no changes in force response were detected at the soma level in our study. This work provides an important expansion on our previously published work on neurons cultured on glass substrates [76]. It greatly expands the applicability of our cell model, yielding parameters for the material properties of both neurons and astrocytes on a variety of substrates and indicating the importance of cell morphology on measured force responses.

These results provide support for our choice to analyze the AFM force data in such a way that cell morphology was taken into account. The finite element framework selected in this study enabled both cell morphology and cell material properties to be varied, leading to the conclusion that changing astrocyte morphology played a critical role in the observed changes in force response. This also suggests that further model refinements to more accurately represent the cell geometry instead of treating cells as ellipsoids may have a noticeable effect on the outcomes of the simulations. Further refinements in model geometry can be accomplished by using the geometries obtained from the confocal Z-stacks of each cell taken at the time of AFM indentation.

These findings also have important implications for studying TBI *in vitro* at the cellular level. In terms of developing accurate single cell and multi-scale models of mechanical loading, our results highlight the importance of selecting appropriate cell geometries to represent the cell in an environment relevant to the simulations. This is especially important when studying

astrocytes, which we showed to be more sensitive to changes in their environment than neurons. In the case of TBI and development of models of brain injury transients, it is essential to use properties and morphologies of cells measured on soft substrates to best mimic the conditions present in soft brain tissue.

Furthermore, for the development of relevant *in-vitro* experimental models to investigate the pathways, criteria, and thresholds of cell injury, it is necessary to select a substrate or matrix closely mimicking the mechanical properties of *in-vivo* conditions. For the case of astrocytes, the significant changes in force response and cell morphology demonstrate the importance of substrate selection in order to ensure an *in vitro* experiment is as biologically relevant as possible. Models in which the cells are grown in 3D cultures in compliant gels or in 2D on soft substrates are likely to be more relevant injury models. Systems that damage cells in 3D cultures such as that used by La Placa and Cullen *et al* are more likely to measure damage in cells with realistic morphologies [161, 163, 166]. In addition, testing the cells in a similar mechanical environment to what would be expected *in vivo* should yield more realistic injury thresholds and deformation profiles.

Other models such as uniaxial or biaxial stretch models offer interesting results, but our results raise questions as to the physiological relevance of the morphology and force response of CNS cells in those culture systems. For example, the material properties of cultured cortical astrocytes have been shown to decrease after injury in a stretch model in which cells were grown on silicone-based elastic membranes for 2 weeks prior to testing [7]. However, in order to fully understand this observation and its meaning for *in vivo* damage, it would be ideal to test the astrocytes on softer substrates on which the cells are more likely to exhibit similar responses to those observed *in vivo*. Changes in morphology and cytoskeletal structure observed on soft

substrates are likely to have an influence on how cells respond to stretch injury, especially when a measured outcome of the experiment is changes in cell material properties.

5.4 Summary

By growing cortical neurons and astrocytes on substrates of different stiffness, to our knowledge, the first quantitative analysis of how substrate properties influence the mechanical properties of neurons and astrocytes is presented. This work shows that force responses of astrocytes are very dependent on their substrate; however, changing morphology is able to account for much of the observed changes in force response. In contrast, neurons are not significantly affected by the properties of their substrate. In addition, the results of this chapter provide an expanded set of model material parameters to accurately represent neurons and astrocytes grown on a range of substrates. This work has important implications, not only for the development of multi-scale models, but also for the design of realistic *in vitro* cell damage systems.

Chapter 6

Design of Damage Devices

6.1 Introduction

In light of the data presented in section 2.1 on the prevalence of mild TBI in the military population for the recent conflicts in Iraq and Afghanistan, there is a pressing need for systems capable of creating mild TBI *in vitro* at the cellular level that share characteristics of damage with that found *in vivo*. Such systems enable controlled testing of the involvement of different cell types and measurement of cellular damage thresholds. In addition, they enable initial screening of potential therapeutics. As part of this thesis, two damage systems were developed to study the effects of traumatic brain injury at the cellular level *in vitro*. Both of these systems are capable of subjecting cell cultures to either single pulses or to a series of pulses, as well as to loading of different magnitudes. One system subjects the cell cultures to compressive loading, which is likely to have similarities to TBI from a blunt impact. The other system sends a shock wave through the cell cultures, simulating the causes of primary blast traumatic brain injury.

Development of a system to simulate a shock pressure transient at the cell culture level is a necessary advancement to provide a simplified experimental system, enabling better understanding of what happens at the cellular level after an explosion.

Both of these damage systems utilize cells grown in 3D collagen gel cultures. Based on our findings in Chapter 5, soft collagen gel should create an environment in which cell morphology and force response are similar to what is found *in vivo* in the soft brain tissue environment. In addition, using the same culture construct with two different damage devices and types of mechanical loading enables the comparison of different types of TBI and investigation into whether or not the same signaling cascades and pathophysiological responses are elicited after mechanical loading transients with significantly different characteristic times. Work done in this thesis provides a full characterization of the loading profiles of each device as well as their compatibility with cell cultures. To further characterize these devices and determine if they accurately reproduce key signaling pathways implicated in animal models of TBI, an ongoing collaboration was formed with the laboratory of Dr. Michael Whalen of the Neuroscience Center at Massachusetts General Hospital to directly compare results of damage with our cell culture systems with that found in their *in vivo* mouse models of TBI.

6.2 3D Cell Cultures

Cell culture constructs were created as a two-layer collagen gel, with the thick, lower layer consisting of unseeded collagen and the thin, top layer containing the cells (Figure 6-1). This arrangement was selected to provide a sufficiently thick specimen for mechanical loading, but a thin enough gel environment around the cells to ensure adequate diffusion of nutrients. In addition, the gels are compatible with pure neuron, astrocyte, and microglia cultures, as well as

with co-cultures containing any combination of the three cells types. This enables investigation of how the different cell types in the brain respond to mechanical loading and whether a single cell type is enough to elicit a damage response similar to that found *in vivo*, or if all cell types must be present together to enable the complex signaling network and damage markers.

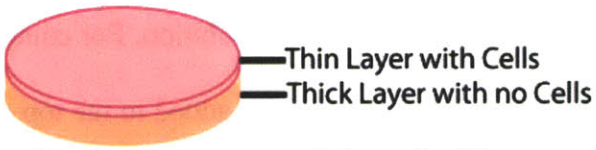

Figure 6-1: Collagen gel cell culture system consisting of a thin upper layer containing cells and a thick lower layer with no cells.

Collagen gels were created with rat-tail collagen type 1 in acetic acid (354236, BD Biosciences, San Jose, CA) following the manufacturer's instructions for creating a 1 mg/mL collagen gel. This concentration of collagen was selected to form a gel that was stiff enough to enable gel manipulation but still soft enough (with a modulus less than brain tissue) to enable long neuron process formation (based on studies finding lower concentrations of collagen to favor neurite outgrowth [189, 190]). Collagen gels at room temperature, thus prior to starting gel preparation all reagents were placed on ice. Each batch of collagen stock solution has a different starting concentration and amounts had to be adjusted accordingly for each batch of collagen. For a 3.68 mg/mL collagen stock solution used to create 10 mL of 1 mg/mL collagen gel, 1 mL 10X PBS, 62.5 μL 1 N sodium hydroxide, and 6.22 mL sterile filtered distilled water were added to a 15 mL tube and mixed well. While being careful to not let the solution warm up, 2.72 mL collagen was added and mixed gently by inverting the tube. The solution was returned to ice prior to addition to the well plates and remained stable for up to 3 hours.

To create the thick bottom layer, the 1 mg/mL collagen solution was plated in either a 24 well plate for compression studies or a 6 well Flexcell plate for blast studies. For compression

studies, 500 μL of collagen solution were added to each well and for blast studies, 2 mL of collagen solution were used. The resulting gels were placed in a 37 °C incubator and allowed to gel for 8 h prior to adding the top, cell-containing layer. To create the thin top layer containing cells, collagen solutions were prepared as described for the thick layer, with cell suspensions added after the addition of the collagen stock solution. To ensure the gel still set properly, cell suspensions made up less than 10% of the total gel solution. For compression studies, 250 μL of the collagen solution containing cells were carefully added to the top of each hardened thick gel. For blast studies, 1 mL of the collagen solution containing cells was added to the set gels in the Flexcell plates. The gels were returned to the 37 °C incubator and allowed to gel. After 2 h, media was gently added to each well. Media was changed every 3-4 days.

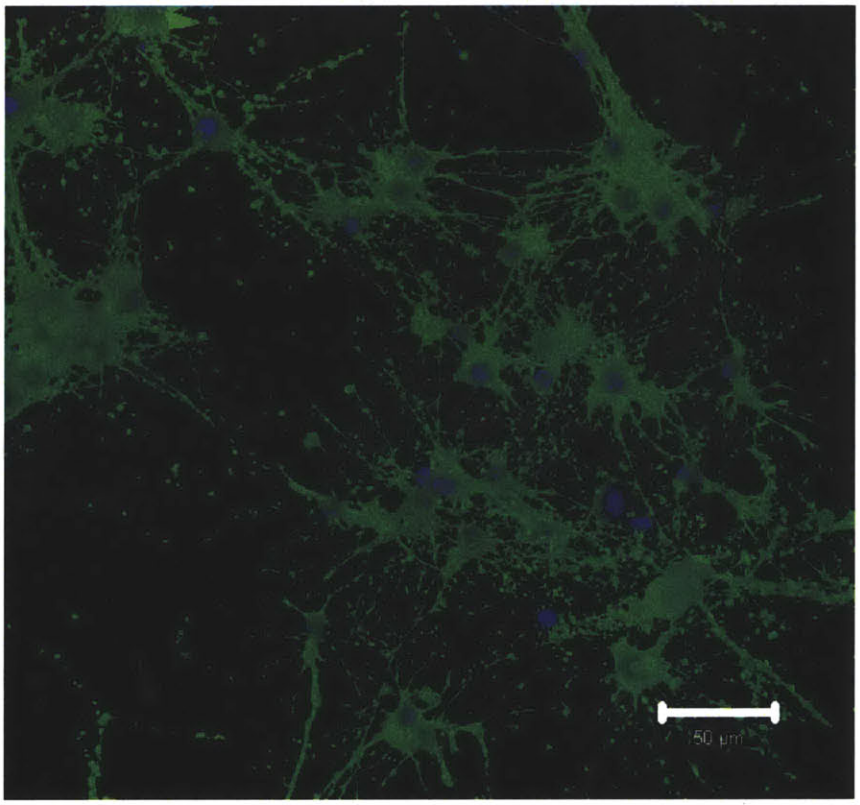

Figure 6-2: Confocal image of representative gel, containing both neurons and glia, showing cells are in close proximity and able to contact and communicate with one another. The cytoplasm is stained with calcein-AM (green) and the nuclei with Hoechst (blue).

Cell suspensions were obtained as described in section 3.2.1. For pure neuronal cultures, cells were used immediately after dissociation and grown in serum free media (Neurobasal supplemented with 1X B27 and 1X Glutamax). Neurons were maintained in culture for two weeks to enable growth of long processes and formation of synapses. Glia were first grown in culture flasks to obtain pure cultures prior to seeding in the gels. Confocal imaging of gels containing both neurons and glia showed that cells were in close proximity and able to contact and communicate with one another (Figure 6-2).

6.3 Shockwave device

In order to simulate primary blast injury at the cellular level, a system was developed to send a shockwave through cell culture constructs. This system consists of a few key components, a machine to generate the shockwave, cell culture constructs in Flexcell plates, and a needle hydrophone and data acquisition system to record the signal as shown in Figure 6-3. The entire system is placed inside a laminar flow hood to minimize possibilities of contamination (Figure 6-3 B). Tests are performed in culture medium and the entire damage process takes just a few minutes ensuring the cells remain outside the incubator for a minimal amount of time. After testing, cells are immediately returned to the 37 °C incubator.

This system utilizes an EMS Swiss Dolorclast extracorporeal shockwave device (Electro Medical Systems, Dallas, TX) to generate the shockwave. The Dolorclast device works via pneumatic generation of a shockwave. Briefly, it uses a compressed air impulse to accelerate a projectile against the tip of the applicator. When the projectile hits the curved surface of the applicator, a shockwave is generated and delivered to the cell cultures, as shown in Figure 6-4. The Dolorclast generates an unfocused, radial shockwave, enabling the shockwave to be

delivered to a larger area. Characteristic rise times, pressures, and energy levels of the Dolorclast shockwave are listed in Table 6-1. Chitnis and Cleveland compared the Dolorclast shock device to two other shockwave therapy devices utilizing electrohydraulic methods of shock wave generation [191]. They found the Dolorclast to reach lower overpressures and have an increased duration of the positive phase of the pressure wave. Also they found the peak pressure could be changed by controlling the energy setting of the Dolorclast device. These characteristics make the Dolorclast a favorable choice for simulating blast injury in cell cultures.

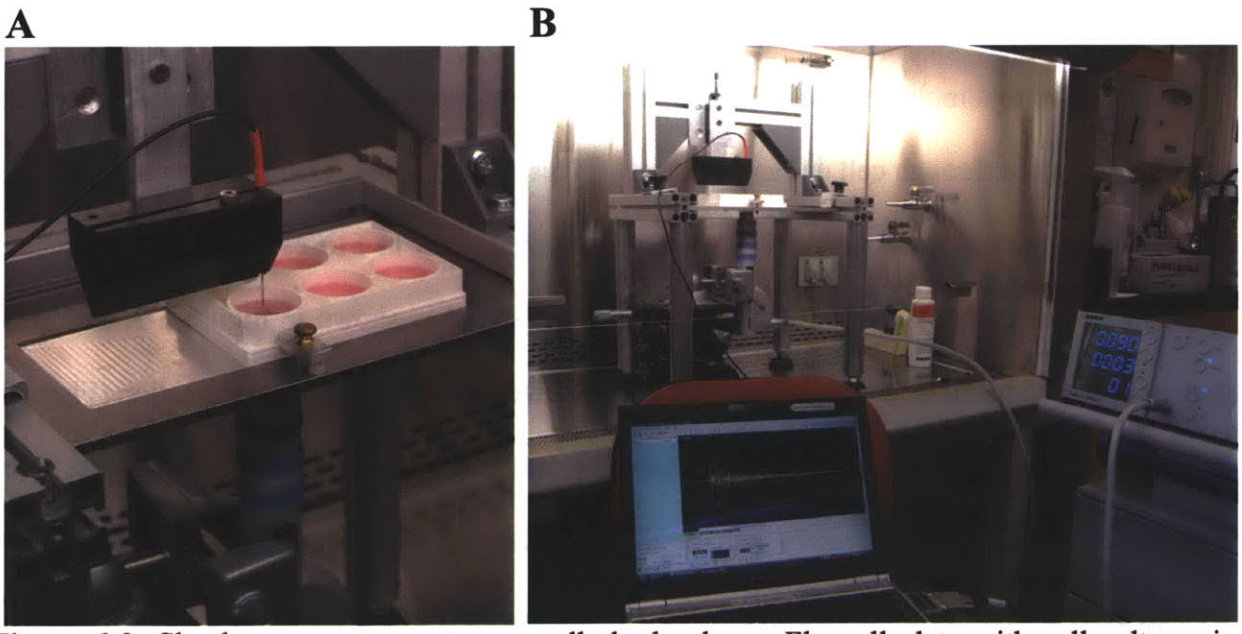

Figure 6-3: Shockwave system set-up: needle hydrophone, Flexcell plate with cell cultures in collagen gel, Dolorclast machine coupled to the underneath of well plate with coupling gel, and computer running data acquisition system.

Cells are grown in collagen gels in Flexcell six-well culture plates (Flexcell international, Hillsborough, NC) as described in section 6.2. The Flexcell plates contain a silastic membrane at the bottom of each well. Tissue Train circular foam culture plates coated with collagen are used in the tests to facilitate gel attachment to the plates. This membrane enables the shockwave to be

sent from underneath the cell cultures, while minimizing interface changes. The tip of the Dolorclast gun is coupled to the bottom of the Flexcell well with ultrasound coupling gel. The coupling gel enables the shockwave to be sent into the well without the applicator tip stretching the membrane and also helps minimize reflections and loss of signal upon entry of the shockwave into the cell cultures.

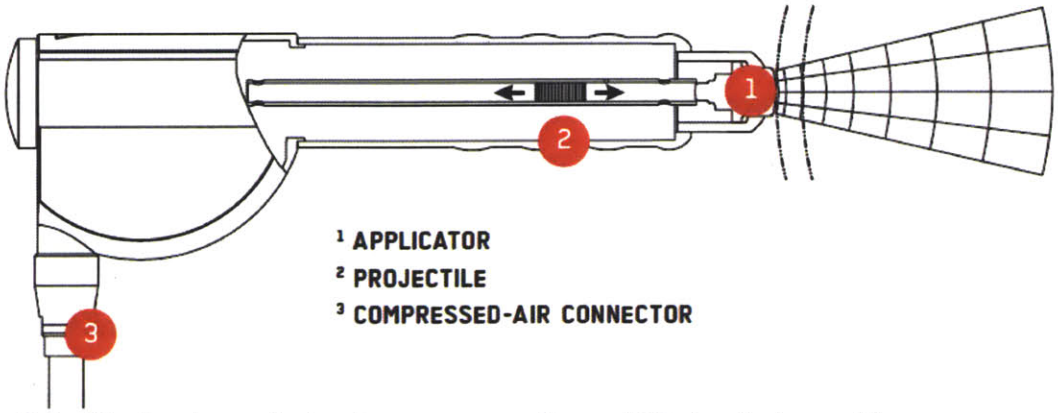

Figure 6-4: Mechanism of shockwave generation of Dolorclast machine: a compressed-air impulse accelerates a projectile in the gun; the projectile contacts the tip of the applicator; the resulting shockwave is delivered to object in contact with the tip. (Image taken from http://www.dolorclast.com/page_productinfo_devicebrochure.php)

Parameter	Dolorclast Machine
Peak Positive Pressure [MPa]	11.9
-6 dB focal area, $f_x = f_y$ [mm]	8
-6 dB focal area, f_z [mm]	8
Total energy flux density [mJ/mm^2]	0.18
Total energy in -6 dB focus [mJ]	5.4
Total energy in 5 mm focal area [mJ]	11.9
Peak negative pressure [MPa]	-5.86
Rise time [μs]	3
Compressive Pulse width [μs]	2.5

Table 6-1: Specifications reported on the Dolorclast device. Adapted from Kearney [4].

The pressure profile that the cells experience is recorded via a needle hydrophone inserted from the top, into the collagen gel. The needle hydrophone selected for this system is an

HNS needle hydrophone as shown in Figure 6-5 (Onda, Sunnyvale, CA). The needle hydrophone is compatible with the cell cultures, being both small enough to insert into the gels and working in the cell culture media. This needle hydrophone has a flat response between 1 and 10 MHz and it can measure pressures between -10 MPa and 200 MPa. The Dolorclast waveform has a characteristic frequency of 1 MHz, compatible with the HNS needled hydrophone, however, it has been shown to also have components as low as 10 kHz [192]. In order to test the appropriateness of the HNS needle hydrophone for capturing the Dolorclast shockwave, Kearney [4] also measured the shockwave with a hydrophone with a lower bandwidth spectrum. He found the two different hydrophones measured similar pressures and characteristic times for the Dolorclast, suggesting the HNS needle hydrophone is appropriate for capturing the major components of the Dolorclast Shockwave. The compatibility of the HNS Needle hydrophone with the cell cultures, as well as its demonstrated ability to capture the key components of the Dolorclast shockwave make it an appropriate choice for measuring the pressure profile actually experienced by the cells.

Figure 6-5: Onda HNS needle hydrophone used for measuring pressures in collagen gels. From http://www.ondacorp.com/images/brochures/Onda_HNS_DataSheet.pdf

In order to characterize how the Dolorclast signal is transmitted to different areas of the culture well, the needle hydrophone was placed at different locations in a Flexcell well containing PBS and the pressure waves were measured. Results showed that the signal was the strongest directly above the center of the Dolorclast tip (6-6 A) and the maximum pressure decreased as the hydrophone was moved towards the edge of the well (6-6 B). It is interesting to note that even off the edge of the Dolorclast tip, a pressure on the order of 1 MPa was still recorded (Figure 6-6 C). This suggests that all cells in the culture will experience a shock wave, with those in the center receiving the greatest pressure.

The signal obtained from multiple consecutive pressure pulses was also characterized in Flexcell plates containing PBS. Both 2 and 10 consecutive pulses were monitored. The measured pressures for both 2 and 10 consecutive shocks are shown in Figure 6-7. This characterization showed the time between pulses to be consistent and each of the pulses to be a true shockwave. There was some variation between the maximum pressures reached over the 10 pulses. Some of this variation may have been due to under sampling the signal in order to acquire all 10 pulses, and the true peak may have not been captured. In addition, there was a small variation in the timing of later pulses as shown in Figure 6-8 B. The timing of the first pulse (Figure 6-8 A) lines up over four sample firings, however, by the tenth pulse (Figure 6-8 B) there is variation in firing times between the four tests. Despite the minor variation, the first and last shockwaves, in a series of ten, are qualitatively the same, reaching similar pressure levels, lasting for the same duration, and represent the expected characteristics of a shockwave from the Dolorclast machine as shown in Figure 6-8 C, D. This characterization shows the Dolorclast can be used to send either a single shock or a reproducible series of shockwaves into the cell cultures in a short period of time.

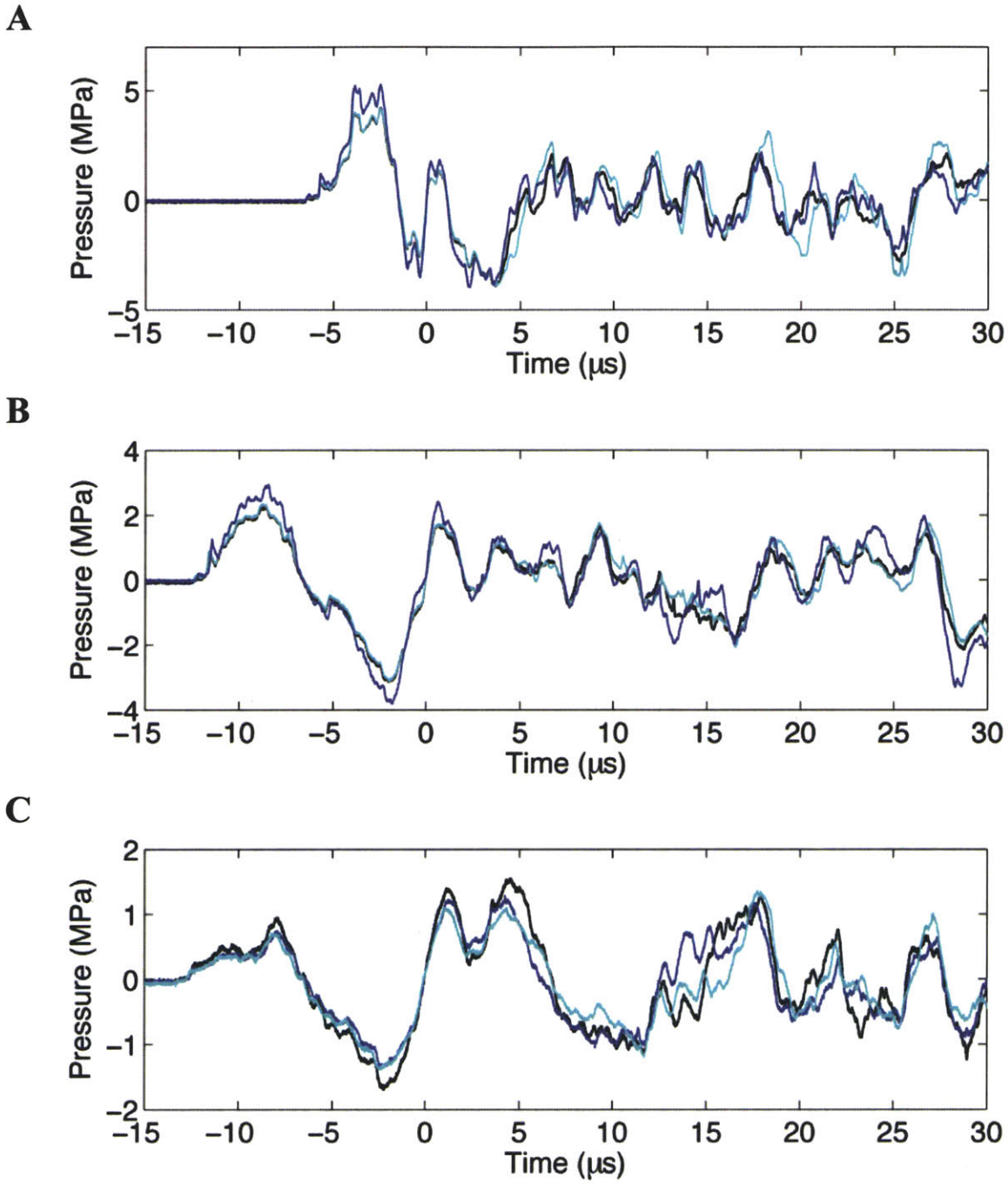

Figure 6-6: Characterization of the pressure signal measured at different locations in the Flexcell well in PBS with respect to the tip of the Dolorclast gun: (A) Centered, (B) at edge of tip, (C) off edge of tip.

A

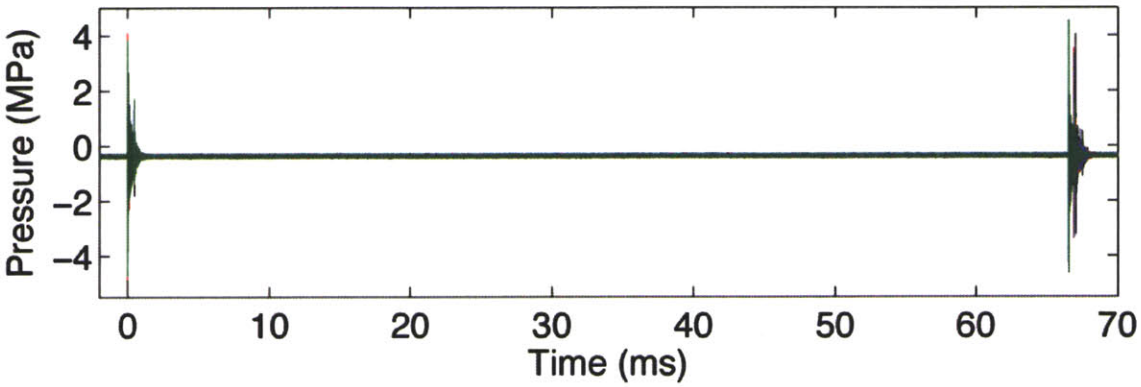

B

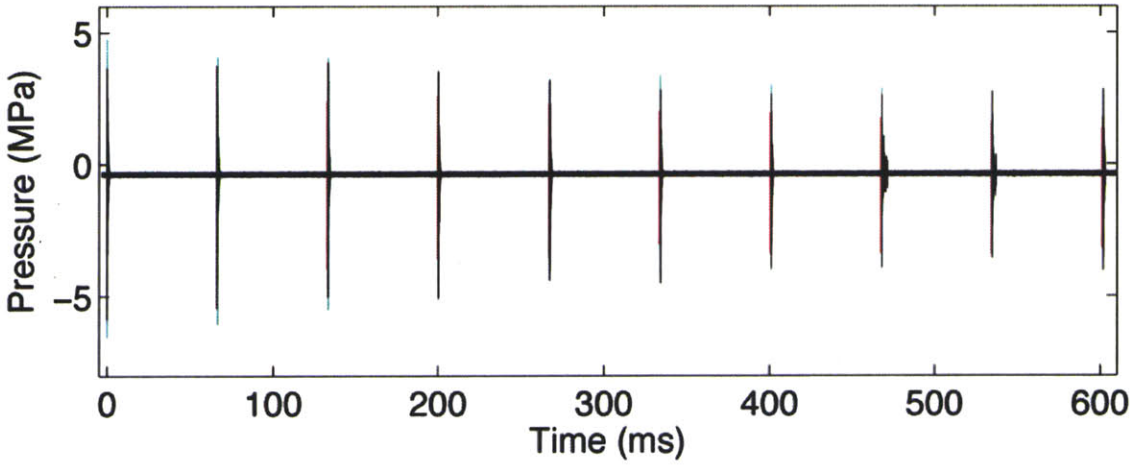

Figure 6-7: Characterization of pressure signal of 2 consecutive pulses (A) and 10 consecutive pulses (B) in a Flexcell well containing PBS showing the time between pulses and the pressures reached for pressure trains taken at 15 pulses per second.

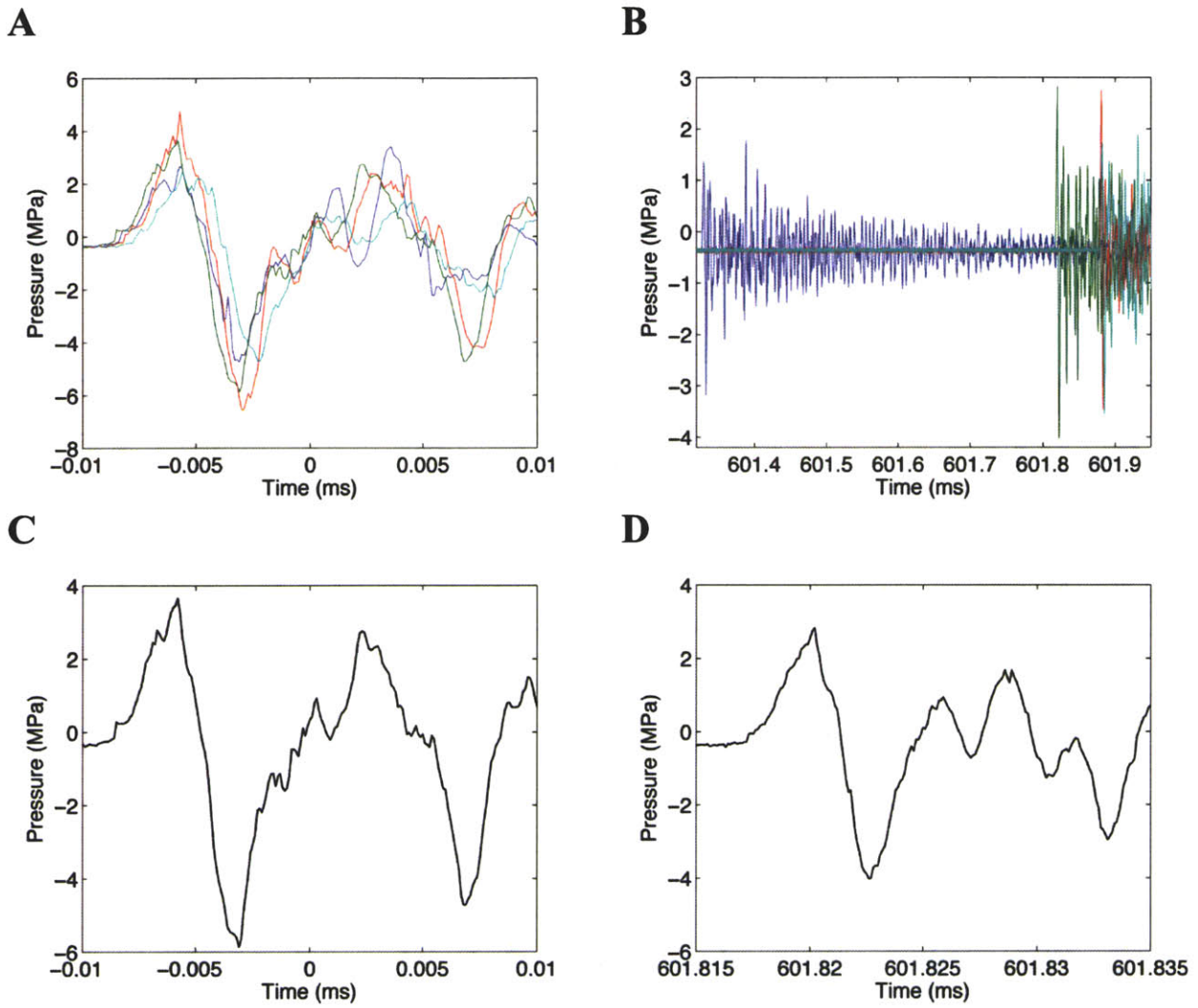

Figure 6-8: Characterization of the change in pressure signal between the first and tenth shock taken at a frequency of 15 shocks per second in a Flexcell well containing PBS. Zoomed in view of the first pulse (A) and the tenth pulse (B) in the series for 4 different sequences of 10 shocks showing the timing of the initial pulse is consistent but there is some variation in the timing of the tenth pulse, with the sample in blue arriving earlier than the other 3 samples. Zoomed in view of the first (C) and the tenth pulse (D) for a single pressure measurement showing the change in pressures reached between the initial and final shock.

In addition, the Dolorclast system has various options for the geometry of the applicator tip as well as guns of two different powers. Tips are available with different radius, longer shaft length, and with a concave tip instead of the standard convex tip. These tips increase the flexibility of the Dolorclast system, allowing administration of shock waves with different pressure profiles. One tip was of particular interest to our studies, having a longer shaft length. In

order to characterize how the increased shaft length changed the pressure wave, the pressure signal was measured in a Flexcell plate containing PBS. When compared with the standard tip, the longer tip resulted in an elongated shockwave as shown in Figure 6-9. This is of considerable interest for simulating blast TBI, as the shockwaves resulting from explosions take place on a longer time scale than the shockwaves generated by the Dolorclast machine. In addition, to characterize options for changing the maximum overpressure of the device, different magnitudes of pressure were generated using the higher power gun as well as the normal gun with the output of the device decreased. These results, shown in Figure 6-10 show that different magnitude pressures can be obtained by changing the output of the system and by changing between the normal and high-power guns.

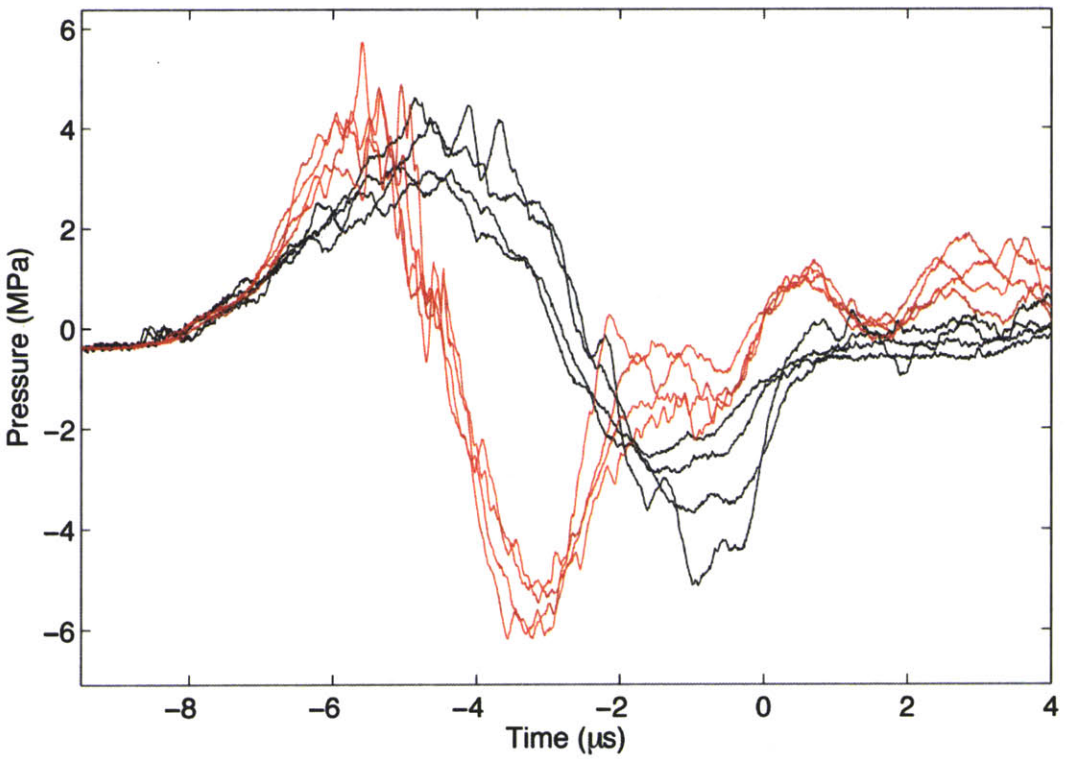

Figure 6-9: Comparison of the shockwave obtained with the standard Dolorclast tip (red) and with a tip with elongated shaft (black). The longer tip produced an elongated shockwave. Measurements were taken in Flexcell wells in PBS.

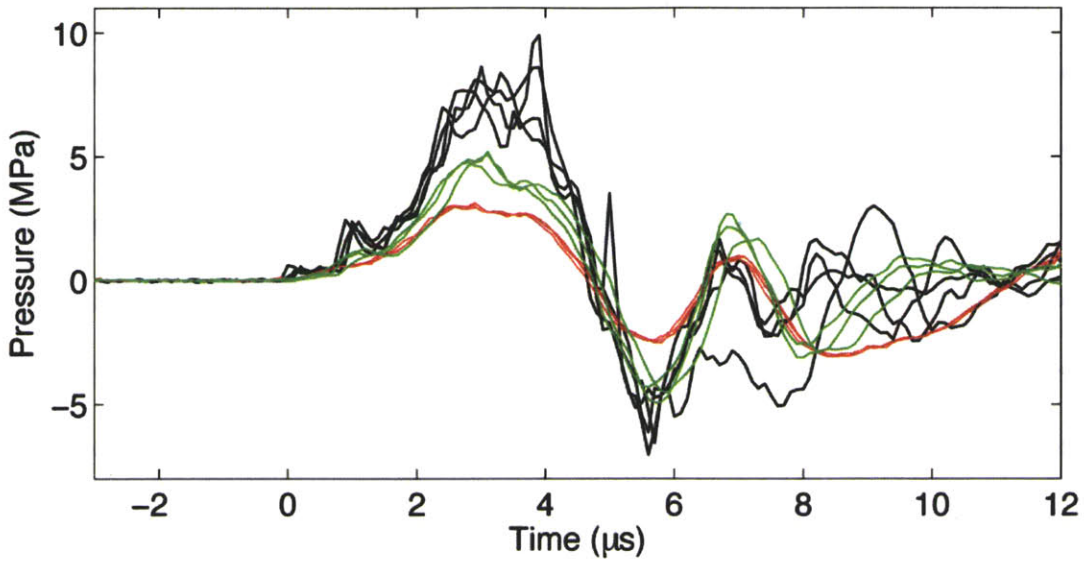

Figure 6-10: Comparison of the shockwave generated with the high-powered gun (black), the normal gun (green) and the normal gun at reduced output (red).

The reproducibility of the pressure pulse when switching wells, as would be done during an experiment shocking cells, was also characterized. This is essential to ensure comparable pressure profiles are measured after adding new coupling gel and repositioning the gun and hydrophone in each new well. Results, shown in Figure 6-11, showed that there was some variation in overpressure, on the order of what was also observed in other experiments in PBS in a single well, and the timing and qualitative shapes of the shockwaves were the same upon changing wells.

In order to ensure that the whole system was compatible with cell cultures, that the tests could be carried out in a sterile manner, and that the shockwave was of an appropriate level to not cause complete cell death, collagen gels containing astrocytes were tested with the system. Astrocytes were seeded in the collagen gels and allowed to grow in culture for two days, at which time shock wave tests were performed. When coupling the Dolorlast tip to the bottom of the Flexcell plate, care was taken to just come in to contact and not stretch the membrane,

ensuring the shockwave was the only mechanism of loading on the cell cultures. The needle hydrophone was placed in the center of the culture well. Experimental culture wells were each administered one shock, at the maximum energy setting of the Dolorclast machine. Control wells received no shocks but were loaded in to the testing configuration and remained out of the incubator for the same period of time. The measured shock waves are shown in Figure 6-12. The pressure profile was found to be roughly reproducible, reaching similar force levels in each well, however some variation was observed. After 48 hours, no contamination was observed and a viability assay was performed to assess general health of the cultures. Calcein-AM was used to identify live cells and ethidium homodimer 1 (Invitrogen, L-3224) was used to label the nuclei of dead cells. Results of the viability assay showed that the cells remained viable 48 h after testing (Figure 6-13). Samples were imaged using a confocal microscope (Zeiss LSM 700, Carl Zeiss Microimaging) to examine the distribution of cell viability throughout the depth of the gel construct. The fact that cells remained viable in culture 48 h after damage suggests this system is ideal to study mechanisms of TBI unfolding in the hours to days after injury. This type of injury could be characteristic of mild bTBI.

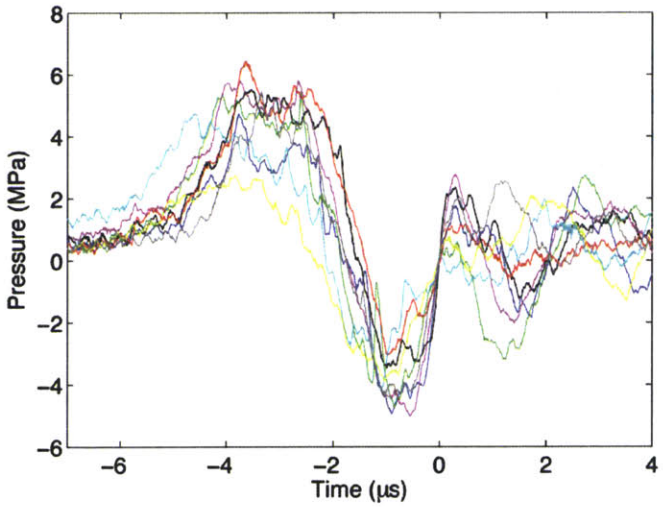

Figure 6-11: Characterization of the reproducibility of the shockwave when switching between 8 different wells containing unseeded collagen gel and culture media.

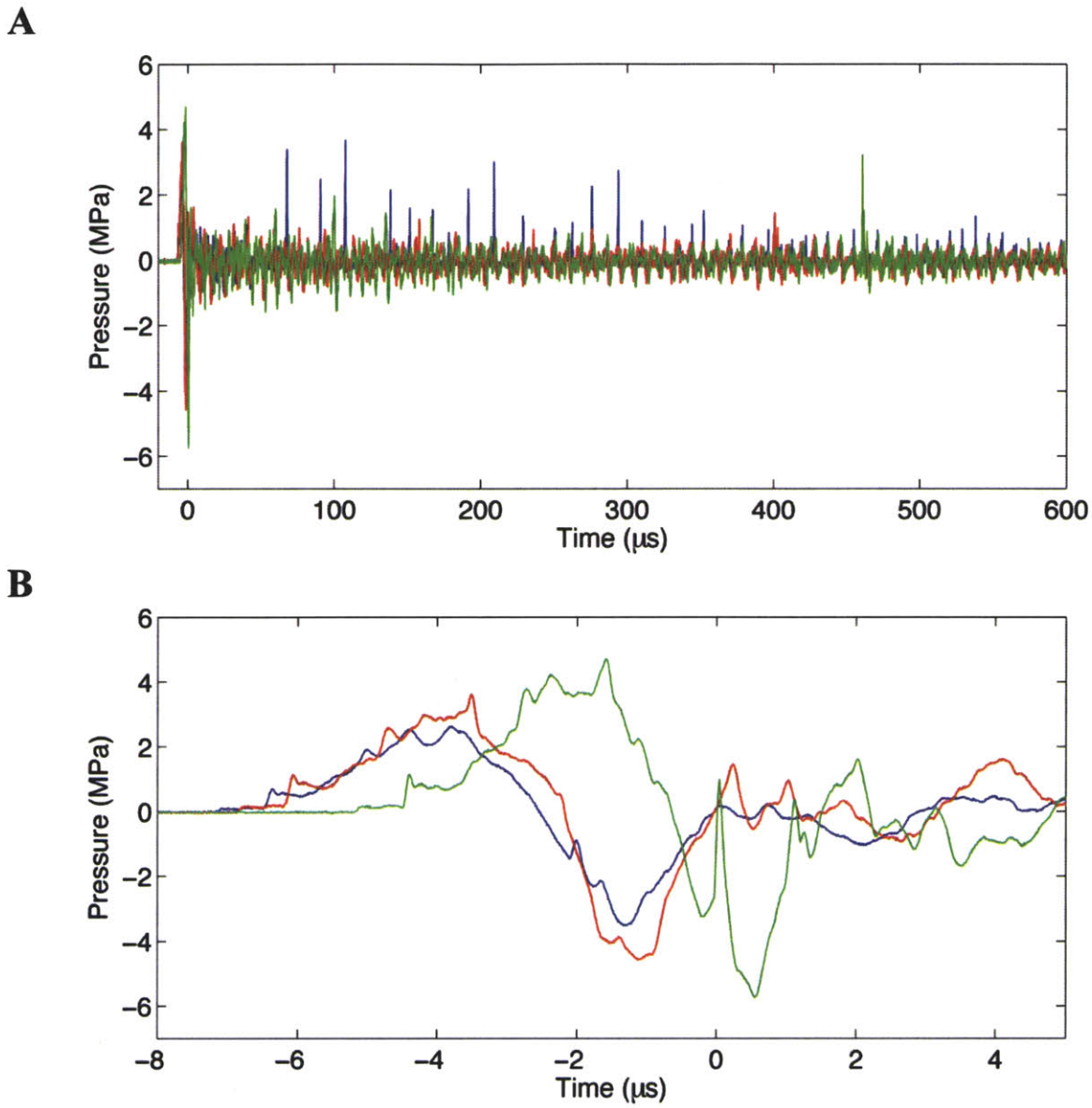

Figure 6-12: Pressure profiles measured in 3 wells containing collagen gels seeded with astrocytes. The full signal including reflections is shown in (A) and a zoomed in view of the initial shockwave is shown in (B).

To better validate the shockwave system as a model of TBI, tests are underway in an ongoing collaboration with the laboratory of Dr. Michael Whalen at Massachusetts General Hospital to compare the changes in signaling pathways in the cell cultures after blast with changes identified in mouse models of TBI. Samples of rat cortical neurons, astrocytes, and microglia as well as co-cultures will be administered different numbers of shock waves and

frozen at time points up to 24 hours after damage, followed by western blots to assay for signaling molecules such as TNFα, Akt, and p-S6. These experiments will provide better validation of our cell damage system as a realistic model of TBI.

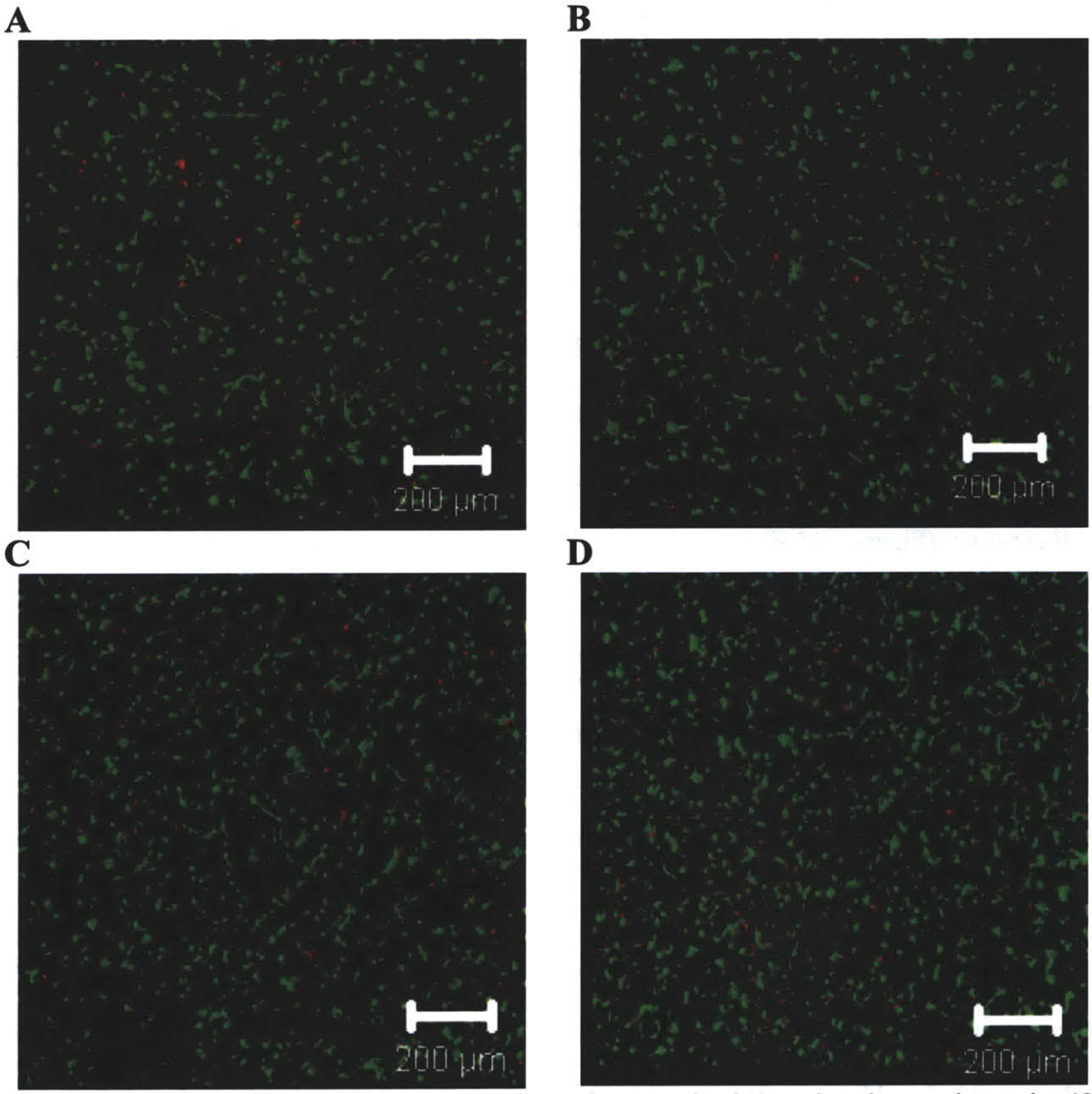

Figure 6-13: Viability assay on astrocytes subjected to one shock (A, B) and control samples (C, D). Live cells labeled with Calcein-AM (Green) and dead cell nuclei labeled with Ethidium Homodimer 1 (Red).

6.4 Compression Device

Injury similar to that from an impact was generated *in vitro* using a compression system. A custom voice coil device, originally designed for the indentation of porcine tissue was used to compress the cell cultures. This device consists of a displacement sensor (Transtek, DC-DC LVDT, Model 243), a voice coil motor (H2W technologies, NCM-05-08-0052JBT), a force sensor (Honeywell Model 31), and a 14 mm flat indenter tip (Figure 6-14). The displacement sensor has a working range of 12 mm and the force sensor can measure loads up to 20 N. These components allow for testing of the cell cultures at rates between 0.01 and 50 Hz at depths resulting in 15-50 % strain. The entire device can fit into a laminar flow hood (Figure 6-15 A) to minimize risks of contamination and the tip that actually comes in contact with the cell cultures can easily be sterilized with ethanol. The 14 mm indenter was designed to fit inside the wells of a 24 well plate, enabling fluid to escape along the sides while still compressing the majority of the cell construct (Figure 6-15 B).

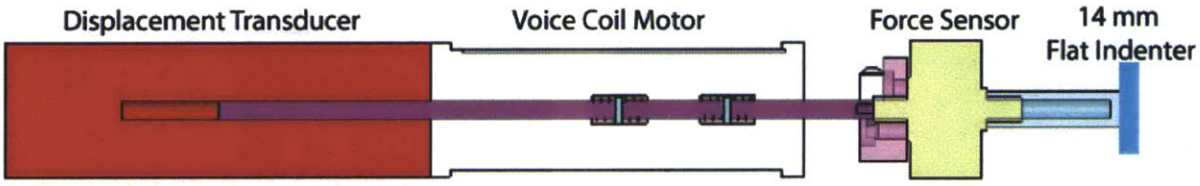

Figure 6-14: Schematic of the key components of the custom voice coil device used to compress cell cultures.

Both the load cell and the LVDT were calibrated. The load cell was calibrated with known masses in both tension and compression. It was found to be linear for loads between 50 mN and 1N. In addition, calibration in both tension and compression was consistent. Force and displacement measurements for 6 different wells containing collagen gels showed that the device produced a consistent compression of the cultures at both 1 and 10 Hz as shown in Figure 6-16.

In addition, reproducible results were obtained for both multi-cyclic loading and for single cycles. Finally, the reproducible force curves validate the positioning methods for consistently placing the indenter above the collagen gels upon changing between wells of a culture plate, ensuring that cell cultures could be reproducibly damaged using this system.

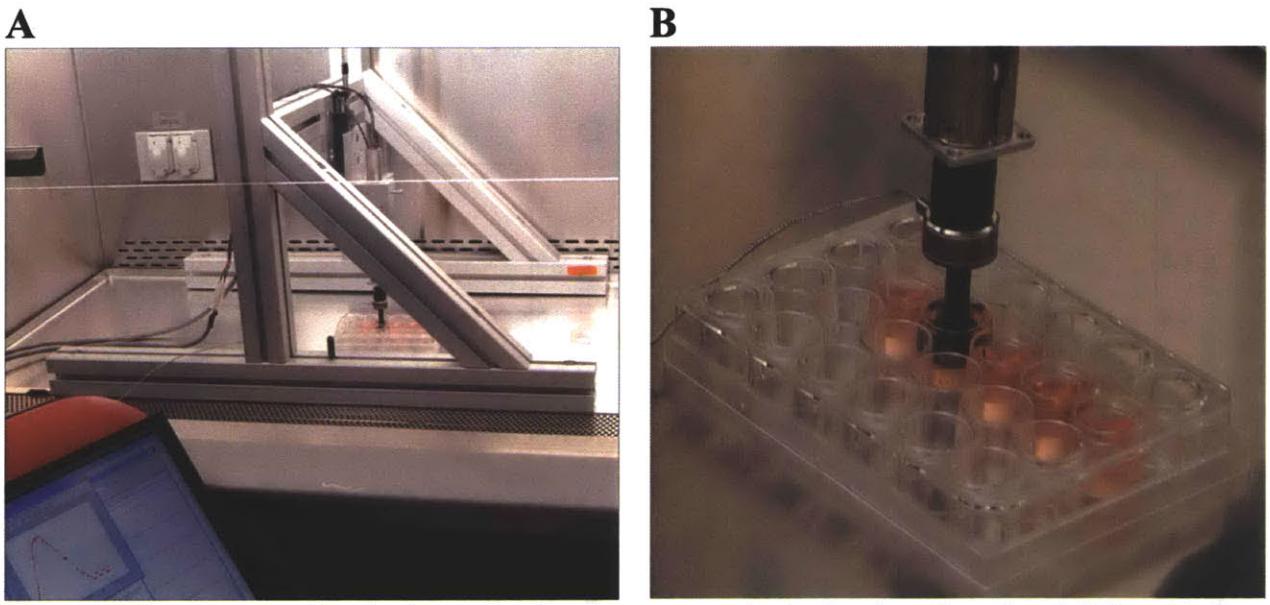

Figure 6-15: Compression device and cell culture set up in the laminar floor hood (A) and being used to compress cell cultures in a 24 well plate (B).

In order to verify that the device did not cause complete cell death or any contamination problems, pure neuronal cultures were compressed one time each at 0.1 Hz and 1 Hz to a depth yielding approximately 20 % strain. Control samples were left out of the incubator during the tests to control for any damage due to being at room temperature for the duration of the compression experiment. No contamination was observed after 48 h, at which time a viability assay was performed using Calcein-AM to identify live cells and ethidium homodimer 1 to label dead cell nuclei. Epi-fluorescence images were taken at 3-4 locations per gel. Cell counts suggested a trend of increasing cell death with rate of compression as shown in Figure 6-17.

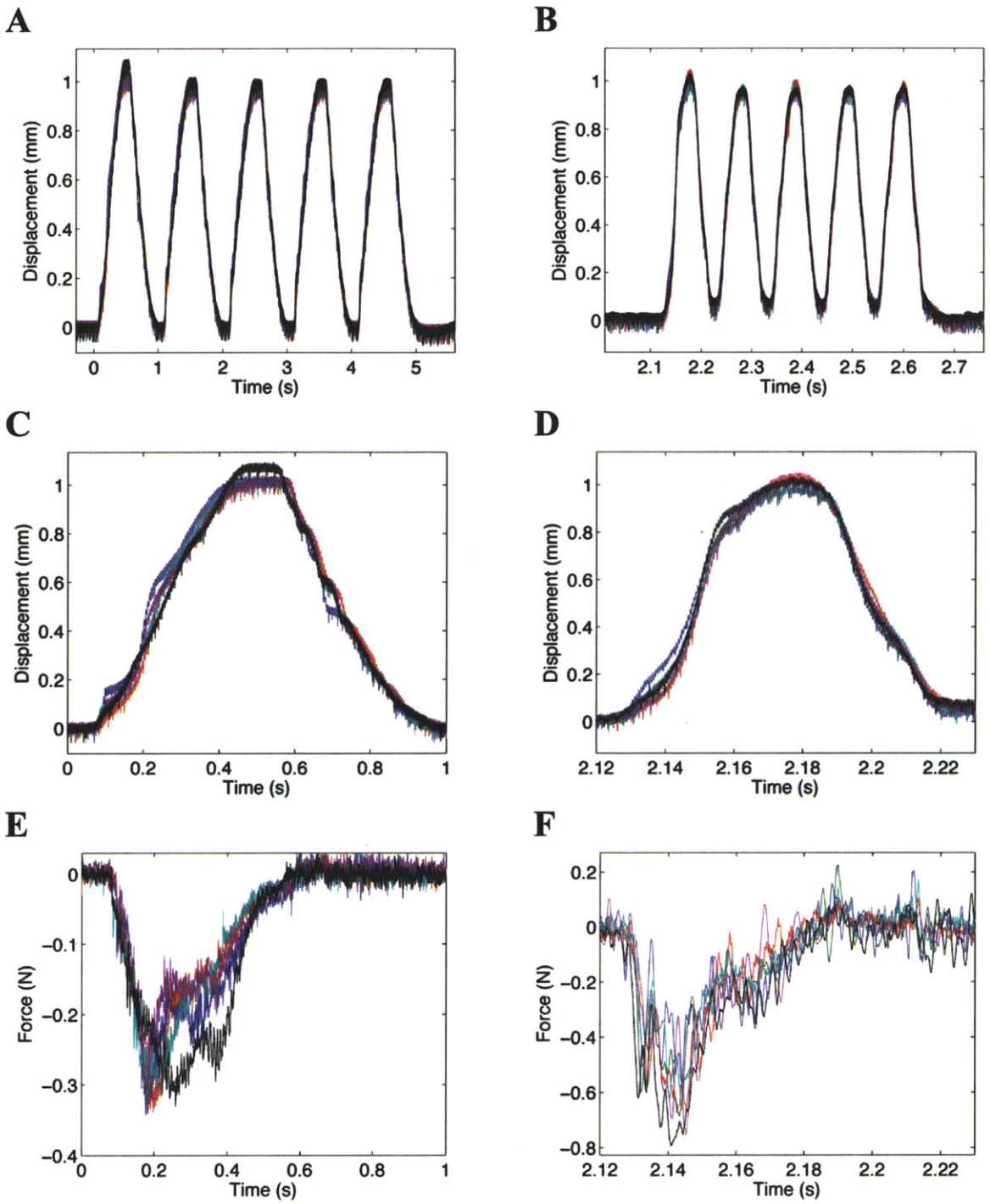

Figure 6-16: Reproducible displacement and force profiles obtained for compressive loading of collagen gels at 1 Hz (A, C, E) and 10 Hz (B, D, F) for 6 wells tested at each rate.

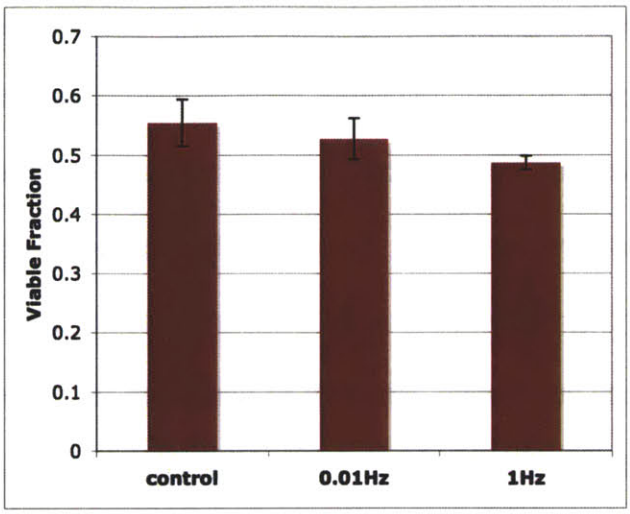

Figure 6-17: Percent viability for control neuron samples as well as those compressed once at 0.01 Hz and 1 Hz. Data taken from counts of live and dead cells in representative images taken throughout the collagen gel constructs.

In order to further investigate the compression system, the above experiment was repeated at faster loading rates and with viability images analyzed with confocal microscopy. Use of confocal microscopy enabled better visualization of the distribution of cell viability throughout the depth of the cultures. In this experiment, cultures containing either pure neurons or both neurons and glia were compressed one time each at either 1 Hz or 10 Hz to a depth of 1 mm (~20% strain). An additional control was added in which some wells were loaded onto the device and the tip was brought into contact with the gel surface, but no compression occurred. As before, the other control wells were left out of the incubator and in the laminar flow hood for the duration of the experiment. Results of viability assays performed with confocal imaging showed the cell viability patterns remained consistent throughout the depth of the gels for both pure neuronal cultures at 1 Hz (Figure 6-18 A), 10 Hz (Figure 6-18 B), control with no contact (Figure 6-18 C), and control with contact (Figure 6-18 D). The same was true for cultures containing both neurons and glia at 1 Hz (Figure 6-19 A), 10 Hz (Figure 6-19 B), control with no contact (Figure 6-19 C), and control with contact (Figure 6-19 D). However, there was observed

variation between different regions of the gels in both the controls and experimental wells. In addition, due to clumping of cells, obtaining accurate counts of live cells proved difficult. Despite these limitations, the results show that a percentage of cells in both pure neuronal cultures and in co-cultures remain viable throughout the depth of the gel, making this an ideal damage system for studying what unfolds at the cellular level after mild TBI.

To further validate this system, tests will be done with the lab of Dr. Michael Whalen at Massachusetts General Hospital as described for the blast system. This will enable comparison to animal models of contusion and concussion, which may be especially relevant to damage caused by compression at the cell level. In addition, due to utilizing the same cell culture system, results can be compared to the blast studies to investigate mechanisms of damage from two different types of loading.

6.5 Summary

In this chapter, two new devices for generating mild TBI at the cellular level were described. Both devices were shown to produce consistent loading profiles and the typical loads were fully characterized. In addition, both the compression and shockwave devices were compatible with cells cultured in collagen gels and the collagen gel culture systems were shown to yield viable cells throughout the depth of the seeded portion of the gels. The damage systems were also shown to not cause complete cell death after 48 h, making them ideal systems to study mild TBI and the events that unfold in the hours to days after trauma that cause the pathopysiological response characteristic of TBI but do not result in immediate cell death. Finally, these systems offer great flexibility in experimental design, allowing for testing different loading conditions (for example: number and magnitude of insult) as well as the response of different types of cells.

These devices serve as valuable new tools in the study of TBI at the cellular level, and coupled with the work done in collaboration with Dr. Michael Whalen, will increase the knowledge of events occurring at the cellular level after injury.

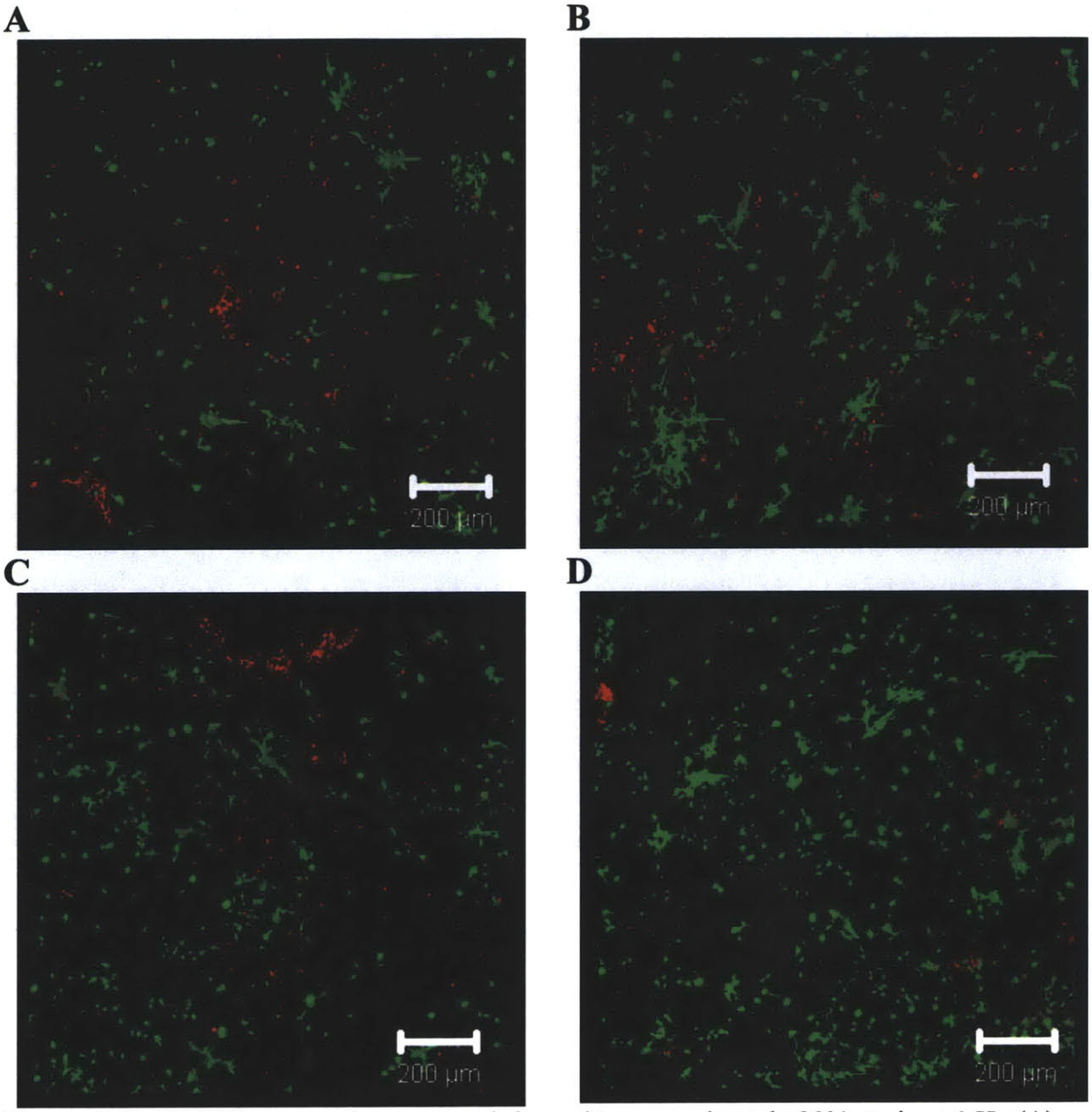

Figure 6-18: Viability assays for neurons deformed to approximately 20% strain at 1 Hz (A) and 10 Hz (B), and for control with no contact (C), and control with contact with gel (D). Live cells labeled with Calcein-AM (Green) and dead nuclei with Ethidium Homodimer 1 (Red).

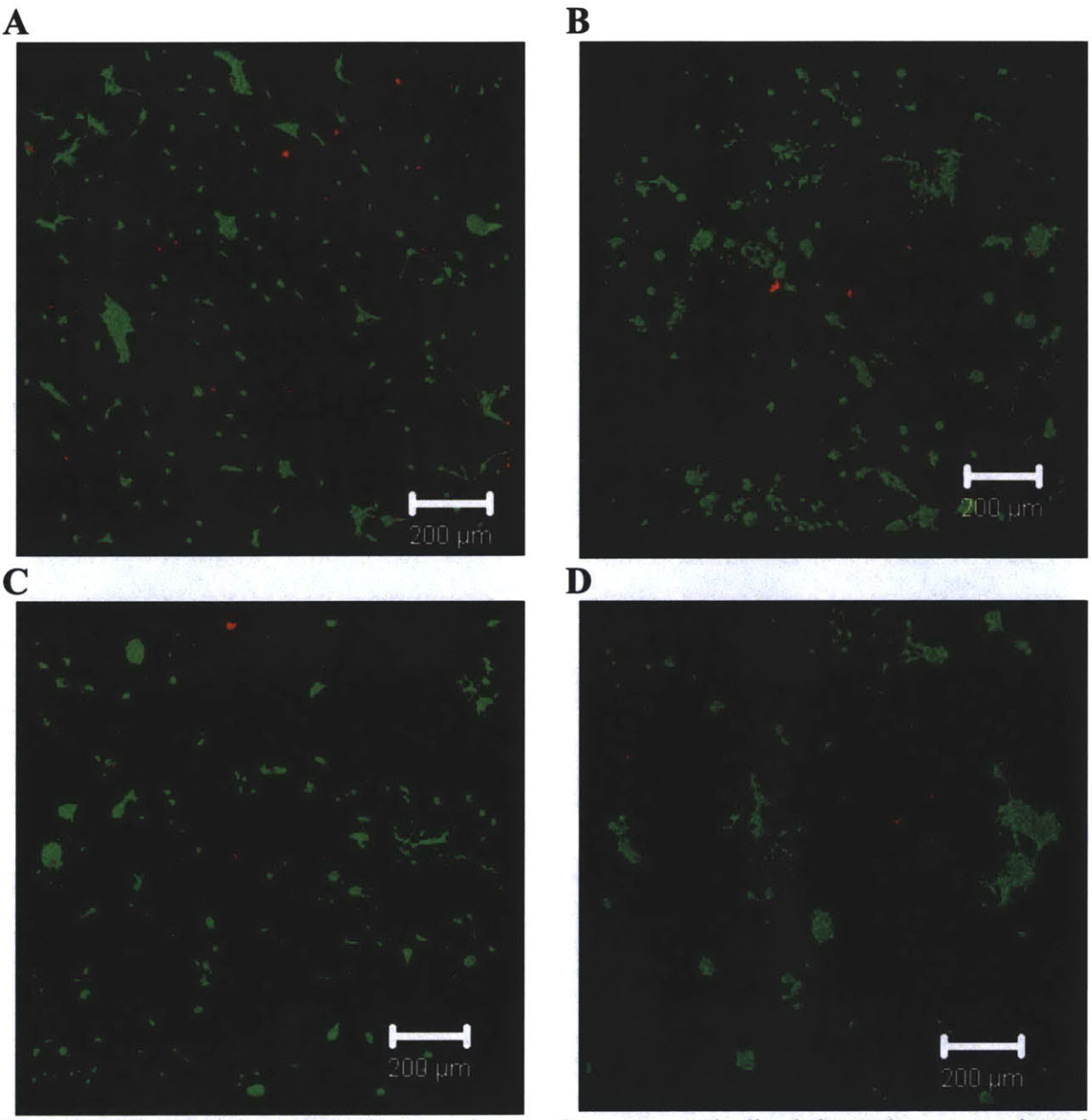

Figure 6-19: Viability assays for co-cultures of neurons and glia deformed to approximately 20% strain at 1 Hz (A) and 10 Hz (B), and for control with no contact (C), and control with contact with gel (D). Live cells labeled with Calcein-AM (Green) and dead nuclei with Ethidium Homodimer 1 (Red).

Chapter 7

Conclusions and Thesis Contributions

This thesis characterizes the biomechanics of cells of the central nervous system and provides important new tools, both experimental and computational for the quantitative study of traumatic brain injury *in vitro* at the cellular level. It fills in major knowledge gaps and advances the field as outlined below:

- Atomic force microscopy methods were developed to measure the global cell response of both neurons and astrocytes at loading rates spanning 3 orders of magnitude and under stress relaxation.

- Single cell finite element models with a rheological material model were developed to capture the response at three different loading rates as well as during a stress relaxation test, providing novel single cell models of both neurons and astrocytes capable of capturing all aspects of the measured force response with a single set of parameters.

- The AFM experimental methods and computational analysis showed astrocytes to be more elastic than neurons, as indicated both by the AFM force response and the material parameters obtained from the calibrated constitutive model. To our knowledge, this finding has not been reported previously.

- The importance of substrate on the cell response was quantified, showing neuron response to be relatively insensitive to changes in substrate stiffness whereas astrocyte response could be classified in to two major groups, characterized by round versus spread morphology and lower force levels reached during AFM indentation for rounded cells. Use of finite element modeling and the developed constitutive model showed changes in cell morphology to account for the bulk of the observed changes in force response, with the material parameters remaining fairly consistent. This highlights the importance of designing *in vitro* studies of TBI to have the cells growing in a realistic mechanical environment, to ensure both morphology and force response are realistic.

- Systems to damage cells with both compressive loading and shock waves in 3D collagen gels were developed and characterized, providing new tools for investigating TBI at the cellular level and in a realistic 3D environment with properties similar to that of soft brain tissue. These tools are especially useful for the study of mild TBI, as shown by the cells remaining viable for at least 48 hours after testing. The developed cell damage systems are currently being tested to see if key signaling molecules identified in rat models of TBI are also up-regulated in the cell cultures (in collaboration with the lab of Dr. Michael Whalen at Massachusetts General Hospital).

References

[1] Taber K.H., Warden D.L., Hurley R.A. Blast-Related Traumatic Brain Injury: What Is Known? J Neuropsychiatry Clin Neurosci 2006;18:141.

[2] Cernak I., Noble-Haeusslein L.J. Traumatic Brain Injury: An Overview of Pathobiology with Emphasis on Military Populations. Journal of Cerebral Blood Flow & Metabolism 2009;30:255.

[3] Park E., Bell J.D., Baker A.J. Traumatic Brain Injury: Can the Consequences Be Stopped? Canadian Medical Association Journal 2008;178:1163.

[4] Kearney C.J. Non-Invasive Shock Wave Stimulated Periosteum for Bone Tissue Engineering. Health Sciences and Technology, vol. Ph.D. Cambridge: Massachusetts Institute of Technology, 2011. p.225.

[5] Virchow R. Gesammelte Abhandlungen Zur Wissenschaftlichen Medicin: Meidinger, 1856.

[6] Sofroniew M.V. Reactive Astrocytes in Neural Repair and Protection. The Neuroscientist 2005;11:400.

[7] Miller W.J., Leventhal I., Scarsella D., Haydon P.G., Janmey P., Meaney D.F. Mechanically Induced Reactive Gliosis Causes ATP-Mediated Alterations in Astrocyte Stiffness. Journal of Neurotrauma 2009;26:789.

[8] Reichenbach A., Pannicke T. Neuroscience. A New Glance at Glia. Science (New York, NY) 2008;322:693.

[9] Fiacco T.A., Mccarthy K.D. Intracellular Astrocyte Calcium Waves in Situ Increase the Frequency of Spontaneous AMPA Receptor Currents in Ca1 Pyramidal Neurons. Journal of Neuroscience 2004;24:722.

[10] Perea G., Navarrete M., Araque A. Tripartite Synapses: Astrocytes Process and Control Synaptic Information. Trends in neurosciences 2009;32:421.

[11] Volterra A., Meldolesi J. Astrocytes, from Brain Glue to Communication Elements: The Revolution Continues. Nature Reviews Neuroscience 2005;6:626.

[12] Faul M., Xu L., Wald M., Coronado V. Traumatic Brain Injury in the United States: Emergency Department Visits, Hospitalizations and Deaths 2002-2006, Centers for Disease Control and Prevention. National Center for Injury Prevention and Control, Atlanta (GA) 2010.

[13] Kraus J.F., Mcarthur D.L. Epidemiologic Aspects of Brain Injury. Neurologic Clinics 1996;14:435.

[14] Tanielian T., Jaycox L.H. Invisible Wounds of War: Psychological and Cognitive Injuries, Their Consequences,and Services to Assist Recovery. Santa Monica, CA: RAND Corporation, 2008.

[15] Hoge C.W., Goldberg H.M., Castro C.A. Care of War Veterans with Mild Traumatic Brain Injury - Flawed Perspectives. New England Journal of Medicine 2009;360:1588.

[16] Chen Y.C., Smith D.H., Meaney D.F. In-Vitro Approaches for Studying Blast-Induced Traumatic Brain Injury. Journal of Neurotrauma 2009;26:861.

[17] Hoge C.W., Mcgurk D., Thomas J.L., Cox A.L., Engel C.C., Castro C.A. Mild Traumatic Brain Injury in US Soldiers Returning from Iraq. New England Journal of Medicine 2008.

[18] Schwab K., Baker G., Ivins B., Sluss-Tiller M., Lux W., Warden D. The Brief Traumatic Brain Injury Screen (Btbis): Investigating the Validity of a Self-Report Instrument for Detecting Traumatic Brain Injury (TBI) in Troops Returning from Deployment in Afghanistan and Iraq. Neurology 2006;66:A235.

[19] Axelsson H., Hjelmqvist H., Medin A., Persson J., Suneson A. Physiological Changes in Pigs Exposed to a Blast Wave from a Detonating High-Explosive Charge. Military medicine 2000;165:119.

[20] Moochhala S.M., Md S., Lu J., Teng C.H., Greengrass C. Neuroprotective Role of Aminoguanidine in Behavioral Changes after Blast Injury. The Journal of Trauma 2004;56:393.

[21] Kaur C., Singh J., Lim M., Ng B., Yap E., Ling E. The Response of Neurons and Microglia to Blast Injury in the Rat Brain. Neuropathology and applied neurobiology 1995;21:369.

[22] Wang Z., Sun L., Yang Z., Leng H., Jiang J., Yu H., Gu J., Li Z. Development of Serial Bio-Shock Tubes and Their Application. Chinese medical journal 1998;111:109.

[23] Cernak I., Wang Z., Jiang J., Bian X., Savic J. Ultrastructural and Functional Characteristics of Blast Injury-Induced Neurotrauma. The Journal of Trauma 2001;50:695.

[24] Saljo A., Bao F., Haglid K.G., Hansson H.A. Blast Exposure Causes Redistribution of Phosphorylated Neurofilament Subunits in Neurons of the Adult Rat Brain. Journal of Neurotrauma 2000;17:719.

[25] Kaur C., Singh J., Lim M., Ng B., Ling E. Macrophages/Microglia as Sensors of Injury in the Pineal Gland of Rats Following a Non-Penetrative Blast. Neuroscience research 1997;27:317.

[26] Kaur C., Singh J., Lim M., Ng B., Yap E., Ling E. Studies of the Choroid Plexus and Its Associated Epiplexus Cells in the Lateral Ventricles of Rats Following an Exposure to a Single Non-Penetrative Blast. Archives of histology and cytology 1996;59:239.

[27] Park E., Gottlieb J.J., Cheung B., Shek P.N., Baker A.J. A Model of Low-Level Primary Blast Exposure Results in Cytoskeletal Proteolysis and Chronic Functional Impairment in the Brain in the Absence of Lung Barotrauma. Journal of Neurotrauma 2010.

[28] Saljo A., Mayorga M., Bolouri H., Svensson B., Hamberger A. Mechanisms and Pathophysiology of the Low-Level Blast Brain Injury in Animal Models. Neuroimage 2010.

[29] Kato K., Fujimura M., Nakagawa A., Saito A., Ohki T., Takayama K., Tominaga T. Pressure-Dependent Effect of Shock Waves on Rat Brain: Induction of Neuronal Apoptosis Mediated by a Caspase-Dependent Pathway. Journal of neurosurgery 2007;106:667.

[30] Vanderploeg R.D., Curtiss G., Luis C.A., Salazar A.M. Long-Term Morbidities Following Self-Reported Mild Traumatic Brain Injury. Journal of Clinical and Experimental Neuropsychology 2007;29:585.

[31] Corrigan J.D., Selassie A.W., Orman J.A.L. The Epidemiology of Traumatic Brain Injury. J Head Trauma Rehabil 2010;25:72.

[32] Belanger H.G., Kretzmer T., Yoash-Gantz R., Pickett T., Tupler L.A. Cognitive Sequelae of Blast-Related Versus Other Mechanisms of Brain Trauma. J. Int. Neuropsychol. Soc. 2009;15:1.

[33] Mccrory P., Makdissi M., Davis G., Collie A. Value of Neuropsychological Testing after Head Injuries in Football. British Journal of Sports Medicine 2005;39:I58.

[34] Meehan W.P., Bachur R.G. Sport-Related Concussion. Pediatrics 2009;123:114.

[35] Crowe L.M., Anderson V., Catroppa C., Babl F.E. Head Injuries Related to Sports and Recreation Activities in School-Age Children and Adolescents: Data from a Referral Centre in Victoria, Australia. Emergency Medicine Australasia 2010;22:56.

[36] Yilmaz S., Pekdemir M. An Unusual Primary Blast Injury - Traumatic Brain Injury Due to Primary Blast Injury. American Journal of Emergency Medicine 2007;25:97.

[37] Lew H.L., Poole J.H., Alvarez S., Moore W. Soldiers with Occult Traumatic Brain Injury. American Journal of Physical Medicine & Rehabilitation 2005;84:393.

[38] Whalen M.J., Dalkara T., You Z., Qiu J., Bermpohl D., Mehta N., Suter B., Bhide P.G., Lo E.H., Ericsson M. Acute Plasmalemma Permeability and Protracted Clearance of Injured Cells after Controlled Cortical Impact in Mice. Journal of Cerebral Blood Flow & Metabolism 2007;28:490.

[39] Farkas O., Lifshitz J., Povlishock J.T. Mechanoporation Induced by Diffuse Traumatic Brain Injury: An Irreversible or Reversible Response to Injury? Journal of Neuroscience 2006;26:3130.

[40] Singleton R.H., Povlishock J.T. Identification and Characterization of Heterogeneous Neuronal Injury and Death in Regions of Diffuse Brain Injury: Evidence for Multiple Independent Injury Phenotypes. Journal of Neuroscience 2004;24:3543.

[41] Raghupathi R. Cell Death Mechanisms Following Traumatic Brain Injury. Brain Pathology 2004;14:215.

[42] Gaetz M. The Neurophysiology of Brain Injury. Clinical Neurophysiology 2004;115:4.

[43] Whalen M.J., Yager P., Lo E.H., Lok J., Noviski N. Molecular Biology of Brain Injury. The Central Nervous System in Pediatric Critical Illness and Injury 2009:1.

[44] Svetlov S.I., Larner S.F., Kirk D.R., Atkinson J., Hayes R.L., Wang K.K.W. Biomarkers of Blast-Induced Neurotrauma: Profiling Molecular and Cellular Mechanisms of Blast Brain Injury. Journal of Neurotrauma 2009;26:913.

[45] Griffiths M., Gasque P., Neal J. The Regulation of the CNS Innate Immune Response Is Vital for the Restoration of Tissue Homeostasis (Repair) after Acute Brain Injury: A Brief Review. International Journal of Inflammation 2010.

[46] Mcgraw J., Hiebert G., Steeves J. Modulating Astrogliosis after Neurotrauma. Journal of neuroscience research 2001;63:109.

[47] Pettus E.H., Christman C.W., Giebel M.L., Povlishock J.T. Traumatically Induced Altered Membrane Permeability: Its Relationship to Traumatically Induced Reactive Axonal Change. Journal of Neurotrauma 1994;11:507.

[48] Pettus E.H., Povlishock J.T. Characterization of a Distinct Set of Intra-Axonal Ultrastructural Changes Associated with Traumatically Induced Alteration in Axolemmal Permeability. Brain research 1996;722:1.

[49] Laplaca M.C., Prado G.R. Neural Mechanobiology and Neuronal Vulnerability to Traumatic Loading. Journal of Biomechanics 2010;43:71.

[50] Shi R., Whitebone J. Conduction Deficits and Membrane Disruption of Spinal Cord Axons as a Function of Magnitude and Rate of Strain. Journal of neurophysiology 2006;95:3384.

[51] Laplaca M., Simon C., Prado G., Cullen D. Cns Injury Biomechanics and Experimental Models. Progress in Brain Research 2007;161:13.

[52] Geddes D.M., Cargill R.S., Laplaca M.C. Mechanical Stretch to Neurons Results in a Strain Rate and Magnitude-Dependent Increase in Plasma Membrane Permeability. Journal of Neurotrauma 2003;20:1039.

[53] Kilinc D., Gallo G., Barbee K.A. Mechanically-Induced Membrane Poration Causes Axonal Beading and Localized Cytoskeletal Damage. Experimental neurology 2008;212:422.

[54] Kilinc D., Gallo G., Barbee K.A. Mechanical Membrane Injury Induces Axonal Beading through Localized Activation of Calpain. Experimental neurology 2009;219:553.

[55] Yi J.H., Hazell A.S. Excitotoxic Mechanisms and the Role of Astrocytic Glutamate Transporters in Traumatic Brain Injury. Neurochemistry international 2006;48:394.

[56] Spaethling J.M., Geddes-Klein D.M., Miller W.J., Von Reyn C.R., Singh P., Mesfin M., Bernstein S.J., Meaney D.F. Linking Impact to Cellular and Molecular Sequelae of CNS Injury: Modeling in Vivo Complexity with in Vitro Simplicity. Progress in Brain Research 2007;161:27.

[57] Ahmed S.M., Weber J.T., Liang S., Willoughby K.A., Sitterding H.A., Rzigalinski B.A., Ellis E.F. NMDA Receptor Activation Contributes to a Portion of the Decreased Mitochondrial Membrane Potential and Elevated Intracellular Free Calcium in Strain-Injured Neurons. Journal of Neurotrauma 2002;19:1619.

[58] Geddes Klein D.M., Serbest G., Mesfin M.N., Cohen A.S., Meaney D.F. Pharmacologically Induced Calcium Oscillations Protect Neurons from Increases in Cytosolic Calcium after Trauma. Journal of neurochemistry 2006;97:462.

[59] Goforth P.B., Ellis E.F., Satin L.S. Enhancement of Ampa-Mediated Current after Traumatic Injury in Cortical Neurons. Journal of Neuroscience 1999;19:7367.

[60] Goforth P.B., Ellis E.F., Satin L.S. Mechanical Injury Modulates Ampa Receptor Kinetics Via an NMDA Receptor-Dependent Pathway. Journal of Neurotrauma 2004;21:719.

[61] Stellwagen D., Beattie E.C., Seo J.Y., Malenka R.C. Differential Regulation of AMPA Receptor and Gaba Receptor Trafficking by Tumor Necrosis Factor-{Alpha}. Journal of Neuroscience 2005;25:3219.

[62] Isaac J.T.R., Ashby M.C., Mcbain C.J. The Role of the Glur2 Subunit in AMPA Receptor Function and Synaptic Plasticity. Neuron 2007;54:859.

[63] Yuan J., Lipinski M., Degterev A. Diversity in the Mechanisms of Neuronal Cell Death. Neuron 2003;40:401.

[64] Zhang X., Chen Y., Jenkins L.W., Kochanek P.M., Clark R.S.B. Bench-to-Bedside Review: Apoptosis/Programmed Cell Death Triggered by Traumatic Brain Injury. Critical care 2004;9:66.

[65] Thornberry N.A., Lazebnik Y. Caspases: Enemies Within. Science 1998;281:1312.

[66] Yakovlev A.G., Knoblach S.M., Fan L., Fox G.B., Goodnight R., Faden A.I. Activation of Cpp32-Like Caspases Contributes to Neuronal Apoptosis and Neurological Dysfunction after Traumatic Brain Injury. The Journal of neuroscience 1997;17:7415.

[67] Bermpohl D., You Z., Lo E.H., Kim H.H., Whalen M.J. TNF Alpha and Fas Mediate Tissue Damage and Functional Outcome after Traumatic Brain Injury in Mice. Journal of Cerebral Blood Flow & Metabolism 2007;27:1806.

[68] Berghe T.V., Van Loo G., Saelens X., Van Gurp M., Brouckaert G., Kalai M., Declercq W., Vandenabeele P. Differential Signaling to Apoptotic and Necrotic Cell Death by Fas-Associated Death Domain Protein Fadd. Journal of Biological Chemistry 2004;279:7925.

[69] Hanisch U.K., Kettenmann H. Microglia: Active Sensor and Versatile Effector Cells in the Normal and Pathologic Brain. Nature neuroscience 2007;10:1387.

[70] Kang S.H., Fukaya M., Yang J.K., Rothstein J.D., Bergles D.E. NG2+ CNS Glial Progenitors Remain Committed to the Oligodendrocyte Lineage in Postnatal Life and Following Neurodegeneration. Neuron 2010;68:668.

[71] Robel S., Berninger B., Gotz M. The Stem Cell Potential of Glia: Lessons from Reactive Gliosis. Nature Reviews Neuroscience 2011;12:88.

[72] Pekny M., Nilsson M. Astrocyte Activation and Reactive Gliosis. Glia 2005;50:427.

[73] Lu Y.B., Iandiev I., Hollborn M., Korber N., Ulbricht E., Hirrlinger P.G., Pannicke T., Wei E.Q., Bringmann A., Wolburg H. Reactive Glial Cells: Increased Stiffness Correlates with Increased Intermediate Filament Expression. The FASEB Journal 2010;25:624.

[74] Bush T.G., Puvanachandra N., Horner C.H., Polito A., Ostenfeld T., Svendsen C.N., Mucke L., Johnson M.H., Sofroniew M.V. Leukocyte Infiltration, Neuronal Degeneration, and Neurite Outgrowth after Ablation of Scar-Forming, Reactive Astrocytes in Adult Transgenic Mice. Neuron 1999;23:297.

[75] Mckeon R.J., H^ke A., Silver J. Injury-Induced Proteoglycans Inhibit the Potential for Laminin-Mediated Axon Growth on Astrocytic Scars. Experimental neurology 1995;136:32.

[76] Bernick K.B., Prevost T.P., Suresh S., Socrate S. Biomechanics of Single Cortical Neurons. Acta Biomaterialia 2011;7:1210.

[77] Bao G., Suresh S. Cell and Molecular Mechanics of Biological Materials. Nature Materials 2003;2:715.

[78] Van Vliet K., Bao G., Suresh S. The Biomechanics Toolbox: Experimental Approaches for Living Cells and Biomolecules. Acta Materialia 2003;51:5881.

[79] Suresh S. Biomechanics and Biophysics of Cancer Cells. Acta Biomaterialia 2007;3:413.

[80] Wang N., Butler J.P., Ingber D.E. Mechanotransduction across the Cell-Surface and through the Cytoskeleton. Science 1993;260:1124.

[81] Trepat X., Grabulosa M., Puig F., Maksym G.N., Navajas D., Farre R. Viscoelasticity of Human Alveolar Epithelial Cells Subjected to Stretch. American Journal of Physiology-Lung Cellular and Molecular Physiology 2004;287:L1025.

[82] Tagawa H., Wang N., Narishige T., Ingber D.E., Zile M.R., Cooper G. Cytoskeletal Mechanics in Pressure-Overload Cardiac Hypertrophy. Circulation Research 1997;80:281.

[83] Massiera G., Van Citters K.M., Biancaniello P.L., Crocker J.C. Mechanics of Single Cells: Rheology, Time Depndence, and Fluctuations. Biophysical Journal 2007;93:3703.

[84] Yamada S., Wirtz D., Kuo S.C. Mechanics of Living Cells Measured by Laser Tracking Microrheology. Biophysical Journal 2000;78:1736.

[85] Tseng Y., Kole T.P., Wirtz D. Micromechanical Mapping of Live Cells by Multiple-Particle-Tracking Microrheology. Biophysical Journal 2002;83:3162.

[86] Jonas M., Huang H., Kamm R.D., So P.T.C. Fast Fluorescence Laser Tracking Microrheometry, Ii: Quantitative Studies of Cytoskeletal Mechanotransduction. Biophysical Journal 2008;95:895.

[87] Mahaffy R.E., Park S., Gerde E., Kas J., Shih C.K. Quantitative Analysis of the Viscoelastic Properties of Thin Regions of Fibroblasts Using Atomic Force Microscopy. Biophysical Journal 2004;86:1777.

[88] Darling E.M., Zauscher S., Guilak F. Viscoelastic Properties of Zonal Articular Chondrocytes Measured by Atomic Force Microscopy. Osteoarthritis and Cartilage 2006;14:571.

[89] Radmacher M., Fritz M., Kacher C.M., Cleveland J.P., Hansma P.K. Measuring the Viscoelastic Properties of Human Platelets with the Atomic Force Microscope. Biophysical Journal 1996;70:556.

[90] Mathur A.B., Collinsworth A.M., Reichert W.M., Kraus W.E., Truskey G.A. Endothelial, Cardiac Muscle and Skeletal Muscle Exhibit Different Viscous and Elastic Properties as Determined by Atomic Force Microscopy. Journal of Biomechanics 2001;34:1545.

[91] Lam W., Rosenbluth M., Fletcher D. Chemotherapy Exposure Increases Leukemia Cell Stiffness. Blood 2007;109:3505.

[92] Lulevich V., Zink T., Chen H.Y., Liu F.T., Liu G.Y. Cell Mechanics Using Atomic Force Microscopy-Based Single-Cell Compression. Langmuir 2006;22:8151.

[93] Evans E., Kukan B. Passive Material Behavior of Granulocytes Based on Large Deformation and Recovery after Deformation Tests. Blood 1984;64:1028.

[94] Merryman W.D., Youn I., Lukoff H.D., Krueger P.M., Guilak F., Hopkins R.A., Sacks M.S. Correlation between Heart Valve Interstitial Cell Stiffness and Transvalvular Pressure: Implications for Collagen Biosynthesis. American Journal of Physiology-Heart and Circulatory Physiology 2006;290:H224.

[95] Rand R.P., Burton A.C. Mechanical Properties of Red Cell Membrane .I. Membrane Stiffness + Intracellular Pressure. Biophysical Journal 1964;4:115.

[96] Schmidschonbein G.W., Sung K.L.P., Tozeren H., Skalak R., Chien S. Passive Mechanical-Properties of Human-Leukocytes. Biophysical Journal 1981;36:243.

[97] Sato M., Theret D.P., Wheeler L.T., Ohshima N., Nerem R.M. Application of the Micropipette Technique to the Measurement of Cultured Porcine Aortic Endothelial-Cell Viscoelastic Properties. Journal of Biomechanical Engineering-Transactions of the Asme 1990;112:263.

[98] Trickey W.R., Vail T.P., Guilak F. The Role of the Cytoskeleton in the Viscoelastic Properties of Human Articular Chondrocytes. Journal of Orthopaedic Research 2004;22:131.

[99] Henon S., Lenormand G., Richert A., Gallet F. A New Determination of the Shear Modulus of the Human Erythrocyte Membrane Using Optical Tweezers. Biophysical Journal 1999;76:1145.

[100] Mills J.P., Diez-Silva M., Quinn D.J., Dao M., Lang M.J., Tan K.S.W., Lim C.T., Milon G., David P.H., Mercereau-Puijalon O., Bonnefoy S., Suresh S. Effect of Plasmodial Resa Protein on Deformability of Human Red Blood Cells Harboring Plasmodium Falciparum. Proceedings of the National Academy of Sciences of the United States of America 2007;104:9213.

[101] Guck J., Ananthakrishnan R., Mahmood H., Moon T.J., Cunningham C.C., Kas J. The Optical Stretcher: A Novel Laser Tool to Micromanipulate Cells. Biophysical Journal 2001;81:767.

[102] Lu Y.B., Franze K., Seifert G., Steinhauser C., Kirchhoff F., Wolburg H., Guck J., Janmey P., Wei E.Q., Kas J., Reichenbach A. Viscoelastic Properties of Individual Glial Cells and Neurons in the Cns. Proceedings of the National Academy of Sciences of the United States of America 2006;103:17759.

[103] Desprat N., Richert A., Simeon J., Asnacios A. Creep Function of a Single Living Cell. Biophysical Journal 2005;88:2224.

[104] Fernandez P., Pullarkat P.A., Ott A. A Master Relation Defines the Nonlinear Viscoelasticity of Single Fibroblasts. Biophysical Journal 2006;90:3796.

[105] Suresh S., Spatz J., Mills J.P., Micoulet A., Dao M., Lim C.T., Beil M., Seufferlein T. Connections between Single-Cell Biomechanics and Human Disease States: Gastrointestinal Cancer and Malaria. Acta Biomaterialia 2005;1:15.

[106] Binnig G., Quate C.F., Gerber C. Atomic Force Microscope. Phys Rev Lett 1986;56:930.

[107] Franz C.M., Puech P.H. Atomic Force Microscopy: A Versatile Tool for Studying Cell Morphology, Adhesion and Mechanics. Cellular and Molecular Bioengineering 2008;1:289.

[108] Margulies S.S., Thibault L.E., Gennarelli T.A. Physical Model Simulations of Brain Injury in the Primate. Journal of Biomechanics 1990;23:823.

[109] Bain A.C., Meaney D.F. Tissue-Level Thresholds for Axonal Damage in an Experimental Model of Central Nervous System White Matter Injury. Journal of Biomechanical Engineering-Transactions of the Asme 2000;122:615.

[110] Zhang L.Y., Yang K.H., King A.I. A Proposed Injury Threshold for Mild Traumatic Brain Injury. Journal of Biomechanical Engineering - Transactions of the Asme 2004;126:226.

[111] Galbraith J.A., Thibault L.E., Matteson D.R. Mechanical and Electrical Responses of the Squid Giant-Axon to Simple Elongation. Journal of Biomechanical Engineering-Transactions of the Asme 1993;115:13.

[112] Shiga H., Yamane Y., Ito E., Abe K., Kawabata K., Haga H. Mechanical Properties of Membrane Surface of Cultured Astrocyte Revealed by Atomic Force Microscopy. Jpn J Appl Phys 2000;39:3711.

[113] Vergara D., Martignago R., Leporatti S., Bonsegna S., Maruccio G., Nuccio F.D., Santino A., Cingolani R., Nicolardi G., Maffia M. Biomechanical and Proteomic Analysis of Inf- -Treated Astrocytes. Nanotechnology 2009;20:455106.

[114] Pelham R.J., Wang Y.-L. Cell Locomotion and Focal Adhesions Are Regulated by Substrate Flexibility. Proceedings of the National Academy of Sciences of the United States of America 1997;94:13661.

[115] Bischofs I.B., Schwarz U.S. Cell Organization in Soft Media Due to Active Mechanosensing. Proceedings of the National Academy of Sciences of the United States of America 2003;100:9274.

[116] Janmey P.A., Weitz D.A. Dealing with Mechanics: Mechanisms of Force Transduction in Cells. Trends in Biochemical Sciences 2004;29:364.

[117] Discher D.E., Janmey P., Wang Y.-L. Tissue Cells Feel and Respond to the Stiffness of Their Substrate. Science 2005;310:1139.

[118] Pedersen J., Swartz M. Mechanobiology in the Third Dimension. Annals of Biomedical Engineering 2005;33:1469.

[119] Yeung T., Georges P.C., Flanagan L.A., Marg B., Ortiz M., Funaki M., Zahir N., Ming W., Weaver V., Janmey P.A. Effects of Substrate Stiffness on Cell Morphology, Cytoskeletal Structure, and Adhesion. Cell Motility and the Cytoskeleton 2005;60:24.

[120] Lo C.M., Wang H.B., Dembo M., Wang Y. Cell Movement Is Guided by the Rigidity of the Substrate. Biophysical Journal 2000;79:144.

[121] Levental I., Georges P.C., Janmey P.A. Soft Biological Materials and Their Impact on Cell Function. Soft Matter 2007;3:299.

[122] Georges P.C., Miller W.J., Meaney D.F., Sawyer E.S., Janmey P.A. Matrices with Compliance Comparable to That of Brain Tissue Select Neuronal over Glial Growth in Mixed Cortical Cultures. Biophysical Journal 2006;90:3012.

[123] Moshayedi P., Costa L.D.F., Christ A., Lacour S.P., Fawcett J., Guck J., Franze K. Mechanosensitivity of Astrocytes on Optimized Polyacrylamide Gels Analyzed by Quantitative Morphometry. Journal of Physics: Condensed Matter 2010;22:194114.

[124] Georges P.C., Wagner O., Yeung T., Janmey P.A. Biopolymer Networks and Cellular Mechanosensing. Institute for Medicine and Engineering Papers 2004:20.

[125] Flanagan L.A., Ju Y.E., Marg B., Osterfield M., Janmey P.A. Neurite Branching on Deformable Substrates. Neuroreport 2002;13:2411.

[126] Norman L.L., Aranda-Espinoza H. Cortical Neuron Outgrowth Is Insensitive to Substrate Stiffness. Cellular and Molecular Bioengineering 2010:1.

[127] Jiang X., Georges P.C., Li B., Du Y., Kutzing M.K., Previtera M.L., Langrana N.A., Firestein B.L. Cell Growth in Response to Mechanical Stiffness Is Affected by Neuron-Astroglia Interactions. Open Neuroscience Journal 2007;1:7.

[128] Teixeira A.I., Ilkhanizadeh S., Wigenius J.A., Duckworth J.K., Inganas O., Hermanson O. The Promotion of Neuronal Maturation on Soft Substrates. Biomaterials 2009;30:4567.

[129] Saha K., Keung A.J., Irwin E.F., Li Y., Little L., Schaffer D.V., Healy K.E. Substrate Modulus Directs Neural Stem Cell Behavior. Biophysical Journal 2008;95:4426.

[130] Balgude A., Yu X., Szymanski A., Bellamkonda R. Agarose Gel Stiffness Determines Rate of Drg Neurite Extension in 3d Cultures. Biomaterials 2001;22:1077.

[131] Sundararaghavan H.G., Monteiro G.A., Firestein B.L., Shreiber D.I. Neurite Growth in 3D Collagen Gels with Gradients of Mechanical Properties. Biotechnology and Bioengineering 2009;102:632.

[132] Gefen A., Margulies S.S. Are in Vivo and in Situ Brain Tissues Mechanically Similar? Journal of Biomechanics 2004;37:1339.

[133] Li Q.S., Lee G.Y.H., Ong C.N., Lim C.T. Afm Indentation Study of Breast Cancer Cells. Biochemical and Biophysical Research Communications 2008;374:609.

[134] Spagnoli C., Beyder A., Besch S.R., Sachs F. Drift-Free Atomic Force Microscopy Measurements of Cell Height and Mechanical Properties. Review of Scientific Instruments 2007;78.

[135] Radmacher M. Studying the Mechanics of Cellular Processes by Atomic Force Microscopy. Cell Mechanics 2007;83:347.

[136] Costa K.D., Sim A.J., Yin F.C.P. Non-Hertzian Approach to Analyzing Mechanical Properties of Endothelial Cells Probed by Atomic Force Microscopy. Journal of Biomechanical Engineering-Transactions of the Asme 2006;128:176.

[137] Karcher H., Lammerding J., Huang H.D., Lee R.T., Kamm R.D., Kaazempur-Mofrad M.R. A Three-Dimensional Viscoelastic Model for Cell Deformation with Experimental Verification. Biophysical Journal 2003;85:3336.

[138] Unnikrishnan G.U., Unnikirishnan V.U., Reddy J.N. Constitutive Material Modeling of Cell: A Micromechanics Approach. Journal of Biomechanical Engineering-Transactions of the Asme 2007;129:315.

[139] Shin D., Athanasiou K. Cytoindentation for Obtaining Cell Biomechanical Properties. Journal of Orthopaedic Research 1999;17:880.

[140] Guilak F., Mow V.C. The Mechanical Environment of the Chondrocyte: A Biphasic Finite Element Model of Cell-Matrix Interactions in Articular Cartilage. Journal of Biomechanics 2000;33:1663.

[141] Mcgarry J.G., Prendergast P.J. A Three-Dimensional Finite Element Model of an Adherent Eukaryotic Cell. Eur Cell Mater 2004;7:27.

[142] Gardel M.L., Nakamura F., Hartwig J.H., Crocker J.C., Stossel T.P., Weitz D.A. Prestressed F-Actin Networks Cross-Linked by Hinged Filamins Replicate Mechanical Properties of Cells. Proceedings of the National Academy of Sciences of the United States of America 2006;103:1762.

[143] Ellis E., Mckinney J., Willoughby K., Liang S., Povlishock J. A New Model for Rapid Stretch-Induced Injury of Cells in Culture: Characterization of the Model Using Astrocytes. Journal of Neurotrauma 1995;12:325.

[144] Cargill R.S., Thibault L.E. Acute Alterations in [Ca2+] I in Ng108-15 Cells Subjected to High Strain Rate Deformation and Chemical Hypoxia: An in Vitro Model for Neural Trauma. Journal of Neurotrauma 1996;13:395.

[145] Rzigalinski B.A., Liang S., Mckinney J.S., Willoughby K.A., Ellis E.F. Effect of Ca2+ on in Vitro Astrocyte Injury. Journal of neurochemistry 1997;68:289.

[146] Lusardi T.A., Rangan J., Sun D., Smith D.H., Meaney D.F. A Device to Study the Initiation and Propagation of Calcium Transients in Cultured Neurons after Mechanical Stretch. Annals of Biomedical Engineering 2004;32:1546.

[147] Geddes-Klein D.M., Schiffman K.B., Meaney D.F. Mechanisms and Consequences of Neuronal Stretch Injury in Vitro Differ with the Model of Trauma. Journal of Neurotrauma 2006;23:193.

[148] Arundine M., Aarts M., Lau A., Tymianski M. Vulnerability of Central Neurons to Secondary Insults after in Vitro Mechanical Stretch. Journal of Neuroscience 2004;24:8106.

[149] Geddes D.M., Laplaca M.C., Cargill R.S. Susceptibility of Hippocampal Neurons to Mechanically Induced Injury. Experimental neurology 2003;184:420.

[150] Pfister B.J., Weihs T.P., Betenbaugh M., Bao G. An in Vitro Uniaxial Stretch Model for Axonal Injury. Annals of Biomedical Engineering 2003;31:589.

[151] Lucas J.H., Wolf A. In Vitro Studies of Multiple Impact Injury to Mammalian Cns Neurons: Prevention of Perikaryal Damage and Death by Ketamine. Brain research 1991;543:181.

[152] Murphy E.J., Horrocks L.A. A Model for Compression Trauma: Pressure-Induced Injury in Cell Cultures. Journal of Neurotrauma 1993;10:431.

[153] Shepard S.R., Ghajar J.B.G., Giannuzzi R., Kupferman S., Hariri R.J. Fluid Percussion Barotrauma Chamber: A New in Vitro Model for Traumatic Brain Injury. Journal of Surgical Research 1991;51:417.

[154] Laplaca M.C., Lee V.M.Y., Thibault L.E. An in Vitro Model of Traumatic Neuronal Injury: Loading Rate-Dependent Changes in Acute Cytosolic Calcium and Lactate Dehydrogenase Release. Journal of Neurotrauma 1997;14:355.

[155] Edwards M.E., Steven S.S.W., Good T.A. Role of Viscoelastic Properties of Differentiated Sh-Sy5y Human Neuroblastoma Cells in Cyclic Shear Stress Injury. Biotechnology progress 2001;17:760.

[156] Regan R.F., Choi D.W. The Effect of Nmda, Ampa/Kainate, and Calcium Channel Antagonists on Traumatic Cortical Neuronal Injury in Culture. Brain research 1994;633:236.

[157] Mukhin A., Ivanova S., Allen J., Faden A. Mechanical Injury to Neuronal/Glial Cultures in Microplates: Role of Nmda Receptors and Ph in Secondary Neuronal Cell Death. Journal of neuroscience research 1998;51:748.

[158] Faden A.I., Ivanova S.A., Yakovlev A.G., Mukhin A.G. Neuroprotective Effects of Group Iii Mglur in Traumatic Neuronal Injury. Journal of Neurotrauma 1997;14:885.

[159] Tecoma E.S., Monyer H., Goldberg M.P., Choi D.W. Traumatic Neuronal Injury in Vitro Is Attenuated by Nmda Antagonists. Neuron 1989;2:1541.

[160] Gross G., Lucas J., Higgins M. Laser Microbeam Surgery: Ultrastructural Changes Associated with Neurite Transection in Culture. Journal of Neuroscience 1983;3:1979.

[161] Laplaca M.C., Cullen D.K., Mcloughlin J.J., Cargill R.S. High Rate Shear Strain of Three-Dimensional Neural Cell Cultures: A New in Vitro Traumatic Brain Injury Model. Journal of Biomechanics 2005;38:1093.

[162] Laplaca M.C., Prado G.R., Cullen D.K., Irons H.R. High Rate Shear Insult Delivered to Cortical Neurons Produces Heterogeneous Membrane Permeability Alterations. IEEE, 2008. p.2384.

[163] Cullen D.K., Laplaca M.C. Neuronal Response to High Rate Shear Deformation Depends on Heterogeneity of the Local Strain Field. Journal of Neurotrauma 2006;23:1304.

[164] Cukierman E., Pankov R., Stevens D.R., Yamada K.M. Taking Cell-Matrix Adhesions to the Third Dimension. Science's STKE 2001;294:1708.

[165] Vandevord P.J., Leung L.Y., Hardy W., Mason M., Yang K.H., King A.I. Up-Regulation of Reactivity and Survival Genes in Astrocytes after Exposure to Short Duration Overpressure. Neuroscience letters 2008;434:247.

[166] Cullen D.K., Simon C.M., Laplaca M.C. Strain Rate-Dependent Induction of Reactive Astrogliosis and Cell Death in Three-Dimensional Neuronal-Astrocytic Co-Cultures. Brain research 2007;1158:103.

[167] Brewer G., Torricelli J. Isolation and Culture of Adult Neurons and Neurospheres. Nat Protoc 2007;2:1490.

[168] Matei G.A., Thoreson E.J., Pratt J.R., Newell D.B., Burnham N.A. Precision and Accuracy of Thermal Calibration of Atomic Force Microscopy Cantilevers. Review of Scientific Instruments 2006;77.

[169] Rudoy D., Yuen S., Howe R., Wolfe P.J. Bayesian Changepoint Analysis with Application to Atomic Force Microscopy and Soft Material Indentation. Journal of the Royal Statistical Society Series C 2010;to appear.

[170] Radmacher M. Measuring the Elastic Properties of Biological Samples with the Afm. Engineering in Medicine and Biology Magazine, IEEE 1997;16:47.

[171] Faria E.C., Ma N., Gazi E., Gardner P., Brown M., Clarke N.W., Snook R.D. Measurement of Elastic Properties of Prostate Cancer Cells Using Afm. Analyst 2008;133:1498.

[172] Cross S.E., Jin Y.S., Rao J., Gimzewski J.K. Nanomechanical Analysis of Cells from Cancer Patients. nature nanotechnology 2007;2:780.

[173] Hertz H. Uber Den Kontakt Elastischer Korper. J. Reine Angew Mathematik 1881;92.

[174] Boudou T., Ohayon J., Picart C., Tracqui P. An Extended Relationship for the Characterization of Young's Modulus and Poisson's Ratio of Tunable Polyacrylamide Gels. Biorheology 2006;43:721.

[175] Prevost T.P., Balakrishnan A., Suresh S., Socrate S. Biomechanics of Brain Tissue. Acta Biomaterialia 2011;7:83.

[176] Gurtin M.E. An Introduction to Continuum Mechanics. New York: Academic Press, 1981.

[177] Holzapfel G.A. Nonlinear Solid Mechanics : A Continuum Approach for Engineering. Chichester ; New York: Wiley, 2000.

[178] Lee E. Elastic-Plastic Deformation at Finite Strains. Journal of Applied Mechanics 1969;36:1.

[179] Arruda E., Boyce M. A Three-Dimensional Constitutive Model for the Large Stretch Behavior of Rubber Elastic Materials. Journal of the Mechanics and Physics of Solids 1993;41:389.

[180] Bergstr^m J., Boyce M. Constitutive Modeling of the Time-Dependent and Cyclic Loading of Elastomers and Application to Soft Biological Tissues. Mechanics of Materials 2001;33:523.

[181] Storm C., Pastore J.J., Mackintosh F.C., Lubensky T.C., Janmey P.A. Nonlinear Elasticity in Biological Gels. Nature 2005;435:191.

[182] Xu J.Y., Tseng Y., Wirtz D. Strain Hardening of Actin Filament Networks - Regulation by the Dynamic Cross-Linking Protein Alpha-Actinin. Journal of Biological Chemistry 2000;275:35886.

[183] Miller K., Chinzei K. Constitutive Modelling of Brain Tissue: Experiment and Theory. Journal of biomechanics 1997;30:1115.

[184] Franceschini G., Bigoni D., Regitnig P., Holzapfel G. Brain Tissue Deforms Similarly to Filled Elastomers and Follows Consolidation Theory. Journal of the Mechanics and Physics of Solids 2006;54:2592.

[185] Guilak F., Tedrow J.R., Burgkart R. Viscoelastic Properties of the Cell Nucleus. Biochemical and Biophysical Research Communications 2000;269:781.

[186] Maniotis A., Chen C., Ingber D. Demonstration of Mechanical Connections between Integrins, Cytoskeletal Filaments, and Nucleoplasm That Stabilize Nuclear Structure. Proceedings of the National academy of Sciences of the United States of America 1997;94:849.

[187] Elkin B., Azeloglu E., Costa K., Morrison Iii B. Mechanical Heterogeneity of the Rat Hippocampus Measured by Atomic Force Microscope Indentation. Journal of Neurotrauma 2007;24:812.

[188] Solon J., Levental I., Sengupta K., Georges P.C., Janmey P.A. Fibroblast Adaptation and Stiffness Matching to Soft Elastic Substrates. Biophysical Journal 2007;93:4453.

[189] Krewson C.E., Chung S.W., Dai W., Mark Saltzman W. Cell Aggregation and Neurite Growth in Gels of Extracellular Matrix Molecules. Biotechnology and Bioengineering 1994;43:555.

[190] O'connor S.M., Stenger D.A., Shaffer K.M., Ma W. Survival and Neurite Outgrowth of Rat Cortical Neurons in Three-Dimensional Agarose and Collagen Gel Matrices. Neuroscience letters 2001;304:189.

[191] Chitnis P.V., Cleveland R.O. Acoustic and Cavitation Fields of Shock Wave Therapy Devices. vol. 829, 2006. p.440.

[192] Cleveland R.O., Chitnis P.V., Mcclure S.R. Acoustic Field of a Ballistic Shock Wave Therapy Device. Ultrasound in medicine & biology 2007;33:1327.